Climatological study of wakes from offshore wind farm clusters

Department of Wind Energy Master Report

Michael Alexander William Catton

DTU Wind Energy-M-0361

June 2020

DTU Wind Energy
Department of Wind Energy

Author: Michael Alexander William Catton

Title: Climatological study of wakes from offshore wind farm clusters

DTU Wind Energy-M-0361
June 2020

Project period:
January 2020 – June 2020

ECTS: 30

Education: Master of Science

Supervisor:
Xiaoli Guo Larsén
Jana Fischereit
Andrea N. Hahmann
DTU Wind Energy

Remarks:
This report is submitted as partial fulfillment of the requirements for graduation in the above education at the Technical University of Denmark.

DTU Wind Energy is a department of the Technical University of Denmark with a unique integration of research, education, innovation and public/private sector consulting in the field of wind energy. Our activities develop new opportunities and technology for the global and Danish exploitation of wind energy. Research focuses on key technical-scientific fields, which are central

for the development, innovation and use of wind energy and provides the basis for advanced education at the education.

We have more than 240 staff members of which approximately 60 are PhD students. Research is conducted within nine research programmes organized into three main topics: Wind energy systems, Wind turbine technology and Basics for wind energy.

Technical University of Denmark
Department of Wind Energy
Frederiksborgvej 399
4000 Roskilde
Denmark

www.vindenergi.dtu.dk

Technical University of Denmark
Department of Wind Energy
Frederiksborgvej 399
2800 Kgs. Lyngby
Denmark
Telephone 46 77 50 85

info@vindenergi.dtu.dk
www.vindenergi.dtu.dk

Acknowledgements

This thesis was conducted during the final semester of my master's degree at DTU and was completed with the help of a number of people whom I would like to thank.

Firstly, I must express my deepest gratitude to my supervisors Xiaoli Guo Larsén and Jana Fischereit for their constant guidance and support throughout the project. Their expertise has been invaluable, and their willingness to donate their time so generously is greatly appreciated. I would also like to thank my supervisor Andrea Hahmann for her additional insight and support during the project, and Martin Haubjerg Rosgaard and Marc Imberger for their technical assistance. I extend my thanks to the ForskEL/EUDP OffshoreWake project (PSO-12521), the researchers at DTU Wind Energy for their insight and knowledge, and Samuel Hawkins for the opportunity to communicate my findings to him and his colleagues at Vattenfall. Thanks to Vattenfall for providing SCADA data for the Sandbank and DanTysk wind farms, and BMWi (Bundesministerium für Wirtschaft und Energie) and PtJ (Projectträger Juleich) for providing data from the FINO3 research platform. Finally, I must thank Erin Langor for her simulations on which this thesis is based.

Abstract

As investment in offshore wind energy continues to increase in order to meet decarbonization goals, the density of wind farms in offshore areas is increasing, leading to clusters of closely packed wind farms. The negative effect this can have on the local wind resource leads to reductions in annual energy production, and the current project is dedicated to achieving a better understanding of wakes from offshore wind farm clusters.

This thesis investigates the behaviour of these wakes using mesoscale modelling, and includes analysis of the first long-term simulation for large offshore wind farm clusters using the two wind farm parameterizations Fitch and the Explicit Wake Parameterization (EWP) in the Weather Research and Forecasting (WRF) model.

Simulations in WRF are validated using measurements from the offshore research platform FINO3, and velocity deficits are examined as functions of wind speed, wind direction, and atmospheric stability. The wake effect is quantified by characteristics such as wake length, wake-affected area, and recovery profile, and the effect on power production of neighbouring wind farms is assessed. The behaviour of turbulence kinetic energy (TKE) in the wake of wind farms is also examined.

Results show that wakes simulated using the Fitch scheme are on average 50% longer than when simulated using the EWP scheme. There are significant differences in the recovery profile when using the two schemes. The Fitch scheme displays a more intense velocity reduction over the wind farm and the recovery follows an exponential curve, while the EWP scheme has a lower wind reduction and the recovery follows a linear curve.

The influence of climatological parameters shows that wakes are longest for winds between 5-10 ms^{-1} and under stable conditions. By analyzing SCADA data, the reduction in power production is found to be greatest under these conditions. The wind direction can also have a significant impact on power production depending on the location of the surrounding wind farms, and winds from directions that are densely populated by wind farms will have a further reduced velocity.

Contents

List of Figures

List of Tables

Abbreviations

ABL	Atmospheric boundary layer
ARW	Advanced research WRF
CF	Capacity factor
CFD	Computational fluid dynamics
CFSR	Climate Forecast System Reanalysis
DNS	Direct numerical simulation
DTU	Technical University of Denmark
EWP	Explicit Wake Parameterization
GRiB	General Regularly-distributed Information in Binary form
KE	Kinetic energy
LES	Large eddy simulation
MYNN	Mellor-Yamada-Nakanishi-Niino
NWF	No Wind Farm
OISST	Optimum Interpolation Sea Surface Temperature
PBL	Planetary boundary layer
RAMS	Regional Atmospheric Modeling System
RRTMG	Rapid Radiative Transfer Model for Global
SAR	Synthetic-aperture radar
SCADA	Supervisory control and data acquisition
TKE	Turbulence kinetic energy
WAsP	Wind Atlas Analysis and Application Program
WFP	Wind farm parameterization
WPS	WRF Preprocessing System
WRF	Weather Reasearch and Forecasting

CHAPTER 1

Introduction

This master's thesis is conducted as part of the OffshoreWake project, a collaboration between DTU Wind Energy and Vattenfall investigating the wind shadow effect behind large offshore wind farms and the effects of ocean surface parameters. This thesis focuses on examining the behaviour of wakes in large offshore wind farm clusters using the wind farm parameterizations Fitch and EWP in the mesoscale model WRF, and quantifying the wake effect and the differences between the two parameterizations. A number of parameters that are relevant for offshore wind energy applications, including wind velocity deficits and turbulence kinetic energy, are examined as a function of climatological parameters such as atmospheric stability, wind speed and wind direction.

The study is based on data from WRF simulations run by previous master's student Erin Langor, where the 2018 climate in a region of the North Sea was simulated, and the focus is on Vattenfall wind farms Sandbank and DanTysk which are situated in a large cluster of offshore wind farms in the German Bight. The simulations by Langor are the first long-term simulations for large offshore wind farm clusters using the Fitch and EWP schemes. Langor's thesis highlighted monthly trends in the behaviour of wind farm wakes in the North Sea and illustrated the effect of wakes on power production through analysis of annual mean capacity factors and their dependency on wind direction. She also found that the Fitch scheme consistently showed greater velocity deficits than the EWP scheme.

In this thesis, a systematic approach to quantifying wake characteristics is taken, expanding on the results found by Langor by applying data binning and statistical analysis to quantify the influence of climatological parameters on wakes and the differences when using the two parameterization schemes. A validation of the simulations is conducted using met mast measurements from the FINO3 research platform, and SCADA data from the DanTysk wind farm is used to determine the influence of wakes on turbine capacity factors under certain conditions. The theoretical concepts necessary to conduct and understand this study are explained in the report, including meteorological concepts and the theory behind the wind farm parameterization schemes.

This chapter includes the motivation for studying wind farm wakes in offshore wind farm clusters and a review of some of the discoveries and advancements already made in the field of study.

1.1 Motivation

In 2019, 15.4 GW of wind power was installed in Europe, of which 24% was offshore, adding a record 3.6 GW to the European offshore wind energy capacity (WindEurope Business Intelligence 2020). In 2017, 71% of all offshore wind capacity in Europe came from installations in the North Sea (Sawyer and Liming 2017). The offshore wind sector is growing, but there is a limit to the space available for offshore wind farms in shallow waters. Due to the decreasing area available for new installations, wind farms are being erected in closer proximity to each other, creating clusters of wind farms, and the effect of neighbouring farms on power production could be considerable (Agora 2020).

A wind turbine extracts kinetic energy from the atmosphere, turning it into electrical energy via a generator which is sent to the electricity grid. The decrease in kinetic energy in the atmosphere results in a reduced wind speed in the wake of the turbine. The wake effects become more complex when a group of turbines are placed in close vicinity of one-another, as is the case with a wind farm.

The OffshoreWake project, a collaboration between DTU Wind Energy and Swedish energy company Vattenfall, aims to improve the efficiency of the Danish power system by studying the large-scale wake effects from neighbouring wind farms (OffshoreWake 2017). As part of the OffshoreWake project, the purpose of this thesis is to create a better understanding of the modelling of wind farm wakes and their climatological effects.

Using the mesoscale model Regional Atmospheric Modeling System (RAMS), Baidya Roy et al. (2004) found that the presence of a wind farm significantly slowed down the wind at turbine hub-height level. Depending on climatological factors, wakes behind Horns Rev and Nysted extended over a distance of 5-20 km in a study by Christiansen and Hasager (2005), where wakes were observed using satellite synthetic-aperture radar (SAR). These findings indicated that there may be a negative impact on the efficiency and power production of wind farms when located in these clusters.

1.2 Literature review

The study of inter-turbine wakes, or wakes within a wind farm, is well-documented. Jensen (1983) devised a simple wake model for calculating the wake behind a wind turbine. Barthelmie et al. (2009) demonstrated that power losses due to wakes can be modelled using computational fluid dynamics (CFD), and Barthelmie and Jensen (2010) quantified relationships between wind farm efficiency and climatological parameters such as wind speed, wind direction, turbulence and atmospheric stability using the wind farm software Wind Atlas Analysis and Application Program (WAsP).

Baidya Roy et al. (2004) and Christiansen and Hasager (2005) found that not only were velocity deficits caused by the presence of wind farms, but that the wake recovery behind a wind farm was dependent on the wind speed, atmospheric stability and the number of turbines in operation. Using SAR, Djath et al. (2018) observed that stable atmospheric conditions favoured longer wakes, and that the overlapping and interaction of wakes could vastly extend their length. Platis et al. (2018)

found the first in situ evidence of wakes in the far field behind offshore wind farms, using research aircraft to confirm wake lengths of tens of kilometers under stable atmospheric conditions and wind speed deficits of up to 40%.

In studies by Ivanova and Nadyozhina (2000) and Malyshev et al. (2003), wind farms were approximated by increasing the surface roughness length of the wind farm area, implicitly representing the general large-scale impacts of wind farms. Using this method, it is difficult to choose an appropriate roughness length without field measurements; however, due to its computational effectiveness, it has been widely used in a number of studies (Keith et al. 2004), (Kirk-Davidoff and Keith 2008), (Wang and Prinn 2010), and (Wang and Prinn 2011). Baidya Roy et al. (2004) modelled a wind farm as an elevated momentum sink and a source of turbulence, a method used in a number of subsequent papers, and improved upon in (Blahak et al. 2010) by adding a loss factor to include mechanical and electrical losses in the model. Other parameterizations of wind farm effects include explicit parameterization of each individual turbine drag using computationally heavy numerical simulations such as large eddy simulation (LES) in Lu and Porté-Agel (2010) or other CFD modelling.

In 2012, a new wind farm parameterization (WFP) was developed by Fitch et al. (2012) for the Weather Research and Forecasting (WRF) Model. While some previous studies neglected any representation of turbulence or wind shear, the Fitch scheme (also known as the WRF-WF scheme) based the turbine-induced drag on the thrust coefficient of a modern turbine. Additionally, the source of the turbulence kinetic energy (TKE) varied with wind speed. Using the Fitch scheme, wakes extended up to 60 km behind an idealized wind farm.

In a study by Volker et al. (2015), a new approach called the Explicit Wake Parametrisation (EWP) was developed and implemented in WRF, using a different definition of TKE than in the Fitch scheme. Although results showed similar wake lengths upon comparison, the recovery profiles of the two schemes differed. The EWP scheme exhibited a linear recovery of velocity behind the wind farm, while the Fitch scheme showed a rapid recovery in the near-wake followed by a slower recovery further downstream. Additionally, differences in the TKE field as well as the velocity profiles were observed when using the two schemes.

There is debate as to which parameterization scheme is more accurate, and few studies have utilized and compared the two wind farm parameterization schemes. Shepherd et al. (2020) compared EWP and Fitch using a single year-long simulation over onshore wind farms in the U.S., finding that using EWP resulted in faster wake recovery and capacity factors of 2-3% higher than for the more commonly applied Fitch scheme. However, due to the absence of measured wake data, 'it would be premature to make recommendations with regard to which wind farm parameterization exhibits superior fidelity' (Shepherd et al. 2020, p. 358). Running a 9-month WRF simulation for an onshore wind farm cluster, Pryor et al. (2020) evaluated the sensitivity of wake effects and power production to model resolution using the Fitch and EWP schemes, finding that EWP resulted in a higher gross capacity factor (CF) than Fitch, equating to a $\sim 5\%$ higher power output. Differences in capacity factor were also shown to be greater under stable conditions. Pryor found that the spatial extent of wind farm wakes was greater when using Fitch, while noting that Lee and Lundquist (2017) reported that the Fitch scheme showed positive bias in wake intensity and therefore negative bias downwind in power production, meaning Fitch underestimated power production compared to observations. Despite Pryor's results, the lack of long-term data meant it was not possible to determine which of the wind farm parameterizations exhibited greater fidelity, and Pryor stated:

> Pending availability of suitable computing resources and release of long-term power production data from individual wind farms, future work should include multiyear simulations and detailed validation against those observations (Pryor et al. 2020, p. 172).

There are currently no publications comparing the EWP and Fitch schemes in long-term simulations for offshore wind farms, making this thesis one of the very first studies to deal with the subject.

CHAPTER 2

Wakes and wake modelling

This chapter introduces the concept of wakes and wake models, and presents some theoretical background for the concepts used throughout this study. The details of mesoscale modelling and the theories behind the two wind farm parameterization schemes Fitch and EWP will be explained, and a summary of findings in current literature that compare the two schemes is presented.

2.1 Wakes

In order to generate electricity, wind turbines extract kinetic energy from the wind. The kinetic energy in the air behind the rotor is thereby reduced, leading to a reduced wind speed downstream of the turbine, as shown in Figure 2.1, and increased turbulence. The reduction in wind speed can cause significant power production losses in wind farms. This reduction in flow velocity and increase in turbulence intensity in the downstream region is referred to as the wake. The wake is divided into the near and the far wake. In the near wake there is a sudden pressure drop, which quickly recovers due to turbulent mixing. The drop in pressure induces a thrust force in the stream-wise direction against the incoming flow, and the magnitude of this thrust force dictates the magnitude of the velocity deficit. Not only does the flow velocity decrease due to the flow momentum extracted by the rotor, but it continues to decrease throughout the near wake as this region expands due to the conservation of mass principle (Zhang 2015). The near wake is a complex region, where mechanical turbulence is induced by tip vortices caused by the blade aerodynamics, and shear-induced turbulence occurs as the high-velocity ambient flow mixes with the low-velocity flow within the wake. The near wake extends roughly 5 rotor diameters downstream (Okulov et al. 2014), where the far wake begins. Here the mixing layer, which causes the mechanical turbulence, has reached the axial line, changing the centre-line velocity, and the far wake is now governed entirely by the turbulence shear mixing. This mixing continues until the flow velocity has fully recovered and reached that of the ambient flow. The velocity deficit in the far wake can be approximated by a Gaussian distribution (Vermeer et al. 2003).

The far wake region can be analyzed using various wake models. This can be simple for a two-turbine case, but it gets more complicated for multiple wind turbines where wakes start overlapping.

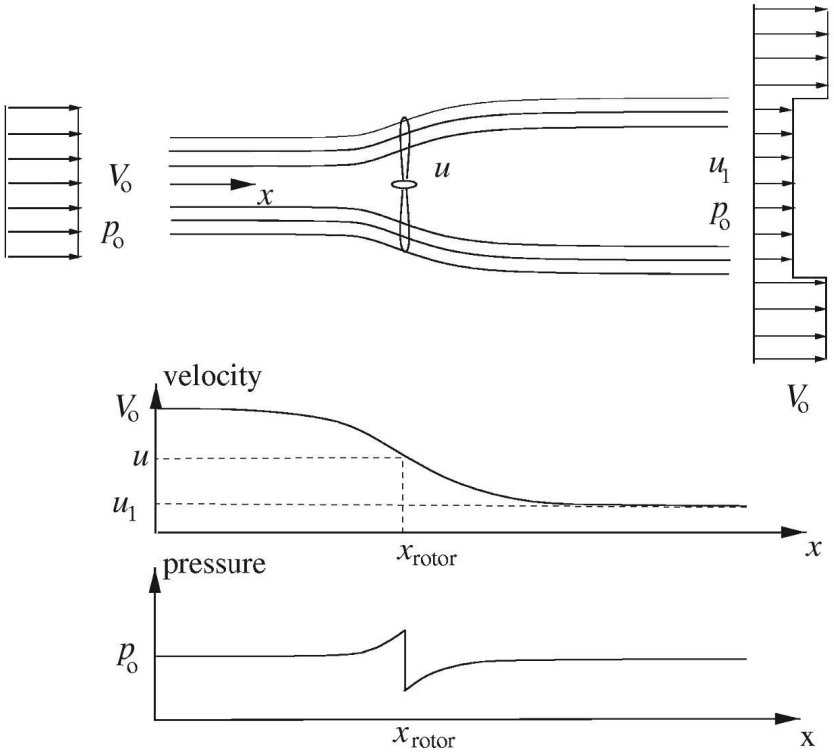

Figure 2.1: Streamlines past the rotor and the axial velocity and pressure up- and downstream of the rotor. Figure from Hansen (2015, p. 24). Copyright by Taylor & Francis Informa UK Ltd. Reprinted with permission.

2.2 Wake models

Many models have been developed to describe wakes, and they can generally be divided into three categories:

- Engineering models
- CFD models
- Mesoscale models

Engineering models are analytical models and often greatly simplified, and therefore requiring only few computational resources. One of the first engineering wake models is the Jensen/PARK model, first developed by Jensen (1983). Instead of a Gaussian profile, the far wake is approximated to a top-hat profile, such that the wake is uniformly distributed at a given distance. The wake expansion is assumed to be linear and is defined by a wake decay coefficient. The Jensen/PARK model is applied in several commercial wind resource assessment tools such as WAsP and WindPRO.

For increased precision, CFD models such as the linearized Navier-Stokes equations, Reynolds-averaged Navier-Stokes (RANS) equations, direct numerical simulation (DNS), and LES can be used. The various models are used depending on the scales to be investigated; for example, LES and DNS are often used for resolving turbulence on the smallest scales, requiring fine grids and high computational costs.

Mesoscale models, often complex and costly, are widely used in atmospheric research and atmospheric forecasting and can be used for wake simulation and analysis with a high precision. In this study, results from simulations using the mesoscale model WRF have been used.

2.3 Atmospheric stability

As discussed previously, the flow velocity inside a wake is largely governed by turbulence shear mixing. An increased level of mixing means a faster velocity recovery and shorter wake. The level of turbulent mixing is heavily influenced by atmospheric conditions in the atmospheric boundary layer (ABL), and these conditions are broadly divided into the three categories unstable, stable, and neutral stability. Barthelmie and Jensen (2010) found that the efficiency of the Nysted wind farm decreased by up to 8.1% under stable conditions when compared to neutral conditions, while unstable conditions lead to an increase of up to 3.0%. This section will introduce some of the key parameters for determining atmospheric stability (or stratification), as well as several methods that can be used to define the stability.

The stability of the atmosphere is closely related to temperature gradients, or the variation of temperature with height. This temperature variation is called the lapse rate Γ, and the adiabatic lapse rate of dry air is given by:

$$-dT/dz = \Gamma_d = c_p/g \ , \tag{2.1}$$

where T is the temperature at height z, c_p is the specific heat capacity, and g is the gravitational acceleration. The dry adiabatic lapse rate is roughly $-10\,\mathrm{K/km}$, meaning the temperature of a dry air parcel decreases approximately 10 K per kilometre that it moves upwards (Zhang 2015). The assumption of a dry atmosphere when calculating stability is due to added complexity when including water vapour, and neglecting the influence of humidity, especially in offshore conditions, may lead to errors in the vertical extrapolation of the mean wind speed.

Another important term in the field of stability is the potential temperature θ, which is the temperature that a parcel of air would have if it were expanded or compressed adiabatically to the surface pressure, and it can be calculated using Poisson's equation (Wallace and Hobbs 2006).

$$\theta = T\left(\frac{p_0}{p}\right)^{R/c_p} \tag{2.2}$$

Here, T is the absolute temperature [K] at a given height, p the pressure at the same height, p_0 the pressure at the surface, and R the gas constant.

The effect of the adiabatic lapse rate can be seen in Figure 2.2, where the temperature of an air parcel in neutral conditions will decrease by the same amount as the surrounding temperature, and no buoyancy forces appear to accelerate the parcel. As the environmental lapse rate is greater than the adiabatic in unstable conditions, the lifted parcel will be warmer and therefore lighter than the surrounding air, causing positive buoyancy forces and vertical acceleration. Unstable conditions occur when the surface temperature is warmer than the air above it. Stable conditions occur when

the surface is cooler than the air above it, and an air parcel displaced upwards will return to its original height, resisting vertical motion.

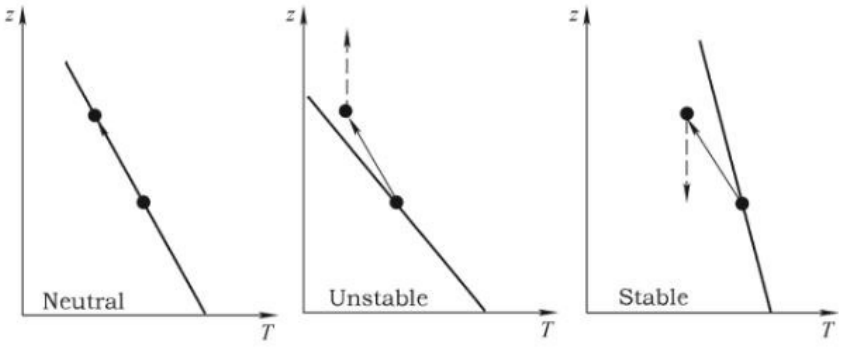

Figure 2.2: Three cases of vertical parcel displacement. Figure from Zhang (2015, p. 230). Copyright by John Wiley and Sons. Reprinted with permission.

Atmospheric stability can therefore be defined by the heat flux H, which is the amount of heat that goes into or out of the surface per unit area caused by a difference in temperature between the atmosphere and surface. Heat flux from the surface to the atmosphere is positive leading to unstable conditions (greater turbulent mixing), and from the atmosphere to the surface is negative leading to stable conditions (lower turbulent mixing).

- $H > 0$ unstable atmosphere
- $H = 0$ neutral atmosphere
- $H < 0$ stable atmosphere

Another definition of stability comes from Monin-Obukhov similarity theory, where buoyancy and turbulent flows can be expressed through the Monin-Obukhov length L.

$$L = -\frac{u_*^3 \overline{\theta_v}}{\kappa g \left(\overline{w'\theta_v'}\right)_s} \tag{2.3}$$

Here, u_* is the frictional velocity, $\overline{\theta_v}$ is the mean virtual potential temperature, κ the von Kármán constant, and $\left(\overline{w'\theta_v'}\right)_s$ the surface virtual potential temperature flux. L represents the height where turbulence is generated more by buoyancy than by wind shear (Landberg 2016). Atmospheric stability can be classified according to intervals of the Monin-Obukhov length, and several sub-classes are defined in various literature, such as very unstable, near-stable, near-neutral stable etc. For this study, just three classes have been defined for simplicity. These are based on stability class definitions in Peña et al. (2008).

Table 2.1: Atmospheric stability classes according to intervals of the Monin-Obukhov length L.

L [m]	**Stability class**
$-500 \leq L \leq 0$	Unstable
$500 < \|L\|$	Neutral
$0 < L \leq 500$	Stable

However, both these measures of stability (heat flux H and Monin-Obukhov length L) have a high uncertainty in WRF due to the model's difficulty in estimating momentum and heat fluxes.

Instead, the Bulk Richardson Number Ri_B, which uses commonly available observations of temperatures and wind speeds, is used to classify stability conditions in this study. Using the WRF outputs for potential temperature θ and wind speed U at the sea surface and at height z, Ri_B can be calculated as follows (Larsén et al. 2011):

$$Ri_B = \frac{g}{\overline{\theta}} \frac{\Delta\theta}{\Delta z} \Big/ \left(\frac{\Delta U}{\Delta z} \right)^2 \tag{2.4}$$

Generally, positive Ri_B values point to stable conditions, negative values to unstable conditions, and values close to 0 indicate neutral conditions. The differentiation between stability classes is often based on the critical Bulk Richardson Number Ri_{Bc}, but there is a considerable uncertainty when choosing an appropriate value. Therefore, stability conditions are estimated using the relation between the Monin-Obukhov length and the Bulk Richardson Number. Using the calculated value for Ri_B, L can be estimated using the following equations (Hansen et al. 2012), and the stability is determined from Table 2.1.

$$\frac{z}{L} = 10 Ri_B \qquad \text{when} \qquad Ri_B \leq 0 \tag{2.5}$$

$$\frac{z}{L} = \frac{10 Ri_B}{1 - 5 Ri_B} \qquad \text{when} \qquad Ri_B > 0 \tag{2.6}$$

When determining stability conditions, the thermal properties of the surface are significant, as expressed by $\overline{\theta}$ and $\Delta\theta$ in Equation 2.4. Zhang (2015) explains that while conditions on land experience diurnal variations, an annual variation is seen offshore due to the high heat capacity of the ocean. This is because the surface temperature of the sea is at its highest in the summer and lowest during the winter, which leads to predominantly unstable conditions in autumn and early winter, and stable conditions in spring and early summer. Near the coast, the situation is complicated by land and sea breezes where low-level jets can occur, strongly affecting the wind speed near hub height (Zhang 2015).

The stability also influences the surface layer wind profile, as seen in Figure 2.3. The surface layer is the lowest part of the atmospheric boundary layer and can vary from tens of metres to hundreds of metres, depending on the stability. The surface layer is low under stable conditions and high under

unstable conditions. Using a stability function Ψ_m, the logarithmic wind profile in the surface layer can be calculated as:

$$u(z) = \frac{u_*}{\kappa} \ln\left(\frac{z}{z_0} + \Psi_m\left(\frac{z}{L}\right)\right) , \tag{2.7}$$

where z_0 is the surface roughness length.

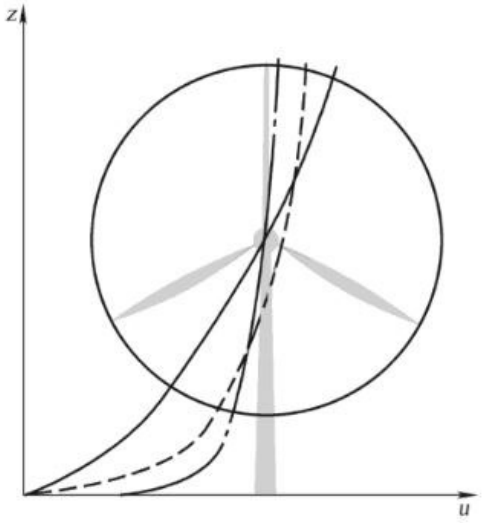

Figure 2.3: The influence of atmospheric stability on a wind velocity profile in the surface layer: Neutral (dashed line), unstable (dot-dashed line), stable (solid line). Figure from Zhang (2015, p. 233). Copyright by John Wiley and Sons. Reprinted with permission.

Zhang (2015) states that the increase in turbulent mixing under unstable conditions accelerates wake recovery, leading to shorter wakes. This is favourable with regard to power production for any downstream turbines or wind farms.

2.4 Mesoscale modelling and wind farm parameterization schemes

Mesoscale meteorology is the study of weather systems in the range of 10^3-10^6 metres, between the microscale and the synoptic scale, simulating the atmospheric flow using the RANS equations. The 3D domain is divided into cells with a horizontal resolution usually between a few hundred metres up to 10-20 km, and a vertical resolution in the order of tens of metres. Due to the relatively low horizontal resolution, sub-grid processes such as turbulence are unresolved in mesoscale models, introducing the need for parameterizations. WRF includes parameterizations for processes such as turbulence and diffusion, cumulus convection, and planetary boundary layer and surface layer physics. As wind turbines affect the flow on these small scales, advanced parameterizations have recently been developed in order to resolve the effect of wind turbines inside grid cells. Early parameterizations treated wind turbines as an increase in roughness length (a measure for the friction imposed on the wind by the surface of the Earth), while modern wind farm parameterizations model turbines as an elevated momentum sink and a function of wind speed and thrust coefficient.

The first of these was developed by Fitch et al. (2012) and is commonly referred to as the Fitch scheme, and the second was developed by Volker et al. (2015) and dubbed the Explicit Wake Parameterization (EWP). Both schemes model turbines as drag devices that extract kinetic energy from the atmosphere, causing the wind speed to decrease in the wake, but their differing treatment of TKE is the main distinguishing factor. Both schemes will be discussed in further detail later in this chapter.

2.4.1 Weather Research and Forecasting Model framework

When simulating the meteorology of a domain, WRF has the option to run an ideal simulation or a real simulation. An ideal simulation takes a constant wind speed and direction as initial conditions, whereas a real simulation uses observed data passed through the WRF Preprocessing System (WPS), interpolating the meteorological and terrestrial data onto the projected domain grid, supplying WRF with a 3D snapshot of the atmosphere as boundary conditions. A flowchart of the processes for a real simulation in WRF can be seen in Figure 2.4. The process starts with a number of subroutines in the pre-processing system WPS: GEOGRID defines the model domains and resolutions and creates static files of geographical data; UNGRIB extracts reanalysis data from GRiB files containing gridded observational data; METGRID interpolates the meteorological and terrestrial data found in UNGRIB to the model domain defined in GEOGRID. The WPS output is passed to the real-data pre-processor in ARW (Advanced Research Weather Research and Forecasting model), which generates initial and lateral boundary conditions. With this information, the simulation can begin in WRF. This study uses the 2018 climate over a domain in the North Sea, obtained in real simulations run by Langor (2019) using Climate Forecast System Reanalysis (CFSR) data and Optimum Interpolation Sea Surface Temperature (OISST) data for the initialization of the meteorological fields. A summary of the settings for simulations used in this study can be seen in Chapter 3.2.

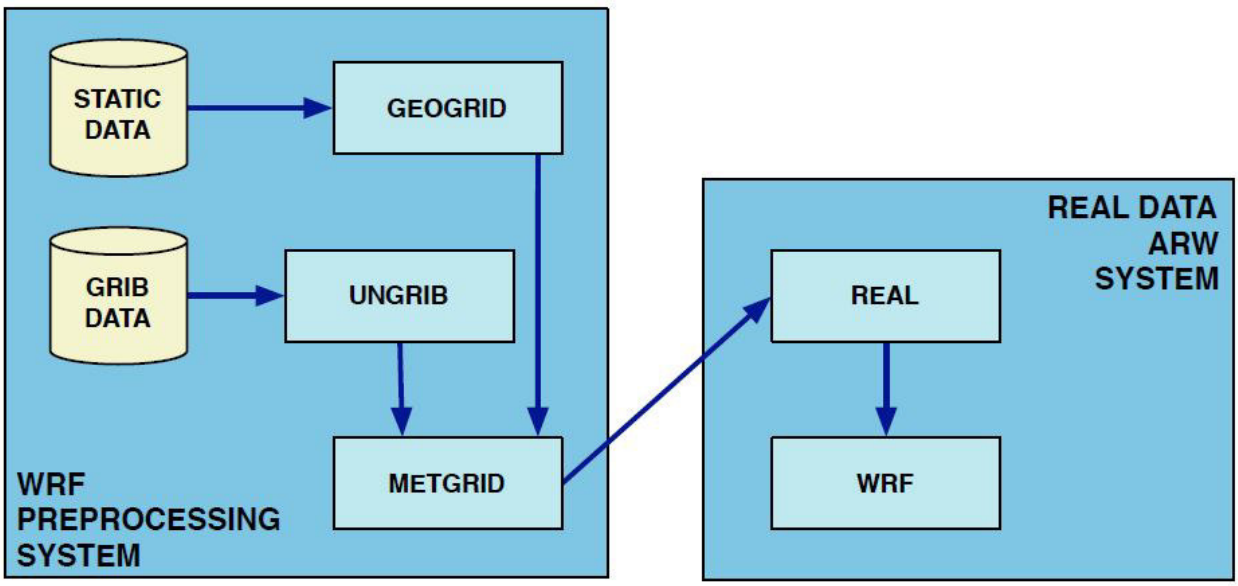

Figure 2.4: Schematic showing data flow and program components in WPS, and how the WPS feeds initial data to the ARW. Figure from Skamarock et al. (2008, p. 44) in accordance with the Creative Commons Attribution license.

2.4.2 Governing equations in WRF

A central technique when using RANS-based models is the use of Reynolds decomposition, where an instantaneous quantity is decomposed into its expectation value (the spatial or ensemble average) and its fluctuations. This can be applied to the Navier-Stokes equations, which describe the motion of a fluid. Due to the various mixing-length scales involved in turbulent flow, finding a solution to the Navier-Stokes equations is close to impossible due to computational time required. Applying Reynolds decomposition to the Navier-Stokes equations, which describe the motion of fluids, the Reynolds-averaged Navier-Stokes equations are obtained, and time-averaged solutions to the Navier-Stokes equations can be calculated. The RANS equations describing flow evolution are shown in Equation 2.8.

$$\frac{\partial \overline{u}_i}{\partial t} + \overline{u}_j \frac{\partial \overline{u}_i}{\partial x_j} + \frac{\partial \overline{u_i' u_j'}}{\partial x_j} = -\frac{1}{\rho}\frac{\partial \overline{p}}{\partial x_i} - 2\varepsilon_{ijk}\Omega_j \overline{u}_k - \delta_{i3} g + \overline{f}_{d_i} \tag{2.8}$$

The Navier-Stokes and RANS equations arise from applying Newton's second law to fluid motion, and the left-hand side (l.h.s.) of Equation 2.8 describes the momentum of the fluid, while the right-hand side (r.h.s.) describes the forces applied to the fluid. Reynolds-averaged quantities are denoted by an overline, and fluctuations around the mean quantities are denoted by a prime. The terms on the l.h.s. describe the storage of momentum, the advection of the mean momentum, and the influence of the Reynolds stress on the mean flow, respectively. The terms on the r.h.s. describe the mean pressure-gradient force, the Coriolis force, and the gravitational acceleration, and the final term $\overline{f}_{d_i}$ is the average horizontal forcing due to the wind turbines (Volker et al. 2015).

The prognostic equation governing the evolution of TKE can be stated in the compact form:

$$\frac{\partial \overline{e}}{t} + \overline{T} = \overline{p}_s + \overline{p}_b + \overline{p}_t - \epsilon \ , \tag{2.9}$$

where $\overline{e}$ denotes TKE and $\overline{T}$ represents the TKE transport, including advection and turbulent transport of TKE and divergence of pressure correlation. Shear production, turbulence production, turbine-induced turbulence, and dissipation are represented by $\overline{p}_s$, $\overline{p}_b$, $\overline{p}_t$, and ϵ, respectively. The turbine-induced turbulence $\overline{p}_t$ is calculated in the wind farm parameterization.

2.4.3 Fitch scheme

The Fitch scheme, introduced in Fitch et al. (2012), models the wind turbine drag as a function of extracted kinetic energy (KE) from the atmosphere by turbines, and is dependent on the thrust coefficient C_T. The thrust coefficient is obtained from the thrust curve, making it a function of wind speed, expanding on the method used by Blahak et al. (2010) where the fraction of energy converted to TKE was constant with wind speed. In the Fitch scheme, the velocity fluctuation u'' is defined as the difference between the grid-cell-averaged velocity $\langle u \rangle$ and the instantaneous velocity u (Figure 2.5). The Fitch scheme models the turbines' effect on the atmosphere by representing the turbines as a momentum sink, transferring a fraction of the extracted kinetic energy to electricity

and the remainder to TKE. The loss of KE from the atmosphere due to the action of N wind turbines in a single grid cell is described by Equation 2.10. Note that the Fitch scheme only takes into account wake effects between turbines in adjacent cells, and not for wake effects between turbines in the same grid cell. The rate of loss of kinetic energy from the atmosphere due to the drag from wind turbines is calculated by:

$$\frac{\partial E_D}{\partial t} = -\frac{C_T N \sum_k A(k)|U(k)|^3}{2(\Delta x)^2 \Delta z(k)} \ , \tag{2.10}$$

where $A(k)$ is the turbine rotor area intersecting with model level k, and Δx and Δz are the horizontal and vertical model grid spacings, respectively (Volker 2014). Of this extracted kinetic energy, the amount used for production of electrical energy is:

$$\frac{\partial E}{\partial t} = \frac{C_P N \sum_k A(k)|U(k)|^3}{2(\Delta x)^2 \Delta z(k)} \tag{2.11}$$

The difference between total power extracted by turbines (Equation 2.10) and power converted to electricity (Equation 2.11) is converted into turbulence kinetic energy:

$$\overline{p_t} = \frac{C_e N \sum_k A(k)|U(k)|^3}{2(\Delta x)^2 \Delta z(k)} \quad , \quad C_e = C_T - C_P \tag{2.12}$$

Because $\langle \overline{p_t} \rangle \propto \langle u \rangle^3$, this approach results in a large increase in TKE production in grid cells containing turbines, quickly decaying downstream. This TKE source represents the ambient flow being stirred by the turbines in the grid cell, while the mixing that results from vertical shear induced by the momentum sink is produced in the ABL scheme in WRF. TKE is thereby produced both by turbines and by shear when using the Fitch wind farm parameterization.

2.4.4 Explicit Wake Parameterization scheme

The Explicit Wake Parameterization was introduced in Volker et al. (2015), using classical wake theory to describe the unresolved wake expansion in turbine-containing grid cells, which is where the largest velocity gradients occur. Similar to the method used in the Fitch scheme, turbines are treated as drag devices and a grid-cell-averaged drag force $\langle \overline{p_t} \rangle$ represents the individual turbines in a cell. Unlike in the Fitch scheme however, the EWP scheme defines the TKE from the random fluctuations u' around the ensemble-averaged velocity $\overline{u}$ at hub height (Figure 2.5), and $\langle \overline{p}_t \rangle$ is expressed as:

$$\langle \overline{p}_t \rangle = \langle \overline{u'_{i,h} f'_{d_i}} \rangle \tag{2.13}$$

These fluctuations are much smaller than those in the Fitch scheme, and the resulting TKE is small enough to be neglected. This means that the additional TKE is solely generated by shear production in the ABL scheme, and the $\overline{p}_t$ term is disregarded.

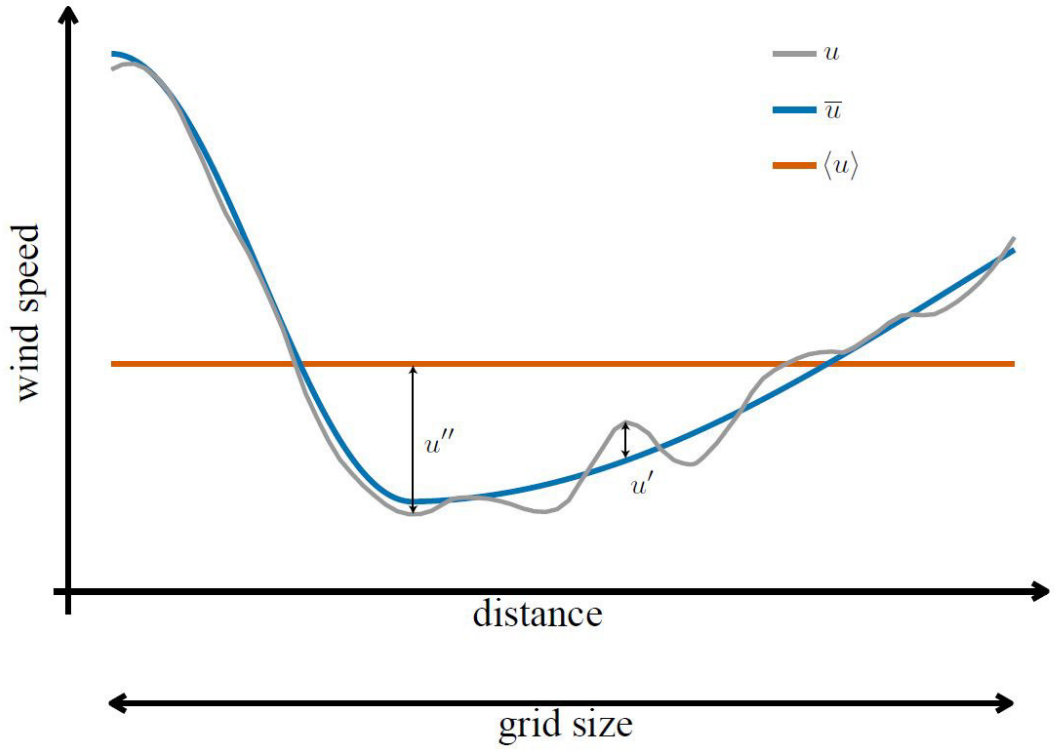

Figure 2.5: A sketch of the downstream development of a turbine-induced velocity reduction. The grey line represents the instantaneous velocity, the blue line shows the ensemble average, and the orange line the spatial average. The difference between the average and instantaneous velocity defines the turbulence fluctuation at each distance. Figure from Volker et al. (2015, p. 3716) in accordance with the Creative Commons Attribution (CC BY) license.

Based on the research by Tennekes and Lumley (1972), the velocity deficit profile $\overline{u}_d$ behind a turbine rotor is described in the EWP scheme by:

$$\overline{u}_d = \overline{u}_s \exp\left[-\frac{1}{2}\left(\frac{z-h}{\sigma}\right)^2 - \frac{1}{2}\left(\frac{y}{\sigma}\right)^2\right] , \tag{2.14}$$

where $\overline{u}_s$ is the maximum velocity deficit at the centre of the wake, h is hub height, and σ is a length scale that determines the wake expansion:

$$\sigma^2 = \frac{2K}{\overline{u}_o}x + \sigma_o^2 \tag{2.15}$$

The wake expansion is described by the turbulence diffusion coefficient K, which is determined from the ABL scheme, and the free stream velocity at hub height $\overline{u}_o$. The initial length scale σ_o, which describes the near wake, should chosen based on the turbine type and is set to 1.6 in this study. In Volker et al. (2015), the initial length scale was fitted based on measurements from Horns Rev I, which is made up of Vestas V80-2.0 MW turbines.

Alternatively, the velocity deficit profile can be expressed as a function of the thrust coefficient C_T:

$$\overline{u}_d = \frac{C_T r_o^2 \overline{u}_o}{4\sigma^2} \exp\left[-\frac{1}{2}\left(\frac{z-h}{\sigma}\right)^2 - \frac{1}{2}\left(\frac{y}{\sigma}\right)^2\right] , \tag{2.16}$$

For every vertical model layer k, the horizontal grid-cell-averaged drag force components are obtained:

$$\langle \overline{f}_{d_1}(k) \rangle = -\sqrt{\frac{\pi}{8}} \frac{C_T r_o^2 \overline{u}_o^2}{\Delta x \Delta y \sigma_e} \exp\left[-\frac{1}{2}\left(\frac{z-h}{\sigma_e}\right)^2\right] \cos\left[\varphi(k)\right] \tag{2.17}$$

$$\langle \overline{f}_{d_2}(k) \rangle = -\sqrt{\frac{\pi}{8}} \frac{C_T r_o^2 \overline{u}_o^2}{\Delta x \Delta y \sigma_e} \exp\left[-\frac{1}{2}\left(\frac{z-h}{\sigma_e}\right)^2\right] \sin\left[\varphi(k)\right] \tag{2.18}$$

φ is the wind direction, and the effective length scale σ_e is related to the model grid size and the downstream distance L that the wake has travelled within the grid cell.

$$\sigma_e = \frac{1}{L} = \int_0^L \sigma \mathrm{d}x = \frac{\overline{u}_o}{3KL}\left[\left(\frac{2K}{\overline{u}_o} L + \sigma_o^2\right)^{\frac{3}{2}} - \sigma_o^3\right] \tag{2.19}$$

From Equations 2.17 and 2.18, the grid-cell-averaged turbine-induced horizontal forcing $\overline{f}_{d_i}$ from the RANS equations is found.

2.4.5 Comparison of parameterizations in literature

After the introduction of the EWP scheme in Volker et al. (2015), several analyses were conducted using both the EWP and Fitch schemes, and results were compared. Using two met masts in the wake of Horns Rev I and an ideal simulation with hub height velocity $10\,\mathrm{ms}^{-1}$ and stability conditions assumed as neutral, measurements of the velocity in the wake of the wind farm agreed well with the EWP scheme, which reproduced the wind farm wake within the standard deviation of the measurements. While the velocity recovery in the EWP scheme was approximately linear, the Fitch scheme showed a faster initial velocity increase immediately behind the wind farm, displaying an exponential recovery. Both schemes estimated the wind speed at the end of the wind farm to within 0.1% of one another. As shown in Figure 2.6, the wake length using both schemes was very similar, both extending roughly 45 km downstream of the the wind farm (using a threshold of 3% velocity reduction as the wake edge).

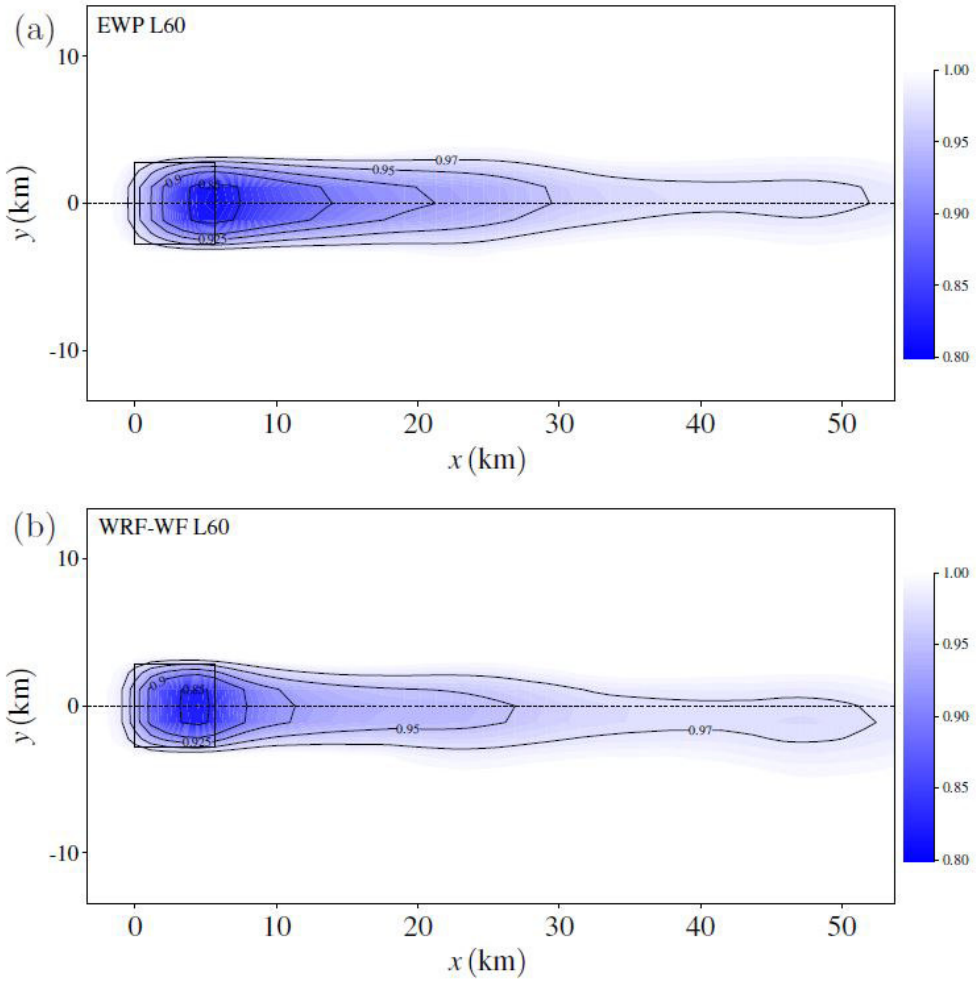

Figure 2.6: Horizontal view of the WRF-simulated velocity field at hub height using (a) EWP and (b) Fitch. The simulations are for $10\,\mathrm{ms}^{-1}$ in the 270° wind direction and 60 vertical layers. The dotted line indicates the latitudinal centre and the solid rectangle the outer boundary of the wind farm. Figure from Volker et al. (2015, p. 3724) in accordance with the Creative Commons Attribution (CC BY) license.

When comparing the TKE profile around the wind farm for both schemes, the TKE increase due to the wind farm is much larger for Fitch and is at its maximum within the wind farm. This is due to the additional turbulence generated by the source term $\langle \overline{p}_t \rangle$ in the Fitch scheme. In Figure 2.7, the EWP TKE field shows a maximum increase behind the wind farm, where the velocity gradients are largest. The vertical extension of the TKE field in Fitch is higher than in EWP, which slightly influences the velocity profile. The wind profile is symmetric around the hub height for EWP simulations, whereas the maximum velocity deficit in Fitch is displaced vertically above hub height (as shown in Figure 9 in Volker et al. (2015, p. 3726)). In the EWP TKE field, there is a decrease in TKE directly below the rotor area and an increase above hub height. This is not seen in the Fitch TKE field, where there is a small increase in TKE in front of the wind farm, and increase within and behind it. The results from the EWP simulations agree well with findings from Wu and Porté-Agel (2012), where the turbulence field was simulated using an actuator-disc approach in an LES model.

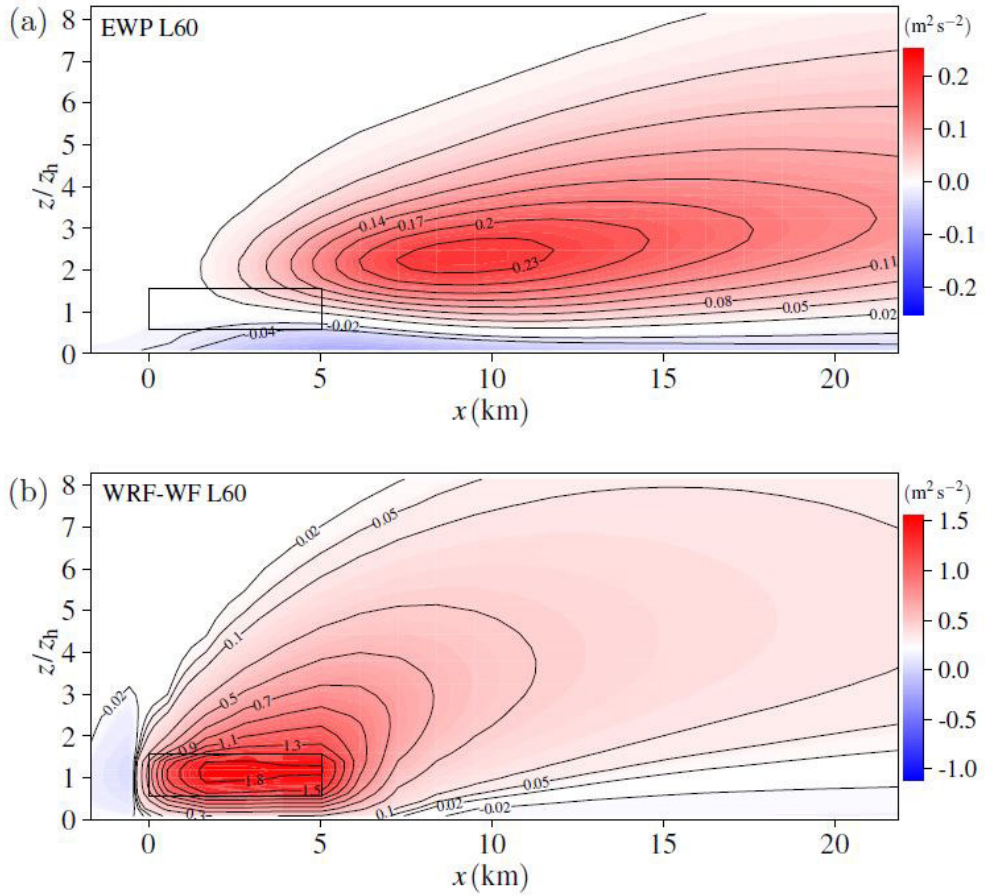

Figure 2.7: Vertical cross-section of the TKE difference for ideal simulations for 10 ms^{-1} along the wake direction for the (a) EWP scheme and (b) Fitch scheme. The region in the model containing turbine blades is indicated by the rectangle. Figure from Volker et al. (2015, p. 3725) in accordance with the Creative Commons Attribution (CC BY) license.

The concept of "wind theft" was studied by Pryor et al. (2020), who compared the sensitivity of wake effects and power production to the two wind farm parameterizations. Simulations of a 9-month period from December 2007 to August 2008 over a domain encompassing a cluster of onshore wind farms in the U.S. Midwest were conducted, using a number of combinations of horizontal and vertical resolutions. Analyzing the fraction of wake-affected grid cells, results showed that the extent of wakes was generally larger for Fitch than EWP, especially in the winter and summer months and less so in the spring months (as shown in Figure 7 in Pryor et al. (2020, p. 167)). Fitch also exhibited significantly higher increases in TKE at hub height and two times the hub height than EWP. The lower impact of wakes when using EWP resulted in 3-4% higher gross capacity factors and $\sim$ 5% higher power output. Simulations using Fitch showed a higher wake intensity than observations, resulting in a lower power production than would be expected in a real situation. To properly be able to evaluate the seasonality of the wake response, the authors stated that future work should include multiyear simulations and long-time power production data from individual wind farms. Similar results were shown in Shepherd et al. (2020), where faster wake recovery and 2-3% greater capacity factors were observed for clustered onshore wind farms when using EWP compared to Fitch.

Due to the fact that the Fitch scheme was developed earlier and is included in the official WRF releases in contrast to the EWP scheme, it is the most common wind farm parameterization used in studies of wakes, and its effects are more thoroughly documented than for the more recently developed EWP scheme. Vanderwende et al. (2016) observed that the Fitch scheme overestimated velocity deficits when comparing to large eddy simulations, an observation that was also made by Lee and Lundquist (2017) when comparing Fitch to measurements. Vanderwende et al. (2016) also found that TKE production was overestimated when using the Fitch parameterization.

CHAPTER 3

Methodology

Included in this chapter is a description of the data used in the study and the methods used to apply this data within the scope of the project. Chapter 3.1 presents the input and output data from the WRF simulations, SCADA data and met mast data. A summary of the WRF setup used for the simulations is presented in Chapter 3.2.

3.1 Data

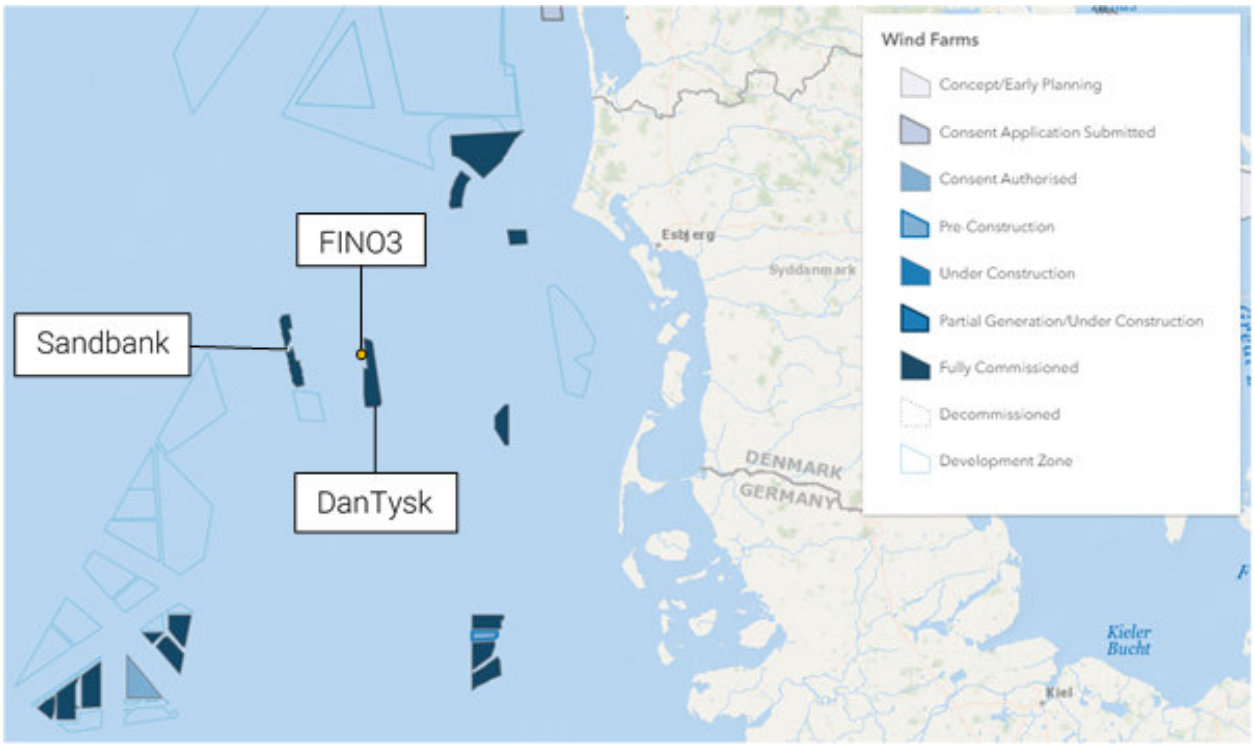

Figure 3.1: Wind farms Sandbank and DanTysk and research platform FINO3 in the North Sea. Source: http://www.4coffshore.com/offshorewind/

Supervisory Control And Data Acquisition (SCADA) data covering 2018 has been supplied by Vattenfall for the German wind farms Sandbank and DanTysk, which are separated by approximately 20 km. Power and thrust curves for the Sandbank and DanTysk wind turbines are provided by Vattenfall and are used together with SCADA wind speed measurements to estimate the power production of the turbines. Met mast measurements between 2010 and 2019 from the research platform FINO3, which is situated on the north-western edge of DanTysk, have been provided by BMWi (Bundesministerium für Wirtschaft und Energie) and PtJ (Projectträger Juleich) and are used to inspect the long-term climate. The locations of the wind farms and met mast can be seen in Figure 3.1. All data used has a 10-minute sample rate. The power and thrust curves for a SWT-3.6-120 turbine can be seen in Figure 3.2.

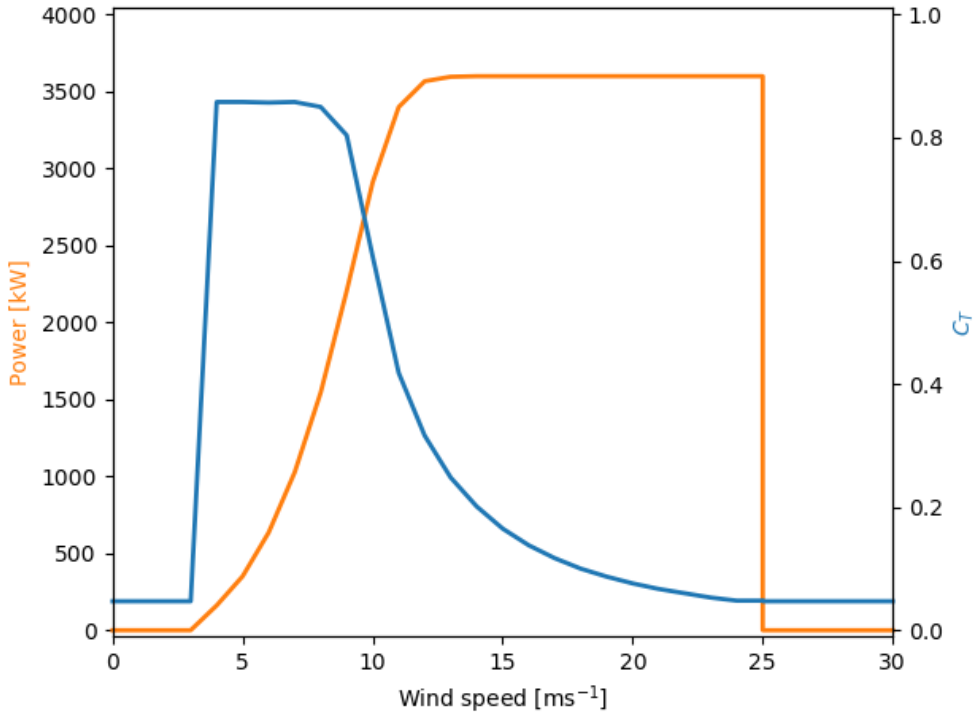

Figure 3.2: Power curve (orange) and thrust coefficient curve (blue) for an SWT-3.6-120 turbine.

Finally, data from a one-year WRF simulation of the atmosphere in 2018 over a domain in the North Sea conducted by Langor (2019) is used for the wake analysis. In order to include the potential influence of wakes from surrounding wind farms in the North Sea, a region covering a 150 km radius centred around the Sandbank/DanTysk area was considered in Langor's simulation, where all wind farms present in the year of study were included. This region can be seen in Figure 3.3 and the wind farms are listed in Table 3.1. The simulation was run for three separate scenarios; one simulation using the Fitch scheme to parameterize the wind farms in the domain, another using the EWP scheme to parameterize the wind farms, and a third simulation run with no wind farms, providing the behaviour of the undisturbed background flow. These three simulations will be referred to as FIT, EWP and NWF, respectively.

The datasets used in this study are listed in Table 3.2, and a detailed description of the met mast and wind farms being studied can be found in Table 3.3.

Figure 3.3: Wind farms included in simulations. Figure courtesy of Langor (2019, p. 19). Reprinted with permission.

Table 3.1: Wind farms included in simulations.

Wind farm	**Turbine model**	**No. of turbines**	**Capacity [MW]**
Alpha Ventus	M5000-116 Senvion 5 MW	12	60
Amrumbank West	SWT-3.6-120	80	288
BARD Offshore I	Bard 5.0	80	400
Borkum Riffgrund 1	SWT-4.0-120	78	312
Butendiek	SWT-3.6-120	80	288
DanTysk	SWT-3.6-120	80	288
Gemini	SWT-4.0-130	150	600
Global Tech I	Areva M5000-116	80	400
Gode Vind 1&2	SWT-6.0-154	97	582
Horns Rev I	V80-2.0	80	160
Horns Rev II	SWT-2.3-93	91	209
Meerwind Süd/Ost	SWT-3.6-120	80	288
Nordsee One	Senvion 6.2M126	54	332
Nordsee Ost	Senvion 6.2M126	48	295
Sandbank	SWT-4.0-130	72	288
Trianel Windpark Borkum I	AD5-116	40	200
Veja Mate	SWT-6.0-154	67	402

Table 3.2: Datasets used in this study.

Data source	**Site**	**Data**	**Start/end date**
SCADA	DanTysk	Wind speed	2018-01-01 00:00:00 2019-01-01 00:00:00
SCADA	Sandbank	Wind speed	2018-01-01 00:00:00 2019-01-01 00:00:00
Met mast	FINO3	Wind speed (91m, 105°) Wind speed (91m, 225°) Wind speed (91m, 345°) Wind direction (101m, 105°) Wind direction (101m, 225°) Sea surface temperature Air temperature (95m)	2010-01-01 00:00:00 2019-01-01 00:00:00
WRF input		SINALPHA (Sine of rotation angle) COSALPHA (Cosine of rotation angle) HGT (land height)	
WRF output	Inner domain	U (x wind component) V (y wind component) PH (perturbation geopotential) PHB (base-state geopotential) T (perturbation potential temperature) SST (sea surface temperature) TKE (turbulence kinetic energy) UST (friction velocity)	2018-01-01 00:00:00 2019-01-01 00:00:00

Table 3.3: Wind farm and met mast information.

	Sandbank	**DanTysk**	**FINO3**
Wind turbine model	SWT-4.0-130	SWT-3.6-120	
Wind turbine capacity	4.0 MW	3.6 MW	
Number of wind turbines	72	80	
Wind farm capacity	288 MW	288 MW	
Wind turbine hub height	95 m	88 m	
Rotor diameter	130 m	120 m	
Centre latitude	55.19°	55.14°	55.20°
Centre longitude	6.86°	7.20°	7.16°
Commission date	Jan 2017	Dec 2015	2009

3.1.1 Preliminary data processing

In order to use the data in the analysis, some data must be processed. The calculations of various variables needed in the analysis are shown below. Due to the staggering of WRF output variables, values are interpolated to the grid cell centres, both in the horizontal and vertical planes. These linear interpolations present the potential for small potential errors in the variables. There are 252 grid cells in the x-direction, 234 grid cells in the y-direction, and 16 vertical layers, resulting in 943 488 grid points after interpolation. There are 52 560 timesteps 10-minute timesteps in 2018.

Height (WRF)

The total geopotential height z [m] is an approximation of the actual height of a pressure surface above mean sea-level. It is calculated using the total geopotential $PH + PHB$, the gravitational acceleration constant, and the terrain height, which for grid cells over water is 0.

$$z = \frac{(PH + PHB)}{9.81} - \text{landheight} \tag{3.1}$$

Due to pressure changing in time, PH also changes with time, and the geopotential height z is not a constant. Computing a z value for every grid cell in each layer for an entire year would be too computationally heavy, and the height for each layer is approximated to the height in the grid cell containing FINO3. It is found that the heights in layer 9 are those closest to the hub heights of the turbines (88 m and 95 m), and layer 9 is used as the "hub-height layer" throughout this study. To investigate whether the presence of the met mast or nearby wind farms influence the geopotential height at this point, the layer 9 height at FINO3 is compared to that at an undisturbed location. The mean height and standard deviation of layer 9 at FINO3 is $\mu = 88.3$ m and $\sigma = 2.1$ m. The mean height for layer 9 for the undisturbed location follows the height at FINO3 very closely, with the mean deviating by just 0.2%. It is therefore concluded that the location at which the height z is calculated has little influence on the result, despite the presence of the wind farms and met mast. The height z used for determining hub height values in this study is shown in Figure 3.4.

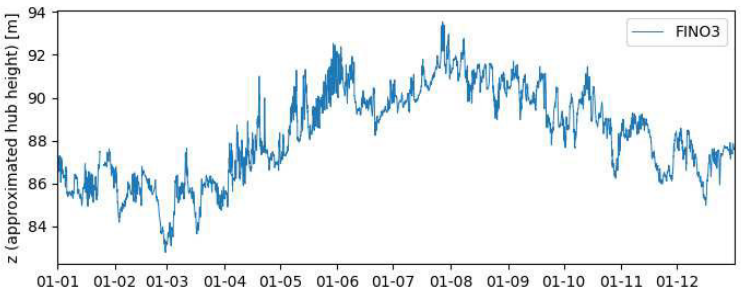

Figure 3.4: Height of layer 9 in the grid cell containing FINO3.

This fluctuation in hub height will result in uncertainties in the wind speed at hub height. As offshore turbine hub heights are often above the surface layer and merged in the Ekman layer, the undisturbed wind speed increases only very slightly with height (Zhang 2015). This means that despite the fluctuations in height seen in Figure 3.4, the free stream velocities at these various

heights are likely to be very similar. More significant uncertainties may arise when using this fluctuating height as hub height in the case of wake-affected flows, as the velocity deficit varies with height depending on the vertical wind profile. This is further complicated by the differences in wind profile when using the two different wind farm parameterization schemes. Despite these uncertainties, it was deemed necessary to use this simple approach in order to reduce computation time.

Wind speed and wind direction (WRF)

Using the x and y-components of the wind velocity, the wind speed [ms^{-1}] and wind direction [°] of each grid cell at hub height level is calculated, using the above-mentioned heights in layer 9 as hub height. The WRF outputs U_{WRF} and V_{WRF} are corrected using the sine and cosine of the Earth's rotation angle.

$$u = U_{\mathrm{WRF}} \cdot \mathrm{COSALPHA} - V_{\mathrm{WRF}} \cdot \mathrm{SINALPHA} \tag{3.2}$$

$$v = V_{\mathrm{WRF}} \cdot \mathrm{COSALPHA} - U_{\mathrm{WRF}} \cdot \mathrm{SINALPHA} \tag{3.3}$$

Using these corrected values, the wind speed and wind direction in each grid cell are calculated. 180 is added to the wind direction, as we use the direction that the wind is coming from rather than the direction the wind is moving towards, and the angle is given in the interval $(0, 360]$.

$$\mathrm{wspd} = \sqrt{u^2 + v^2} \tag{3.4}$$

$$\mathrm{wdir} = \frac{\arctan2(u, v)}{4 \cdot \arctan(1)/180} + 180 \tag{3.5}$$

Temperature (WRF)

The total potential temperature θ [K] is obtained by adding 300 to the WRF output temperature.

$$\theta = \theta_{\mathrm{WRF}} + 300 \tag{3.6}$$

Turbulence kinetic energy (WRF)

The TKE [$\mathrm{m}^2\mathrm{s}^{-2}$] is equal to half the WRF output $\mathrm{QKE}_{\mathrm{WRF}}$.

$$\mathrm{TKE} = \mathrm{QKE}_{\mathrm{WRF}}/2 \tag{3.7}$$

Wind speed and wind direction (FINO3)

Wind speeds measured at 91 m at the FINO3 met mast are used as hub height observations. The FINO3 data is made up of 10-minute-averaged cup anemometer measurements, which are made

at three different angles around the mast (105°, 225°and 345°) in order to reduce the influence of tower distortion effects on the wind speed (blue lines in Figure 3.5). The three datasets are combined into one timeseries (orange line) depending on the measured wind direction (green line). Whenever data is missing from the dataset corresponding to the wind direction, data from the next-nearest direction is used. A number of small gaps are still present in the sorted FINO3 wind speed measurements where no data was available.

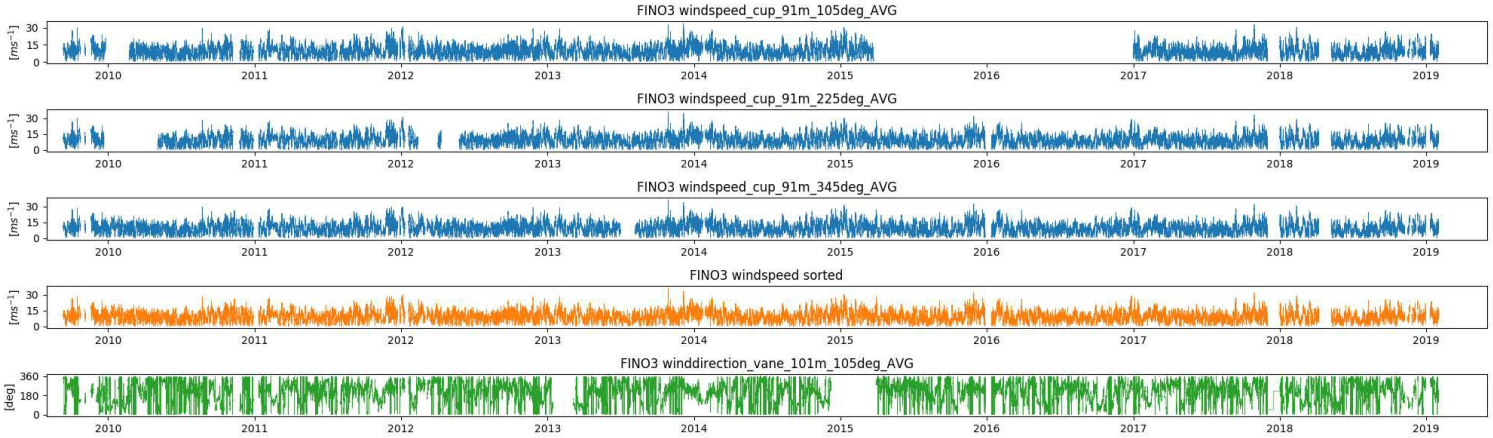

Figure 3.5: Wind speed and wind direction measurements from FINO3 for 2018.

Stability (FINO3)

Through Equation 2.4, the Bulk Richardson Number is calculated for each 10-minute timestep using measurements from FINO3 for sea-surface temperature and hub height air temperature and wind speed. The measurements and resulting Ri_B can be seen in Figure 3.6. Due mainly to missing wind speed measurements, the data coverage for the stability in 2018 at the FINO3 location is 76%. Using the methods discussed in Chapter 2.3, the stability classes are defined for each timestep according to the Bulk Richardson Number.

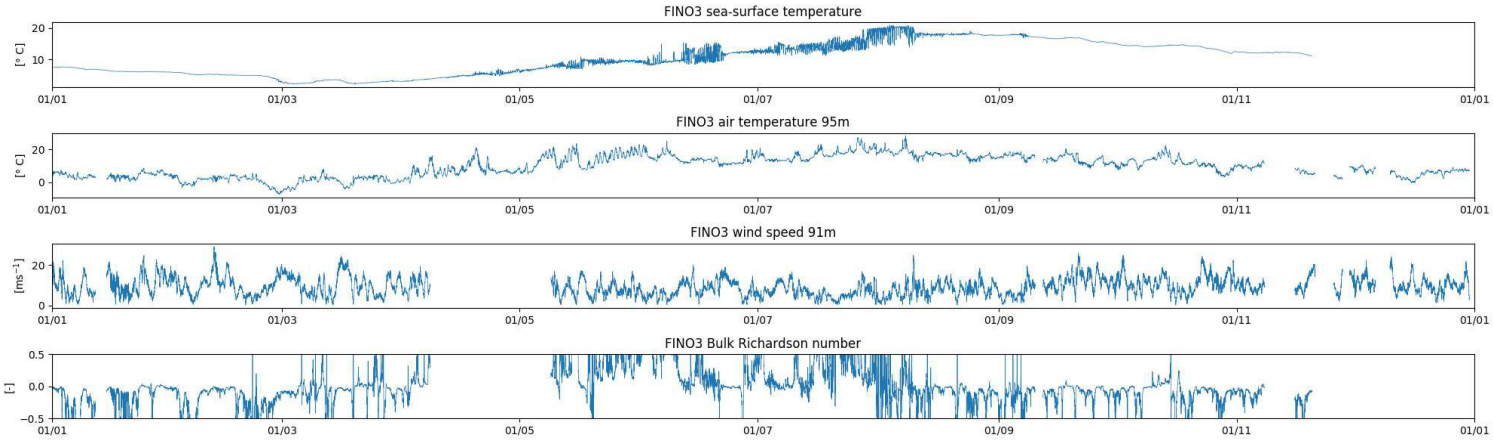

Figure 3.6: 2018 measurements from FINO3 for calculating Bulk Richardson Number.

3.2 WRF model setup

In this section, an overview of the WRF settings is presented, including physics settings for the simulations run by Langor. Langor's simulations last for the entirety of 2018 and use CFSR and OISST data for reanalysis data and sea-surface temperature data. All physics schemes are applied to the outer domain (d01), middle domain (d02) and inner domain (d03) with the exception of the cumulus parameterization and the wind farm parameterization. TKE advection was not used in the simulation by Langor, which will influence the analysis of TKE later in this report. A summary of the settings are shown in Table 3.4.

Table 3.4: Settings for WRF simulations run by Langor.

WRF version	V 3.7
Simulation period	2018-01-01 00:00:00 2019-01-01 00:00:00
Reanalysis data	CFSR + OISST
Microphysics	New Thompson et al.
Longwave Radiation	RRTMG
Shortwave Radiation	RRTMG
Surface Layer	MYNN
Land Surface	Noah Land Surface Model
Planetary Boundary Layer	MYNN Level 3 PBL
Cumulus Parameterization	Kain-Fritsch (d01)
Wind Farm Parameterization	NWF/EWP/FIT (d03)
Initial Length Scale σ	1.6 (EWP scheme only)
TKE Advection	Off

All simulations are run over three domains, seen in Figure 3.7, where output from the inner domain, with a grid cell size of 2×2 km, is used for the analysis. A 1440×1260 km domain is centred around the coordinates 55.5°N, 6.0°E. The horizontal resolution for each grid cell for d01, d02 and d03 is 18 km, 6 km, 2 km respectively, and the vertical resolution is split into 16 layers. The outer domain is made up of 70×80 grid cells (east-west $\times$ south-north), the middle 144×162, and the inner 234×252. Based on recommended practices in Hahmann et al. (2014), the year-long simulation was made up of consecutive 11-day simulations, with the first 24-hour spin-up period of each run being discarded. Note that data from the 24^{th} and 25^{th} of January could not be retrieved from the FIT simulation, and these dates have been excluded from the analysis. The output from these simulations contains 10-minute-averaged data, and variables are staggered in an Arakawa C-grid (shown in Figure 3.8).

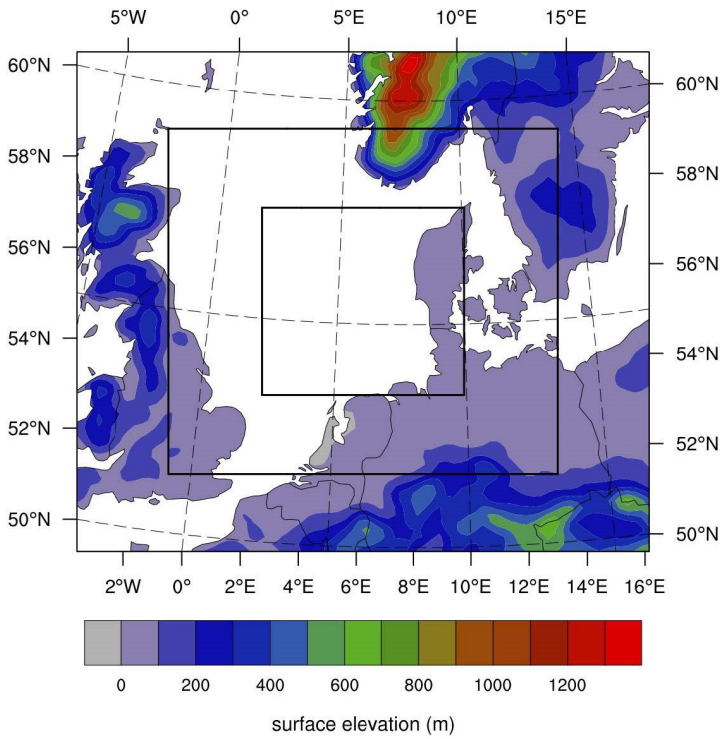

Figure 3.7: Outer, middle and inner domains of WRF simulations. Figure courtesy of Langor (2019, p. 25). Reprinted with permission.

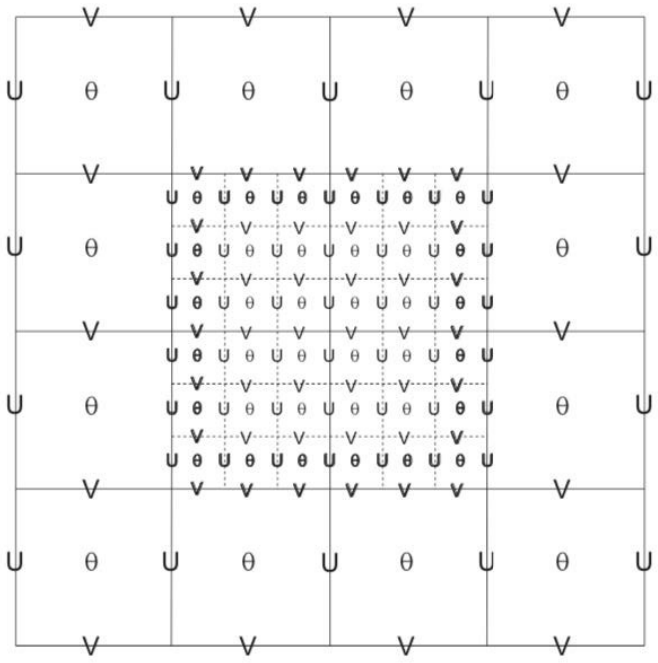

Figure 3.8: Arakawa C-grid staggering. Figure from Skamarock et al. (2008, p. 59) in accordance with the Creative Commons Attribution license.

CHAPTER 4

Climatological study

A study of the climatology of the simulated region is presented, including analysis of 2018 data and long-term data spanning a 9-year period from the beginning of 2010 to the end of 2018 from the FINO3 met mast. This includes an assessment of the distribution of wind speeds and wind directions and the monthly distribution of stability conditions. Additionally, the possible influence of the presence of wind farms on the local climate is discussed.

4.1 2018 climate

The variation in wind speeds at a specific site can be described using a Weibull distribution. The Weibull distribution is most often described by two parameters; the Weibull scale parameter A and the Weibull shape parameter k. The scale parameter is a measure for the characteristic wind speed of the distribution, while the shape parameter describes the breadth of the distribution. A Weibull distribution for 2018 has been fitted to the wind speeds measured at 91 m at FINO3 which were shown in Figure 3.5 (orange curve). The wind speed data coverage for 2018 is 84.2%, largely due to a long gap in the spring. The Weibull distribution of wind speeds in 2018 is shown in Figure 4.1. The Weibull fitted curve appears to agree well with the data, and the scale and shape parameters are $A = 10.38$ ms^{-1} and $k = 2.13$, respectively.

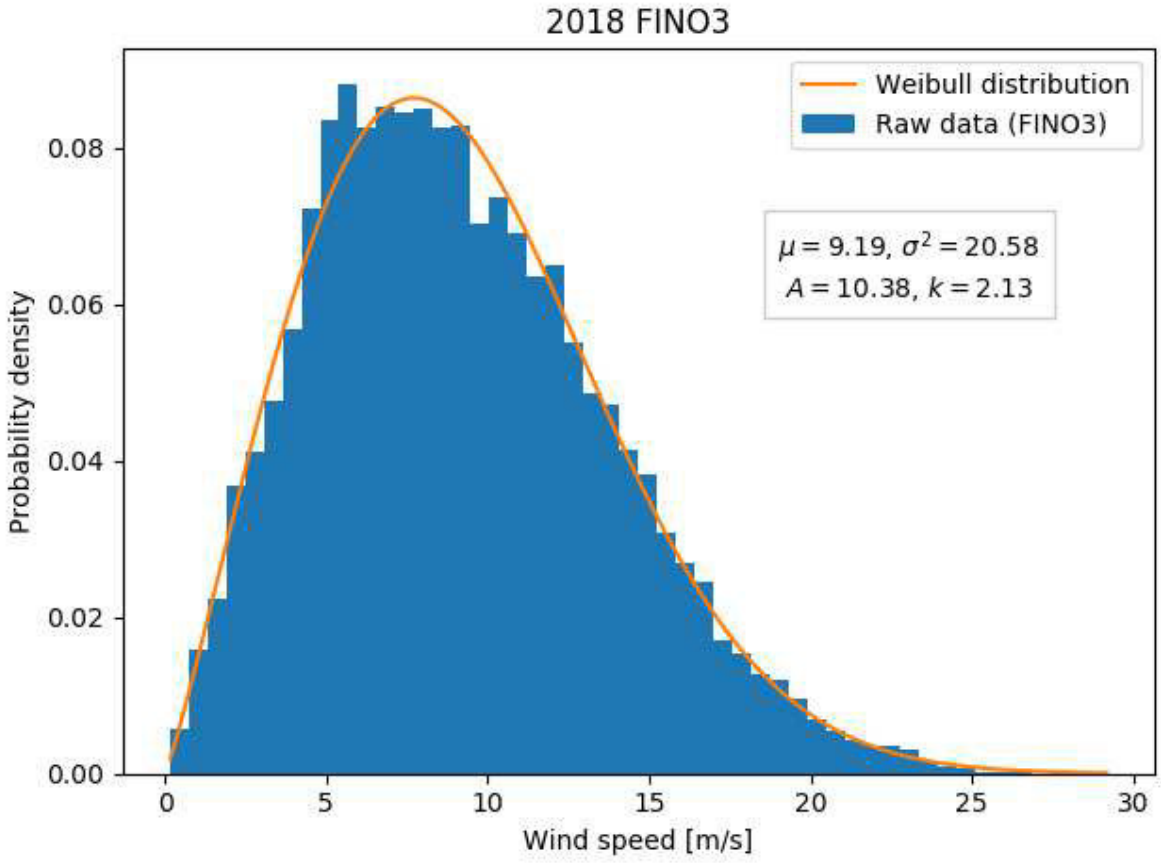

Figure 4.1: Weibull distribution of wind speeds at 91 m observed at FINO3 for 2018. Values for the mean μ, variance σ^2, and Weibull scale parameter A are in [ms^{-1}].

Using a wind rose, the distribution of wind directions and velocities is depicted in Figure 4.2. As is expected at these latitudes, the prevailing winds are predominantly from the westerly directions. The wind rose also indicates that winds often come from the east, while the wind rarely blows from the south and north/northeast. The highest wind speeds are generally from the west. Lower wind speeds from the east/southeast may be due to the presence of the DanTysk wind farm, as FINO3 is located immediately to the west of the wind farm, and due to the shorter fetch as a result of land to the east.

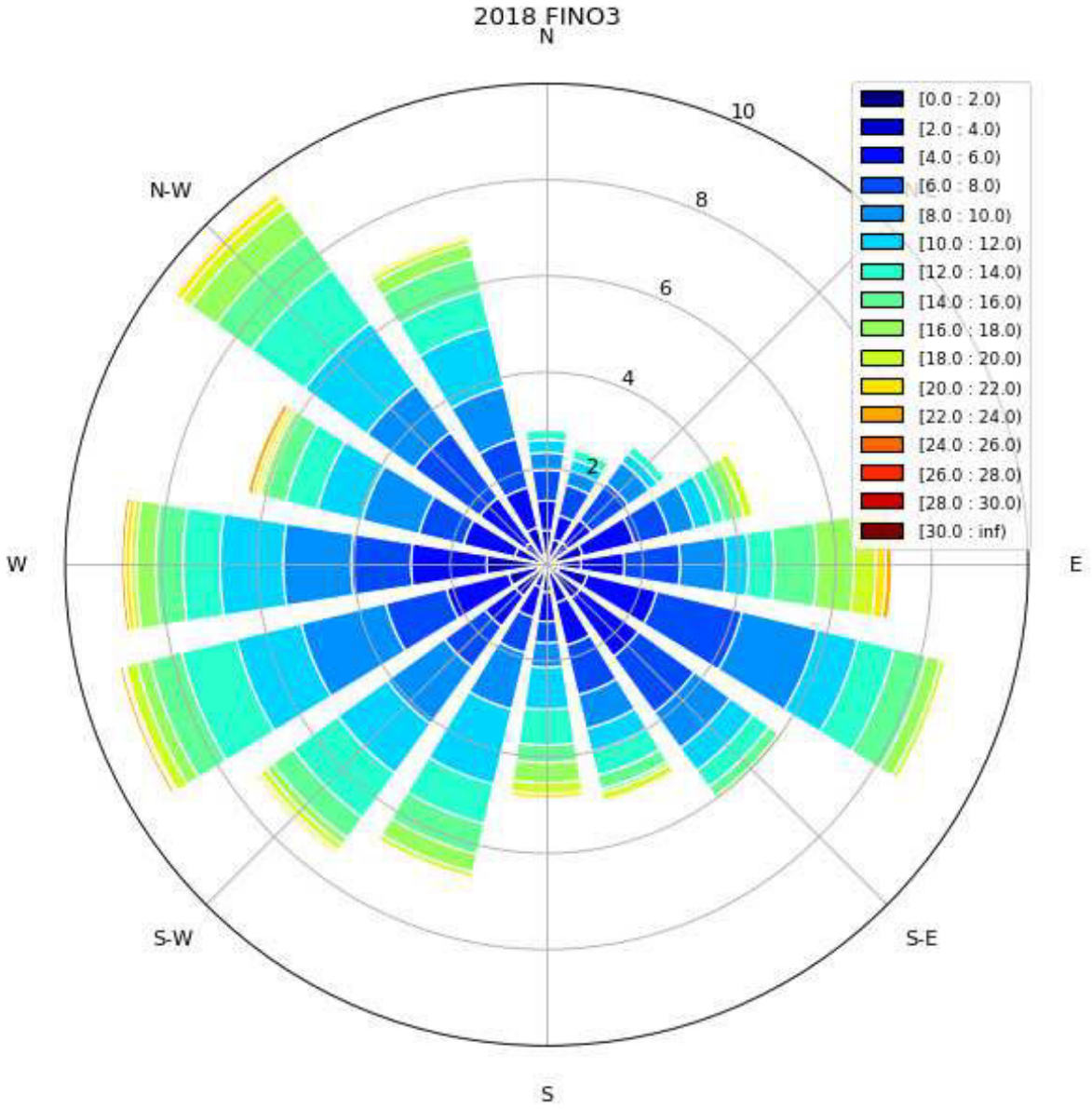

Figure 4.2: Wind rose (% frequency) as observed at 91 m at FINO3 for 2018.

Stability conditions have been assessed at the FINO3 location using calculated values for the Bulk Richardson Number and the Monin-Obhukov length. The distributions of the Bulk Richardson Number and Monin-Obukhov length at FINO3 are displayed in Figure 4.3, indicating an unstable atmospheric stratification. Using the three defined stability classes “unstable”, “stable” and “neutral”, the monthly distribution of stability for 2018 is shown in Figure 4.4. As discussed in Chapter 2.3, the atmospheric stability offshore is expected to be more stable in the spring and early summer, which appears to be the case. Due to low data coverage in April, November and December, one stable month and two unstable months are poorly represented by the FINO3 data, and this may lead to some seasonal bias.

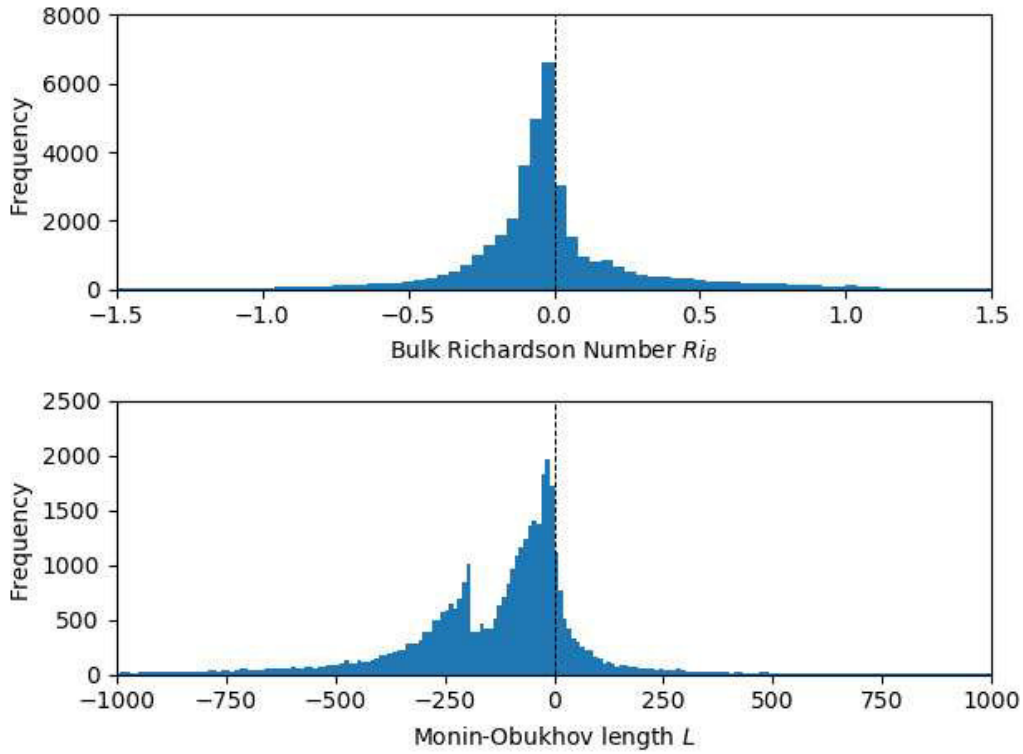

Figure 4.3: Distribution of Bulk Richardson Number and Monin-Obukhov length for FINO3 observations in 2018.

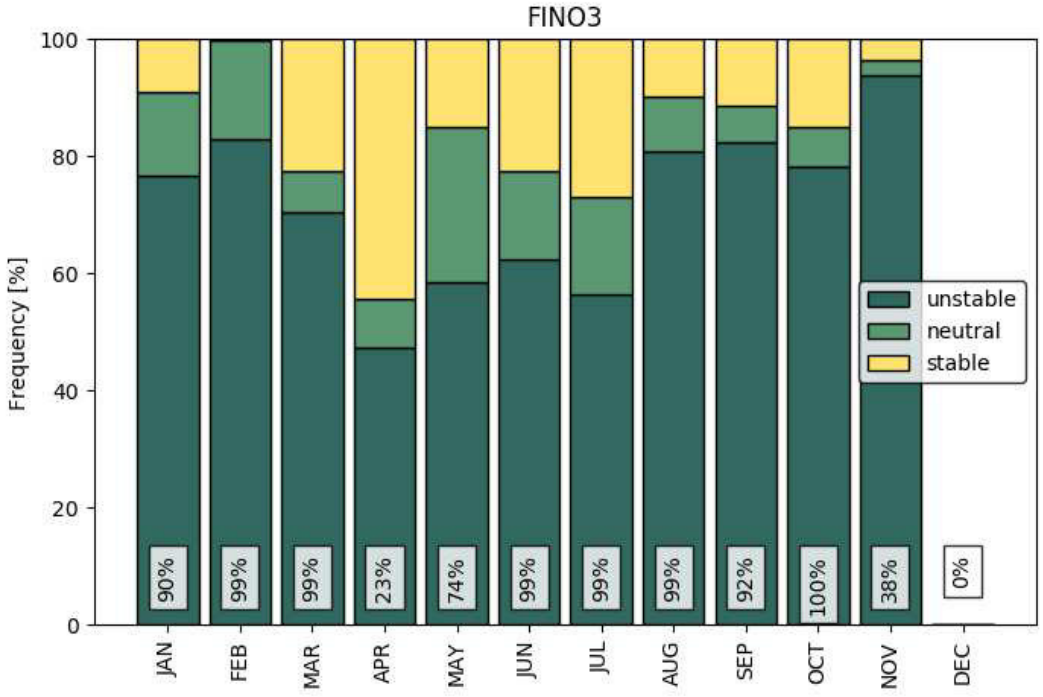

Figure 4.4: Monthly distribution of stability at FINO3 for 2018, with data availability displayed in percent for each month.

4.2 Long-term climate

In order to understand the 2018 climate, it must be put into perspective and compared with the long-term climate of the same region. FINO3 data is available for the years 2010-2018, and winds from this period are analysed and compared to 2018.

The Weibull distributions and parameters of each year can be seen in Appendix Figure A.1. The wind speed distribution differs from year to year due to the inter-annual variability of the wind climate, and possibly due to the influence of the surrounding wind farms; DanTysk began operating in December 2015, and Sandbank began in January 2017. The 9-year period being examined is split into three periods to assess the influence of the wind farms' presence. Period 1 precedes the operation of the wind farms, while DanTysk is operational in period 2, and both wind farms are in operation in period 3. The periods have been approximated to full years. Table 4.1 shows the mean wind speed of these periods, and the Weibull distributions can be seen in Appendix Figure A.2.

Table 4.1: Mean wind speeds at 91 m at FINO3 for various periods.

	Start date	**End date**	$\overline{\mathbf{U}}$ [ms^{-1}]
Period 1 (no WF)	2010-01-01	2016-01-01	9.71
Period 2 (DT)	2016-01-01	2017-01-01	9.15
Period 3 (DT+SB)	2017-01-01	2019-01-01	9.27
Full period	2010-01-01	2019-01-01	9.55

The sharp decrease in mean wind speed between period 1 and subsequent periods may be due to the operation of DanTysk, while the addition of Sandbank does not seem to have a noticeable effect. As stated before however, these effects may also be due to the inter-annual variability, and the shorter lengths of periods 2 and 3 make it difficult to determine whether annual variations or the presence of wind farms are the main cause. For further investigation, the inter-annual variability observed at a different location with no surrounding infrastructure can be examined. That has not been carried out in this study.

In Figure 4.5, statistics and Weibull parameters are shown for 2018 and for the 2010-2018 period average. The yearly Weibull distributions are compared in Figure 4.6, which shows that 2018 (red line) experiences lower wind speeds than the period average (black line). It should therefore be noted that wind speeds analysed in this study are lower than what could be expected in an average year.

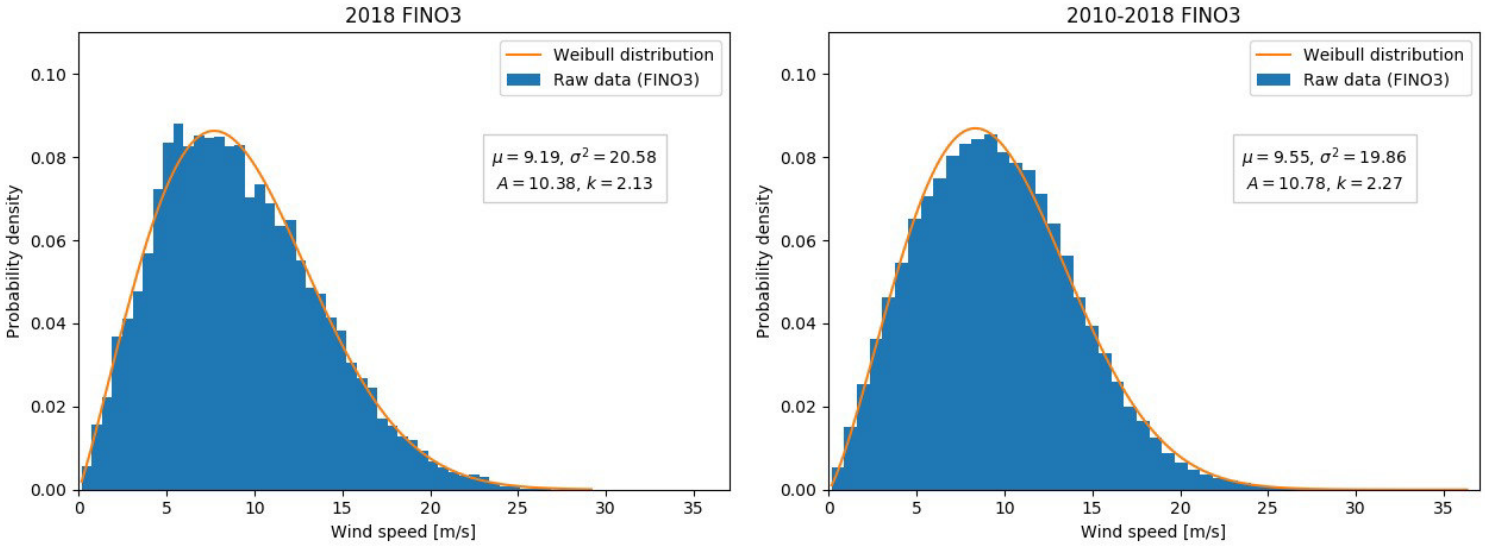

Figure 4.5: Histograms and Weibull distributions of wind speeds observed at 91 m at FINO3 for the year of 2018 (left) and for the 2010-2018 period (right). Values for the mean μ, variance σ^2, and Weibull scale parameter A are in [ms^{-1}].

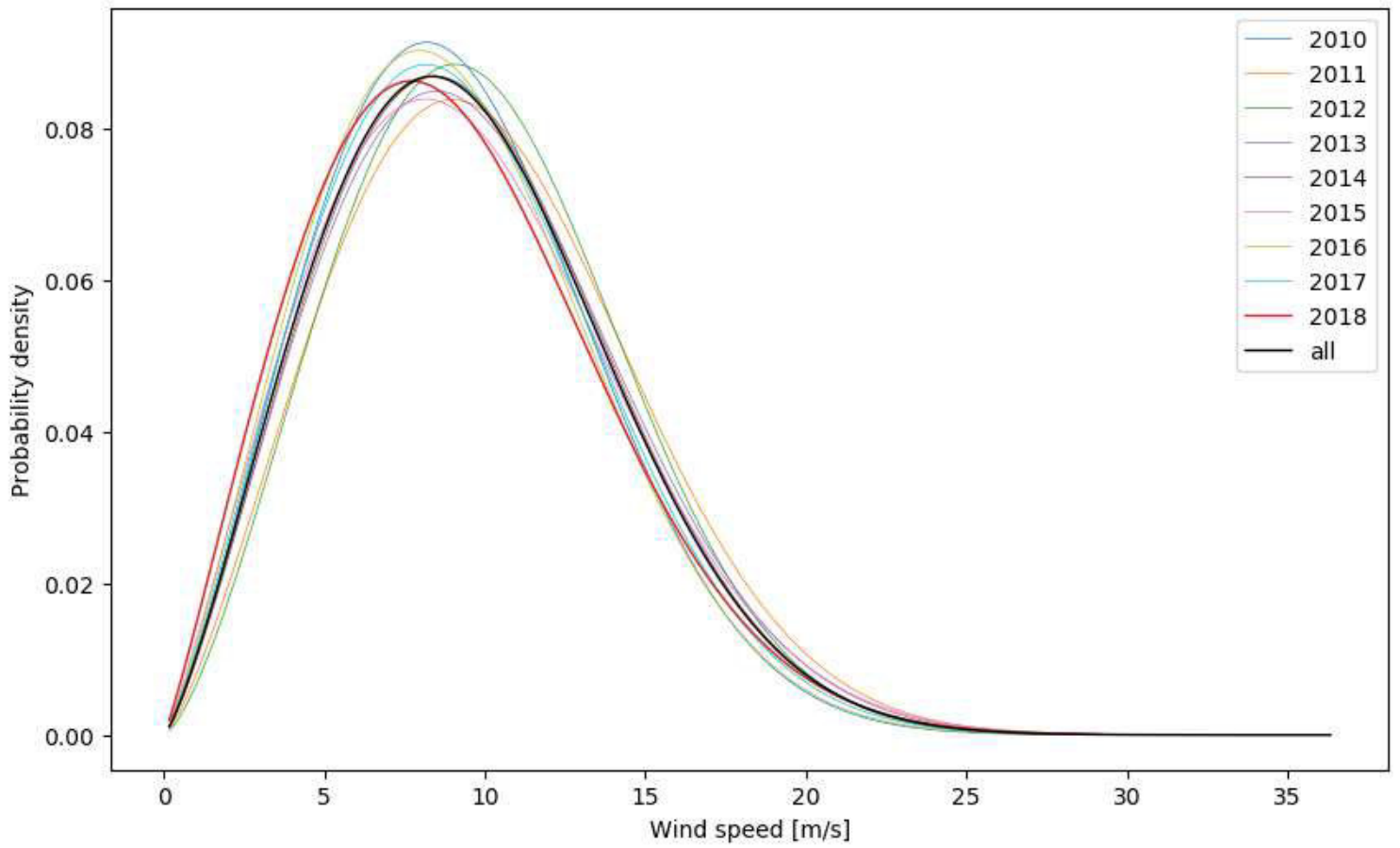

Figure 4.6: Weibull distributions of wind speeds observed at 91 m at FINO3 for 2010-2018 including period average.

In Figure 4.7, the wind rose is displayed for 2018 and for the 2010-2018 period average. 2018 experienced a much higher frequency of easterly winds than during the full 9-year period. A large number of these easterly wind speeds were below $10\,\mathrm{ms}^{-1}$ in 2018, while the full period does not show this pattern. As discussed previously, these low wind speeds in 2018 are possibly due to the presence of the DanTysk wind farm, which would decrease the velocity of easterly winds before hitting the FINO3 met mast. The wind roses for each year and for the defined periods can be seen in Appendix Figures A.3 and A.4.

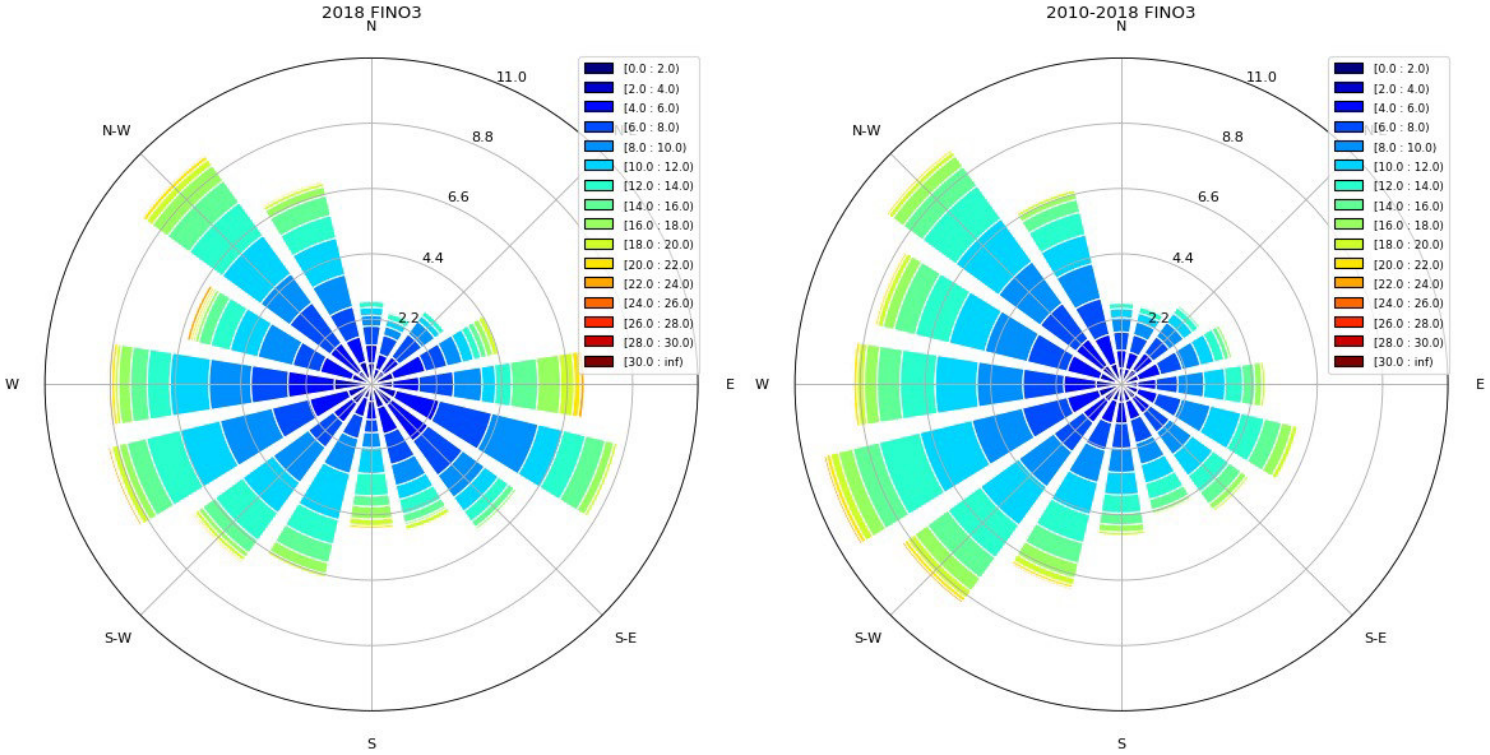

Figure 4.7: Wind roses for observations at FINO3 for the year of 2018 and for 2010-2018 period.

CHAPTER 5

WRF validation

A validation study has been carried out in order to determine the accuracy of the WRF simulation. Data from the WRF simulations has been compared to FINO3 measurements for the year of 2018 using the parameters wind speed, wind direction, and atmospheric stability in order to assess how realistic the simulated climate is.

5.1 Wind speed

In Figure 5.1, the Weibull distributions of the hub height wind speed as measured by the FINO3 met mast (at a height of 91 m) and the hub height wind speeds for the grid cell containing FINO3 output by the WRF simulations (at an average height of 88.3 m) are displayed, showing that WRF slightly overestimates the wind speed relative to the measurements. The difference between FINO3 and WRF velocities is also displayed, where the velocity difference has been calculated as $U_{\mathrm{WRF}} - U_{\mathrm{FINO3}}$. The average difference for EWP and FIT is $\mu = 0.14\,\mathrm{ms}^{-1}$ and $\mu = 0.01\,\mathrm{ms}^{-1}$ respectively, indicating that FIT predicts wind speeds in this grid cell very accurately, while EWP overpredicts by $0.14\,\mathrm{ms}^{-1}$ on average. The spread of the velocity difference, expressed by the standard deviation, is roughly the same for both parameterization schemes. Statistics and Weibull parameters for FINO3 and WRF are shown in Table 5.1, showing that simulations including wind farms on average overestimate wind speeds compared to observed values at FINO3.

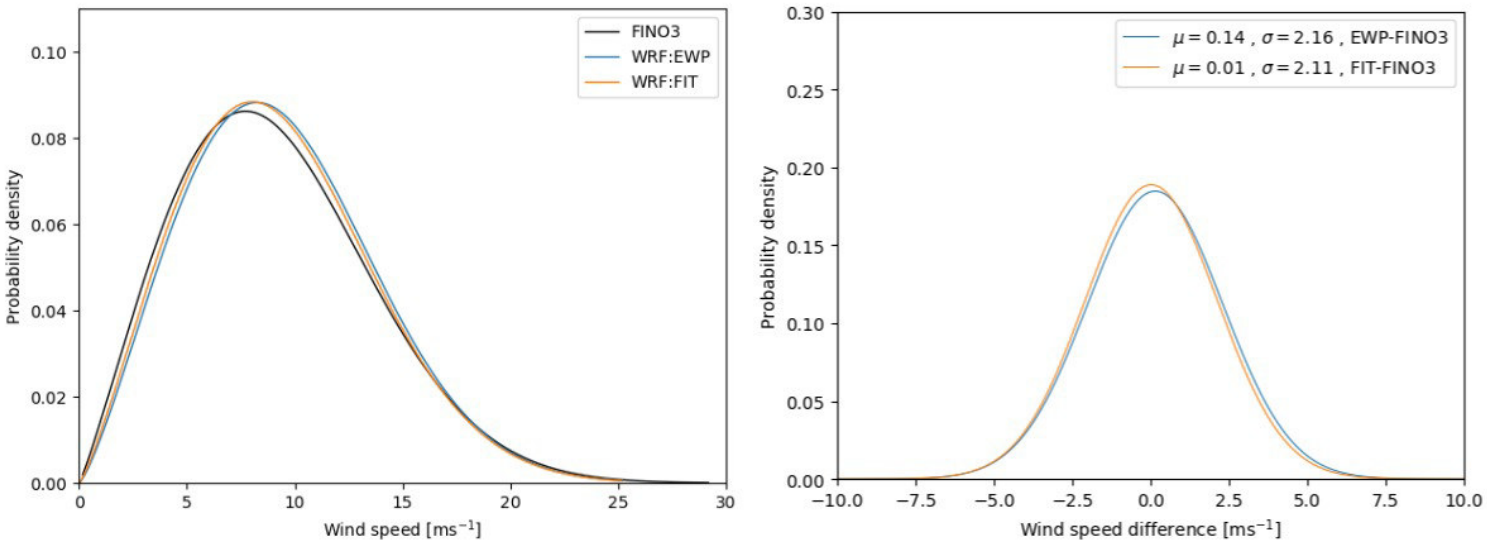

Figure 5.1: Weibull distributions of FINO3 and WRF (left) and probability density functions of the difference in wind speed between FINO3 and WRF (right). Values for the mean μ and standard deviation σ are in [ms^{-1}].

Table 5.1: Weibull parameters for FINO3 and WRF. Values for A, μ and σ^2 are in [ms^{-1}].

	FINO3	**EWP**	**FIT**	**NWF**
Shape parameter A	10.38	10.63	10.47	11.0
Scale parameter k	2.13	2.28	2.23	2.35
Mean velocity μ	9.19	9.42	9.27	9.74
Variance σ^2	20.58	19.22	19.26	19.42

The data points for the difference between FINO3 and EWP wind speeds are shown in Figure 5.2 along with a trend line for 30 wind speed bins, showing the mean and standard deviation. WRF generally overpredicts the wind speed for winds below $5\,\mathrm{ms}^{-1}$ and underpredicts winds above $20\,\mathrm{ms}^{-1}$.

The difference around 7-8 ms^{-1} is roughly 0, and at wind speeds above 22 ms^{-1}, WRF vastly underpredicts the wind speed. Wind speeds this high occur only very rarely (as shown in the Weibull distribution) and are mostly above cut-out wind speed, so these limitations in WRF are not considered problematic in this thesis. When studying extreme winds or storms, this should be taken into account.

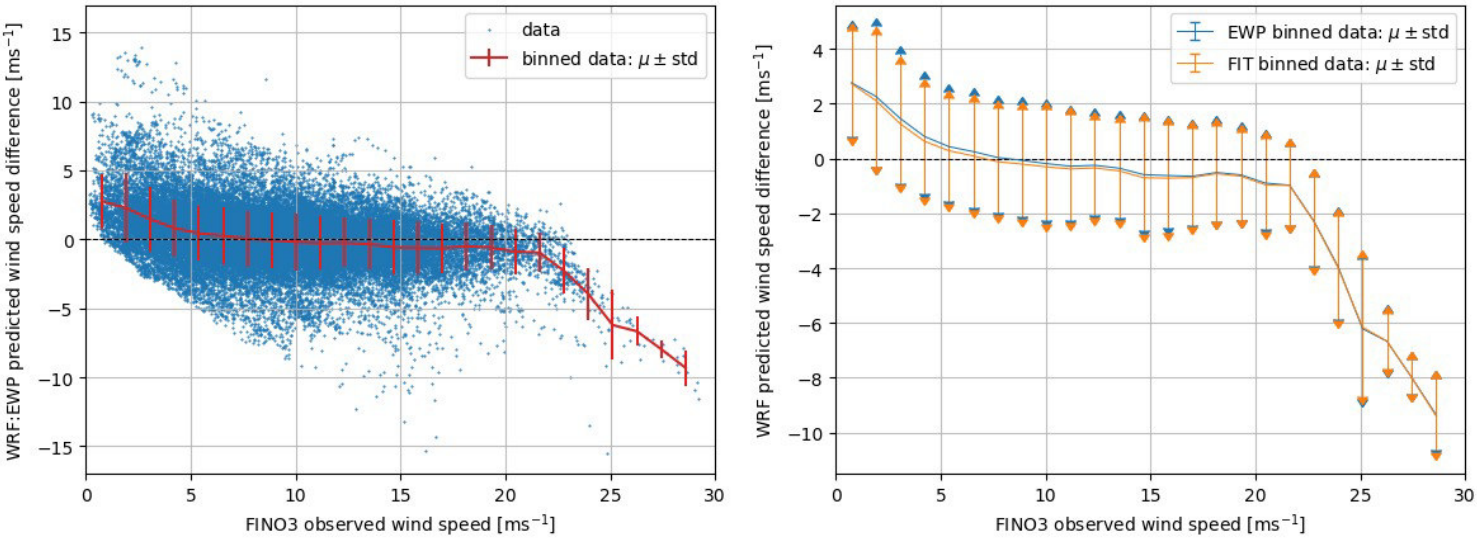

Figure 5.2: Scatter plot and trend line with error bars for wind speed difference between FINO3 observations and EWP predictions (left) and trend lines with error bars for wind speed difference between FINO3 and both wind farm parameterization schemes (right).

A closer examination of the discrepancy between the FINO3 measurements and the WRF simulations can be seen in Figure 5.3, where the two schemes are compared. Wind speeds below 4 ms^{-1} are below the cut-in speed for both turbine types and are excluded from this examination. Wind speeds above 20 ms^{-1} are excluded, as the difference between EWP and FIT becomes negligible. For wind speeds of 7 ms^{-1} and below, WRF underpredicts the wind speed compared to the observed values. In this range of velocities, FIT predictions are more accurate than EWP, with the difference $\leq 0.5\,\mathrm{ms}^{-1}$. For wind speeds above 8 ms^{-1}, WRF underpredicts the wind speed, and EWP predictions are more accurate than FIT, with the difference growing to up to 1 ms^{-1}. However, the difference between the two schemes does not exceed 0.2 ms^{-1}, and the trend lines for both EWP and FIT follow each other closely.

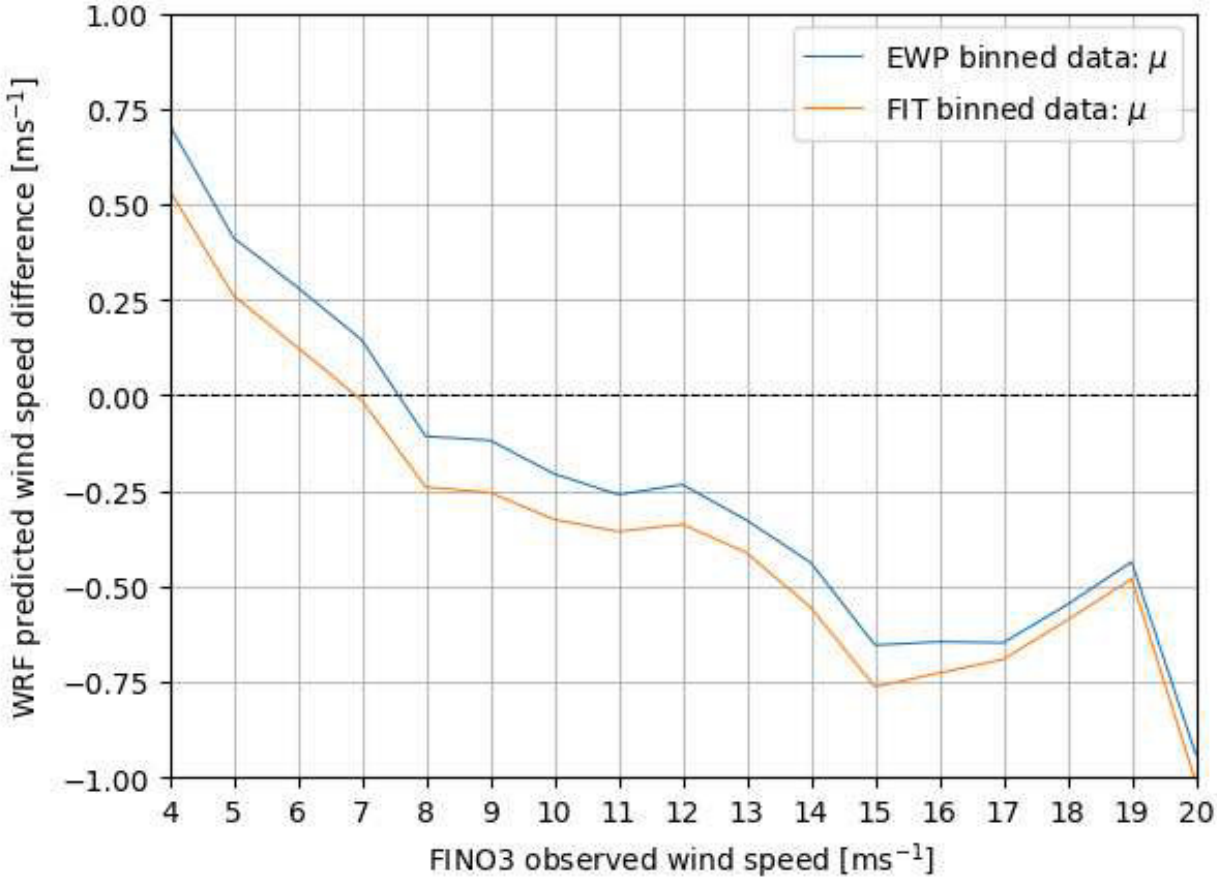

Figure 5.3: Trend line for wind speed difference between FINO3 and wind farm parameterization schemes.

5.2 Wind direction

A comparison of wind directions and wind speeds is made using wind roses of FINO3 observations and WRF simulations. In Figure 5.4, the FINO3 wind rose is compared to the wind roses from the WRF simulations, and there appears to be relatively good agreement regarding both wind direction and wind speed. The wind roses also show the effect of the wind farms in comparison to the NWF simulation, where EWP and FIT have a higher frequency of lower wind speeds (shades of blue).

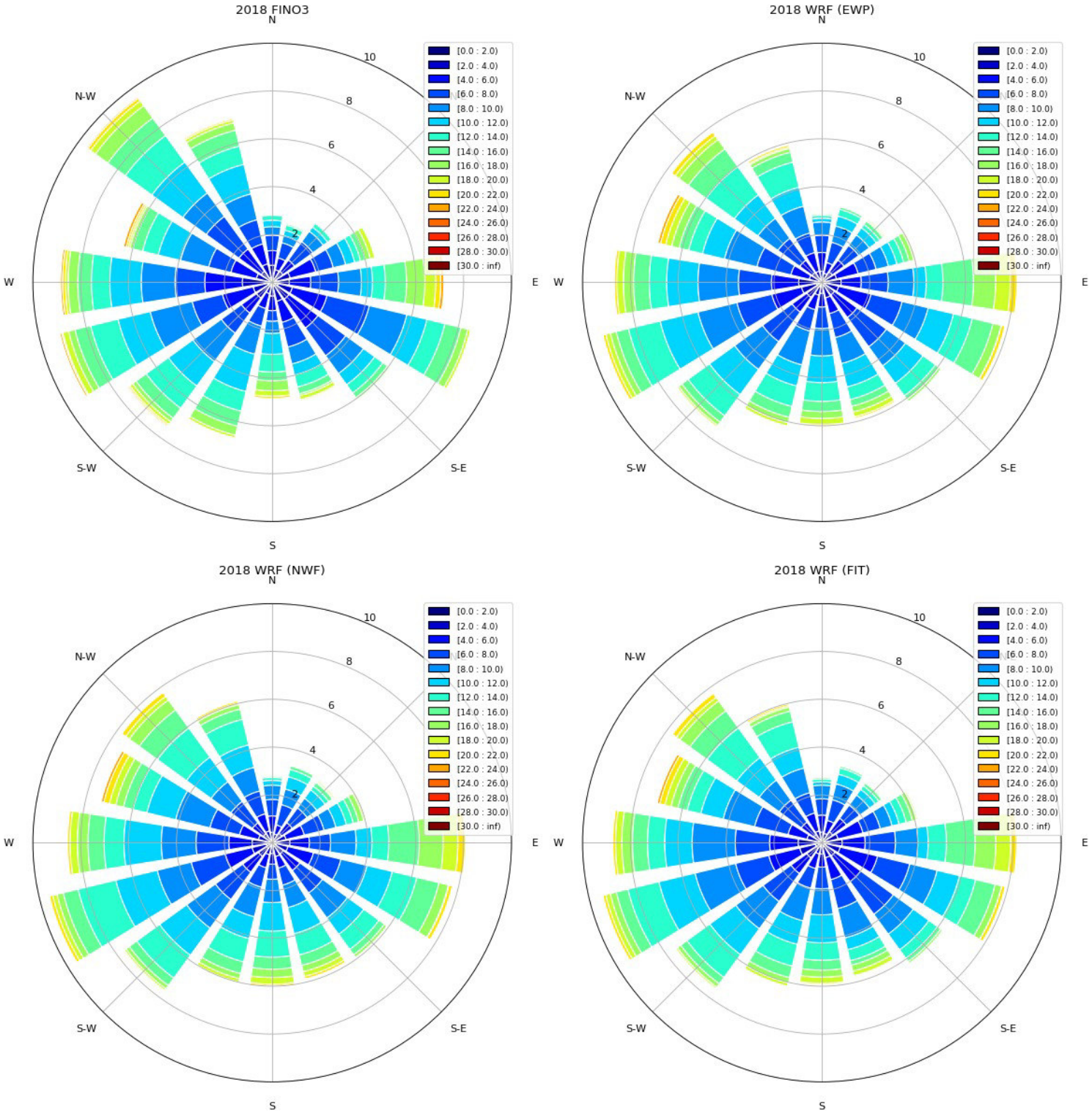

Figure 5.4: Wind roses for observations and simulations at the FINO3 location for 2018.

5.3 Atmospheric stability

To validate the stability conditions on site, the observed stability and the simulated stability (calculated as discussed in Chapters 3.1.1 and 2.3, respectively) are compared. Figure 5.5 shows good agreement between FINO3 and WRF, with FINO3 slightly more unstable than WRF. We also see that conditions become slightly more unstable with the inclusion of wind farms in the simulations compared to NWF. EWP is marginally more stable than FIT.

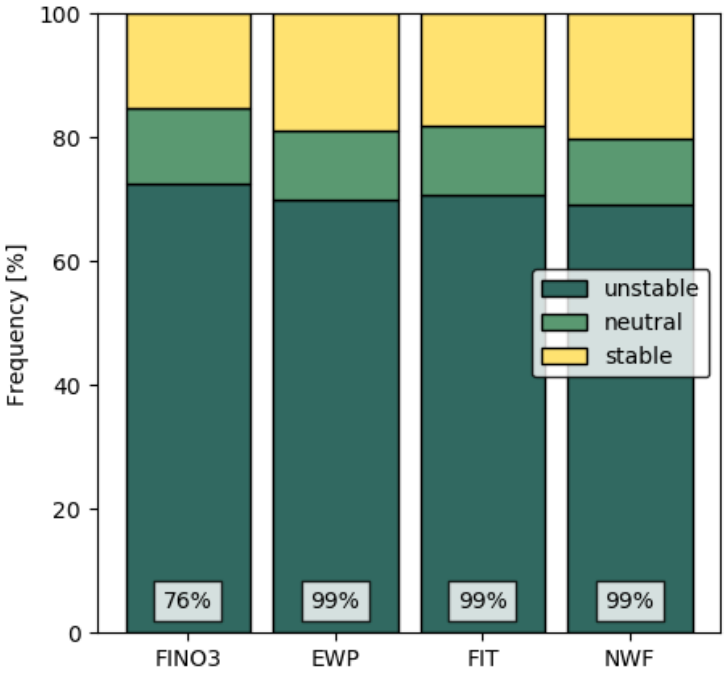

Figure 5.5: Observed and simulated stability at the location of FINO3 for 2018, with data availability displayed in percent for each case.

The data availability is lower for the FINO3 measurements, and we must check to see whether the stability results are biased. As established in Chapter 4.1, there is lots of data missing from April and November, and no data available for December. That is one stable and two unstable months that are poorly represented for FINO3. A comparison of the monthly stability for FINO3 and WRF is made in Figure 5.6. Comparing FINO3 and EWP for example, the results look similar, but EWP has a higher frequency of stable conditions and lower frequency of unstable conditions for most months, which matches what is shown in Figure 5.5. June, July and August are more stable in FINO3, while January, February and March are more stable in EWP. The remaining months are more or less equal or too poorly represented for FINO3 to compare.

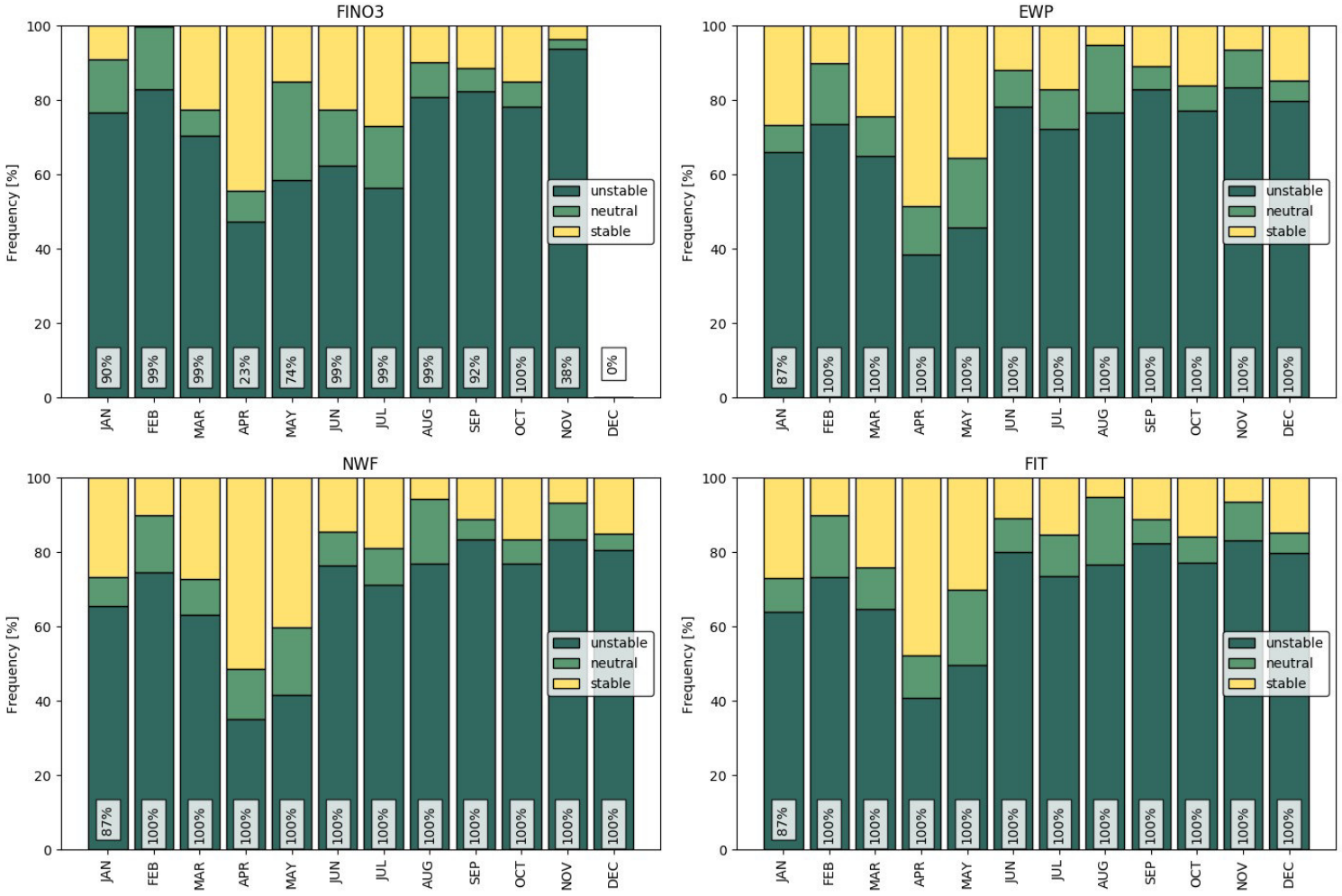

Figure 5.6: Monthly distribution of observed and simulated stability at the FINO3 location for 2018, with data availability displayed in percent for each month.

CHAPTER 6

WRF wake analysis

This chapter includes a discussion of the wake behaviour found from the WRF simulations, including analysis of the velocity deficit at hub height and the TKE field. In this study, the wake has been defined as the area affected by velocity deficits in excess of 2% compared to the simulation without wind farms, as also used by Christiansen and Hasager (2005) and Pryor et al. (2020). Velocity deficits have been calculated so that negative values represent decreased wind speeds with the inclusion of wind farms; for example, EWP velocity deficits are calculated as $U_{\mathrm{EWP}} - U_{\mathrm{NWF}}$.

6.1 Climatology

In Chapter 5, the EWP and FIT simulations were compared to the FINO3 observations in order to validate the simulation results. In order to determine the impact of the wind farms on the climatology, EWP and FIT simulation results are compared to the NWF simulation. Once again, data for the grid cell containing FINO3 is used for this study of climatological parameters.

The first evidence of velocity deficits due to the presence of wind turbines is seen in the Weibull distributions in Figure 6.1, where the distributions of EWP and FIT wind speeds are skewed further left than for the NWF scenario. Weibull parameters and statistics can be seen in Table 5.1, and the mean velocity is decreased by $0.33\,\mathrm{ms}^{-1}$ and $0.48\,\mathrm{ms}^{-1}$ for EWP and FIT respectively.

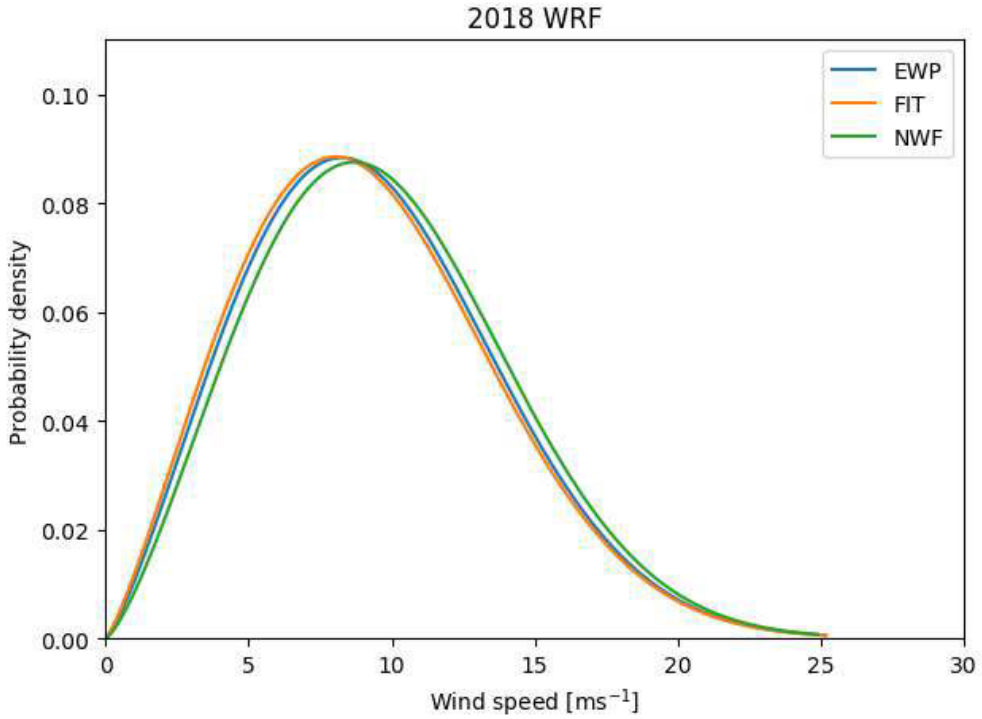

Figure 6.1: Weibull distributions of WRF simulated wind speeds at hub height.

The differences in wind speed between the simulations are shown in histograms in Figure 6.2. Comparing the Gaussian fits to the histograms of simulated data, it is clear that velocity deficits are not normally distributed but have a negative skewness, and the mean value is a poor measure for the central tendency. This was also noted by Pryor et al. (2020), who instead used median values to describe omnidirectional wake deficits. The median values have been shown in Figure 6.2 and are significantly smaller than the mean values. The average values occur at the centre of the normal distributions (dashed lines) and illustrate the misrepresentation of the velocity deficits when using mean values. When examining the histograms, FIT shows a higher frequency of deficits above $2\,\mathrm{ms}^{-1}$, causing a higher median deficit. These statistics show that the velocity deficit is generally greater for FIT simulations than EWP simulations, but may be exaggerated when using mean values rather than median values.

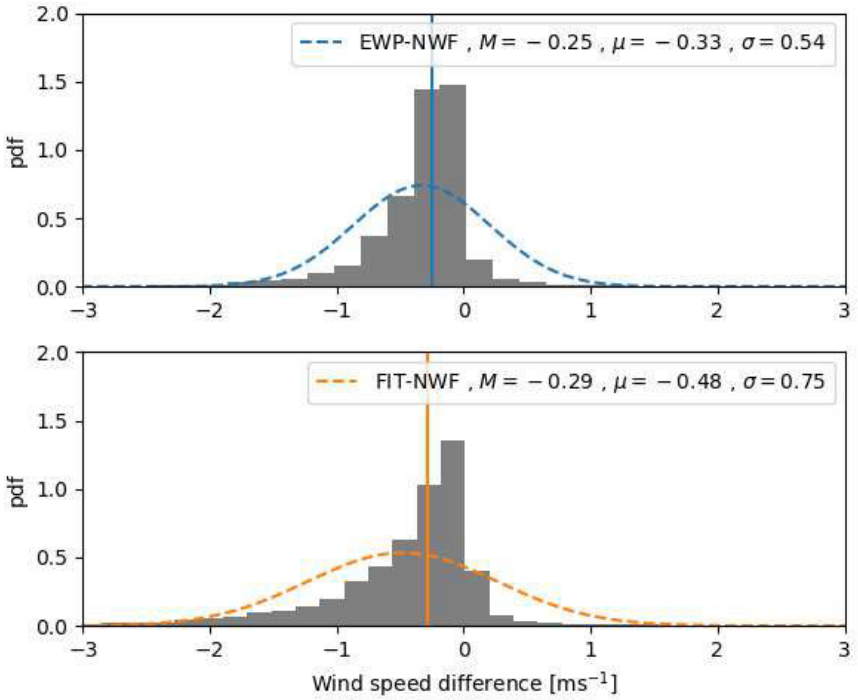

Figure 6.2: Probability density of hub height wind speed differences at the location of FINO3. Median values for deficits are depicted by solid vertical lines, and fitted normal distributions are depicted by dashed lines, with the mean value occurring at the peak of the normal distribution. Values for median M, mean μ, and standard deviation σ are displayed are in [ms^{-1}].

The deficit caused by the presence of the wind turbines is highly dependent on the wind speed. As discussed in Chapter 2, the magnitude of the velocity deficit is a function of the thrust force, as can be seen by looking at the thrust curve in Figure 3.2. The thrust coefficient is greatest in the range 4-9 ms^{-1}. The thrust force, seen in Figure 6.3, peaks at 10 ms^{-1}, where the strongest velocity deficits can be expected. The velocity deficits when using EWP and FIT are shown as a function of wind speed in Figure 6.4, where the greatest deficits in [ms^{-1}] do indeed occur at 10 ms^{-1}. Deficits are shown in absolute values and as percentages. From the trend lines it is clear that the range of wind speeds with the highest percentage-wise deficits is 5-10 ms^{-1}, with diminishing effects as wind speed increases. Throughout this study, the focus will be on percentage-wise velocity deficits, which is common in the field of wake studies.

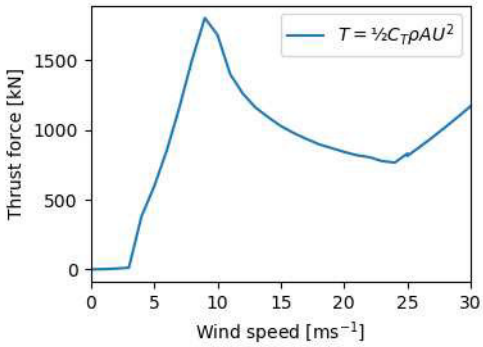

Figure 6.3: Thrust force as a function of wind speed calculated for an SWT-3.6-120 turbine.

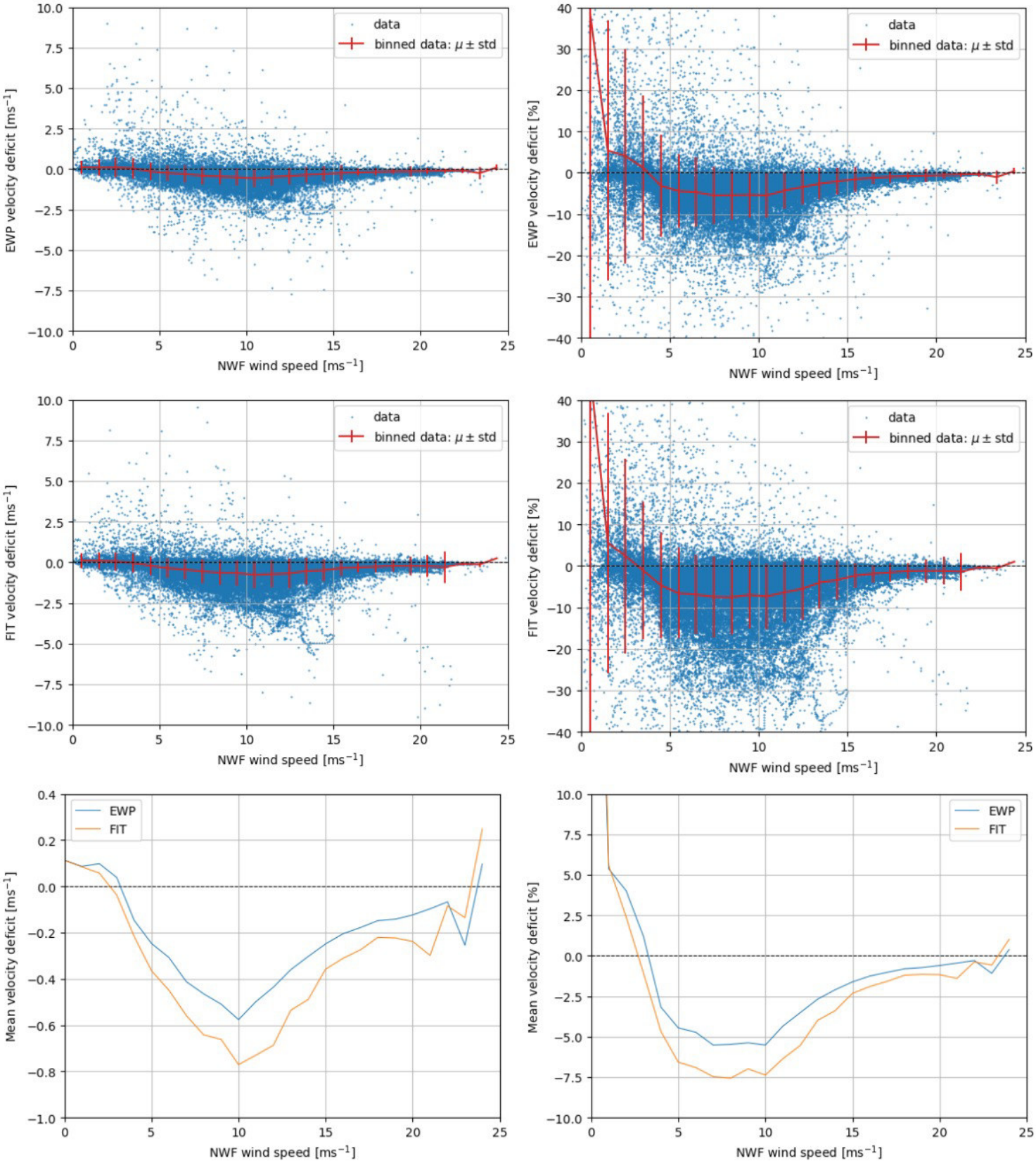

Figure 6.4: Velocity deficits as a function of wind speed expressed in absolute values [ms^{-1}] on the left, and percentages [%] on the right. The top and middle rows show scatter plots and trend lines with error bars for 25 bins, and the bottom row compares these trend lines of EWP and FIT.

6.2 Velocity deficit

Now that it has been established that the presence of wind turbines does in fact lead to a decrease in wind velocity, a more detailed study can begin.

Data has been split into a number of bins in order to analyse the effect of various wind speeds and stability conditions for different wind directions. Wind directions have been split into 30° sectors, wind speeds in intervals of $5\,\mathrm{ms}^{-1}$, and three stability classes as defined in Chapter 2.3. Wind speeds below $5\,\mathrm{ms}^{-1}$ and above $20\,\mathrm{ms}^{-1}$ have not been included in the analysis due to their rare occurrence and/or negligible climatological effect. All data bins are shown in Table 6.1, and data is filtered according to the grid cell containing FINO3. It is worth pointing out that despite filtering for the same data bins, this method of filtering can result in noticeable differences between EWP and FIT simulations, as can be seen in the datacounts of the wind speed deficit plots discussed below. These discrepancies may have been reduced by choosing to filter according to an undisturbed grid cell upwind of the wind farms; however this would not be without its own drawbacks, as the upwind grid cells for some wind sectors are affected by wakes from other wind farms.

The basis for the wind velocity deficit analysis is the difference in hub height wind speed between the NWF simulations and the EWP and FIT simulations, where mean values for each bin have been calculated. Based on the discussion regarding Figure 6.2, it could be argued that median values would have been more appropriate for this analysis, but this was only noted late on in the process of this thesis. Therefore it should be noted that using mean values may lead to exaggerated wake effects. An example of the mean velocity deficits that can occur have been visualized in plots in Figure 6.5, depicting a 160×160 km domain centred around the Sandbank/DanTysk wind farms, where the 2% wake limit is outlined. EWP simulations are shown on the top row and FIT on the bottom, while stability is unstable, stable and neutral from left to right. The number of occurrences of each bin is shown as the datacount in each plot. The plots shown in Figure 6.5 are for wind directions between 0-30° and wind speeds between 10-15 ms^{-1}, and similar plots have been made for all wind direction and wind speed bins. These plots are shown in their entirety in Appendix B.1. The low datacount for most neutral cases should be noted, and the pattern of wake behaviour under neutral cases is much less clear than for unstable and stable conditions.

Table 6.1: Data bins.

	Bins
Wind directions [°]	0-30, 30-60, 60-90, 90-120, 120-150, 150-180, 180-210, 210-240, 240-270, 270-300, 300-330, 330-360
Wind speed [$\mathbf{ms}^{-1}$]	5-10, 10-15, 15-20
Stability classes	Unstable, Stable, Neutral
Parameterization schemes	EWP, FIT

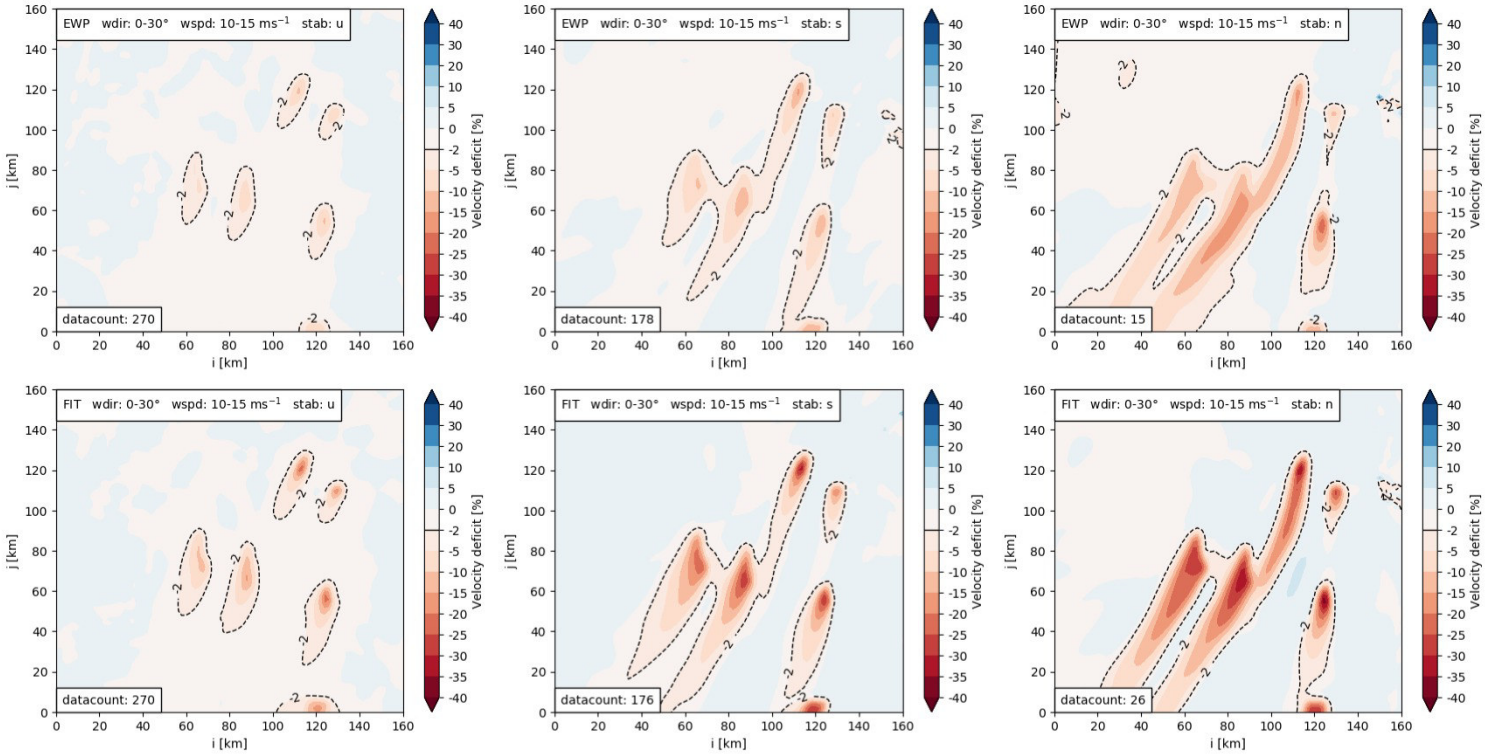

Figure 6.5: Wind speed deficit at hub height for wind directions 0-30° and wind speeds 10-15 ms^{-1} for a 160×160 km domain centred around the Sandbank and DanTysk wind farms. The dotted line shows the 2% wake-line, defining the edge of the wake-affected area.

6.2.1 Wake length

A common measure of the wake behind a wind farm is the wake length. Christiansen and Hasager (2005) observed wakes of 5-20 km behind Horns Rev and Nysted depending on ambient wind speed, atmospheric stability and number of turbines in operation, and Gayle Nygaard and Newcombe (2018) tracked wakes for 17 km behind Westermost Rough before reaching the limiting range of the dual-Doppler radars used in the study. Volker et al. (2015) found wakes of roughly 45 km behind Horns Rev I when simulating with both the EWP and Fitch schemes in WRF. Djath et al. (2018) found that stable conditions favoured longer wakes, observing isolated wakes in excess of 30 km behind Alpha Ventus. When including wake superposition from neighbouring wind parks, merged wakes could extend to more than 70 km downstream.

As Djath et al. (2018) discovered, when studying wake lengths behind a wind farm, the investigation can be complicated by the overlapping of wakes. If wind farm B is in the wake of wind farm A, wind farm B will experience a wind speed lower than the free stream velocity, causing the wake of wind farm B to extend further than it otherwise would. Furthermore, the length of the wake behind wind farm A cannot be measured, as it does not recover before encountering wind farm B. This makes it difficult to quantify wakes lengths for clustered wind farms, as is the case for Sandbank and DanTysk, and indeed the majority of wind farms in the North Sea. The difficulty of determining wake lengths in wind farm clusters can be seen by just glancing at Figure 6.6.

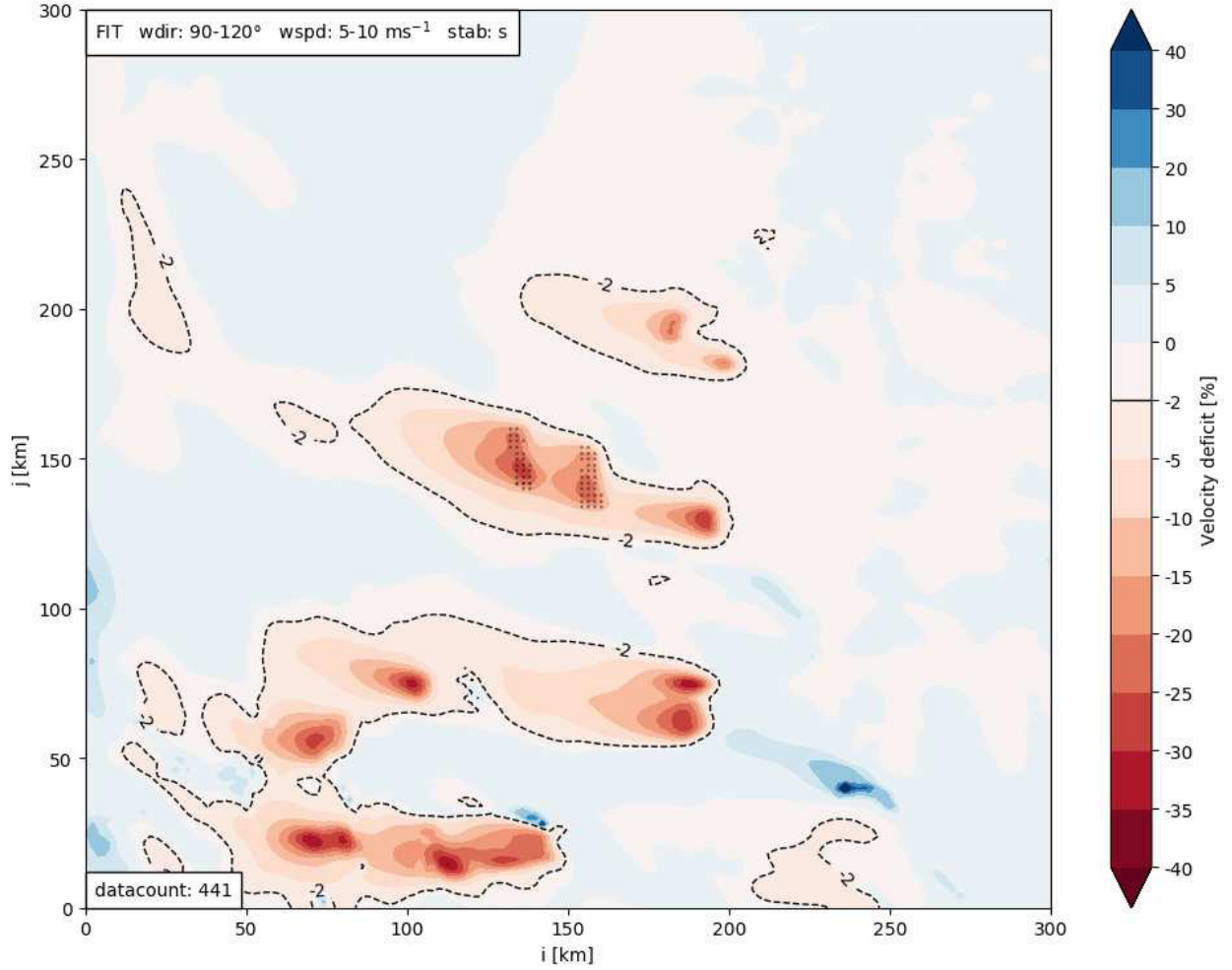

Figure 6.6: Wind speed deficit at hub height for a 300 × 300 km domain centred around Sandbank and DanTysk, where grid cells containing Sandbank and DanTysk turbines are marked.

Despite the difficulties discussed, an attempt to determine wake lengths behind Sandbank/DanTysk has been made by observing at the plots in Appendix B.1 and equivalent plots of the 300 × 300 km domain when necessary. The wake length behind Sandbank or DanTysk (whichever is clearest) has been measured by hand using a measurement stick with the appropriate scale, and the wake length has been approximated to the nearest 10 km. The wake is the straight line distance from the trailing edge of the wind farm to the 2% wake-line in the approximate wind direction, and the trailing edge of the wind farm is assumed equivalent to the trailing edge of the maximum deficit contour. When a wake does not recover before encountering a wind farm, the distance to that wind farm is noted as the wake length. The measured wake length does not take into account the upstream wind velocity, so the effects of upstream wind farms are not considered. The results are shown in Figure 6.7. Due to the low number of occurrences of wind speeds in the 15-20 ms^{-1} range and the negligible wake effects at these speeds (see Figure 6.4 and Appendix B.1), these bins have been excluded from this part of the analysis.

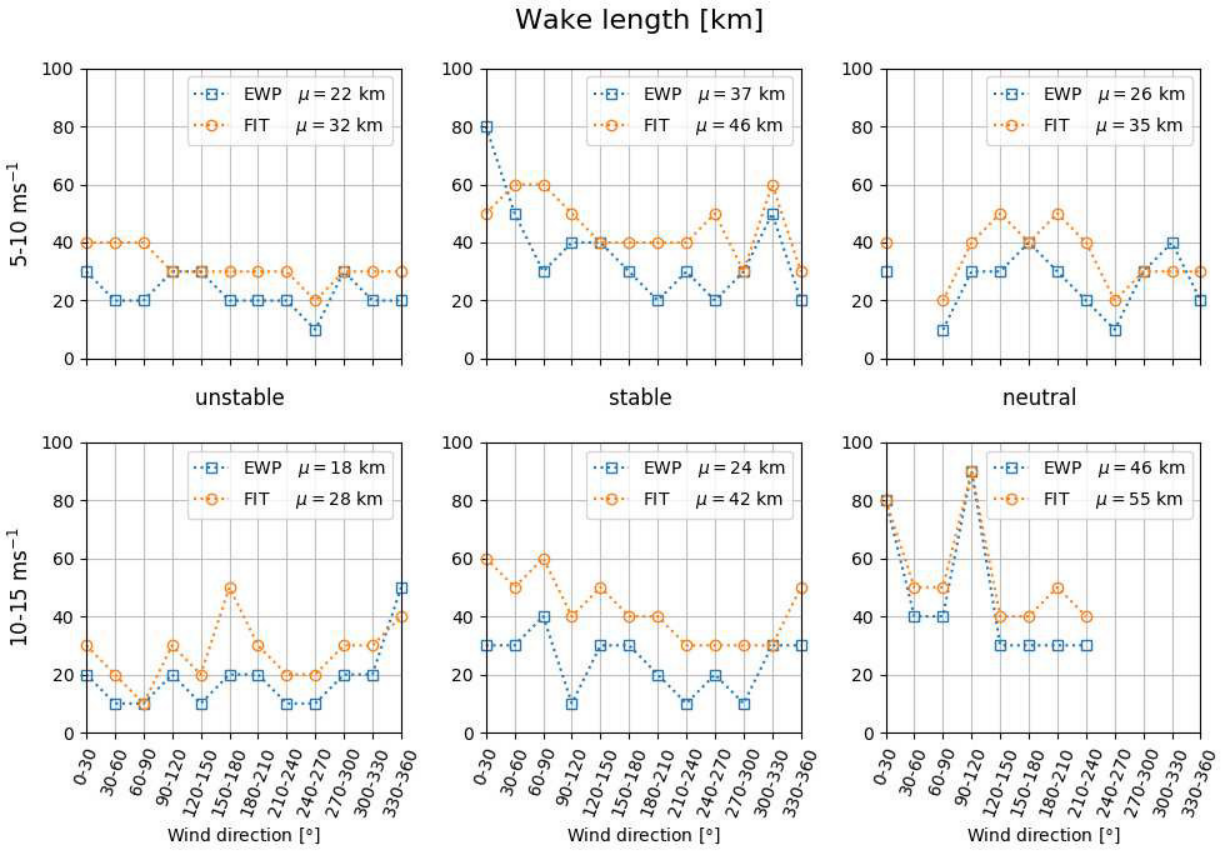

Figure 6.7: Wake lengths for wind speeds 5-10 ms^{-1} (top row) and 10-15 ms^{-1} (bottom row). The first, second and third columns represent unstable, stable and neutral conditions, respectively. The mean values displayed are unweighted averages and do not account for the number of occurrences in each direction, but are simply the mean of the points along the line.

It is apparent that the extent of the wake is very dependent on the wind direction, and this is largely due to the location of the surrounding wind farms. Wakes appear to extend further when simulating using FIT rather than EWP, which is in agreement with findings in other literature. In all 6 categories shown, the wakes are on average longer for FIT than EWP. For stable and unstable conditions, wakes are longer for wind speeds 5-10 ms^{-1}, while wakes under neutral conditions appear to be longer for wind speeds 10-15 ms^{-1}. It should be noted that for neutral conditions, several of the wind direction bins had no datacounts, so wake effects in these directions are unaccounted for. Only bins where data has been recorded for both EWP and FIT have been included in this part of the analysis in order to avoid bias towards either parameterization scheme. In Table 6.2, the effect of stability conditions and wind farm parameterizations on the wake length are quantified. The values shown are calculated from the mean values displayed in Figure 6.7 and are therefore also unweighted.

Table 6.2: Mean wake lengths [km] for wind speeds 5-15 ms^{-1}.

	Unstable	**Stable**	**Neutral**	**All conditions**
EWP	20	30	35	28
FIT	30	44	45	38

The average wake length regardless of atmospheric conditions is 28 km for EWP and 38 km for FIT, which is an increase of 36%. The shortest wakes occur under unstable conditions, while the longest occur under neutral conditions. The increase in wake length from unstable to stable conditions is roughly 50% for both EWP and FIT. Wakes under stable and neutral conditions are roughly the same for FIT, while EWP shows longer wakes under neutral conditions than under stable. With roughly 20 km between Sandbank and DanTysk, power production is likely to be affected when they are in the wake of one another. This is investigated in Chapter 7.

6.2.2 Wake-affected area

Another way of quantifying wake effects in a cluster of wind farms is assessing the wake-affected area. While quantifying wake lengths in multiple directions can be a complex task, a broader and simpler analysis can be conducted by evaluating how much of a certain domain is affected by velocity deficits in excess of 2%. In their report on "wind theft" of a cluster of onshore wind farms in Iowa, Pryor et al. (2020) conducted a similar analysis by observing the percentage of WRF grid cells affected by 3 different wake thresholds (2%, 5% and 10% median velocity deficits) for each of the 9 months included in the study (see Figure 7, Pryor et al. (2020, p. 167)). Testing for both wind farm parameterizations and several horizontal and vertical resolutions, they found that the area with velocity deficits of $\geq 2\%$ was generally larger for FIT simulations than for EWP, however with less variability between the two during the spring months. These are the months where the atmosphere is expected to be at its most stable, suggesting that EWP and FIT wakes may be more similar in magnitude under stable conditions; this is just speculation, however, and the reason for the reduced variability during spring is never addressed in their report.

For this analysis, the 160×160 km domain shown in the plots in Figure 6.5 and Appendix B.1 is investigated. For the data bins with highest availability, which are unstable and stable conditions and wind speeds 5-10 ms^{-1} and 10-15 ms^{-1}, the percentage of the domain affected by velocity deficits in excess of 2% is marked by a dashed line in Figures 6.8 and 6.9. Averaging over the 12 sectors gives the (unweighted) average wake-affected area, which is displayed in the upper right corner of each plot.

By observing the plots, it is clear that not only is the wake-affected area larger when simulating with FIT than with EWP, but the wake intensity is greater for FIT, with more high-deficit regions depicted by darker shades of orange/red. The average wake-affected area in the studied domain for FIT is almost 1.5 times that of EWP.

Comparing stable scenarios to unstable scenarios, the wake-affected area under stable conditions is almost twice as large as that under unstable conditions. In contrast to findings in Pryor et al. (2020), the difference between EWP and FIT is roughly the same for stable and unstable conditions;

the variability is not lower under stable conditions as it was in their findings. The reason for this is unclear, but the reduced variability in spring observed by Pryor et al. may be due to other variables than stability.

When examining the plots in Figures 6.8 and 6.9, it is apparent that the area affected by wakes is greater for the wind speed range of 5-10 m/s, meaning shorter wakes for wind speeds 10-15 ms^{-1}, which is in keeping with earlier findings and discussions in this report.

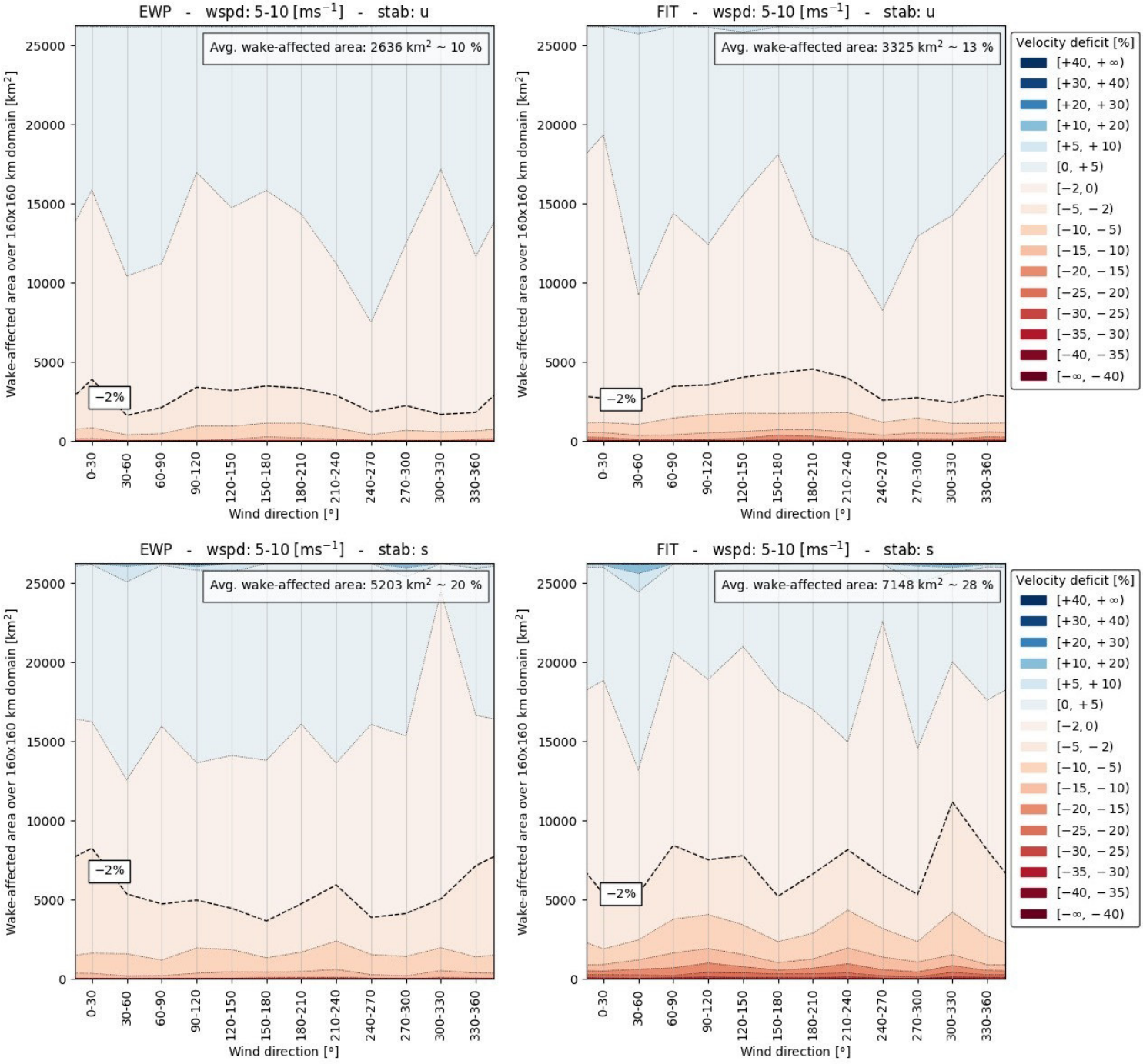

Figure 6.8: Wake-affected area of 160×160 km domain for wind speeds 5-10 ms^{-1}, displayed in [km^2] and percentage [%] of the domain. The average values displayed are unweighted averages and do not account for the number of occurrences in each direction, but are simply the mean of the 12 points along the dashed line representing the 2% deficit wake-line.

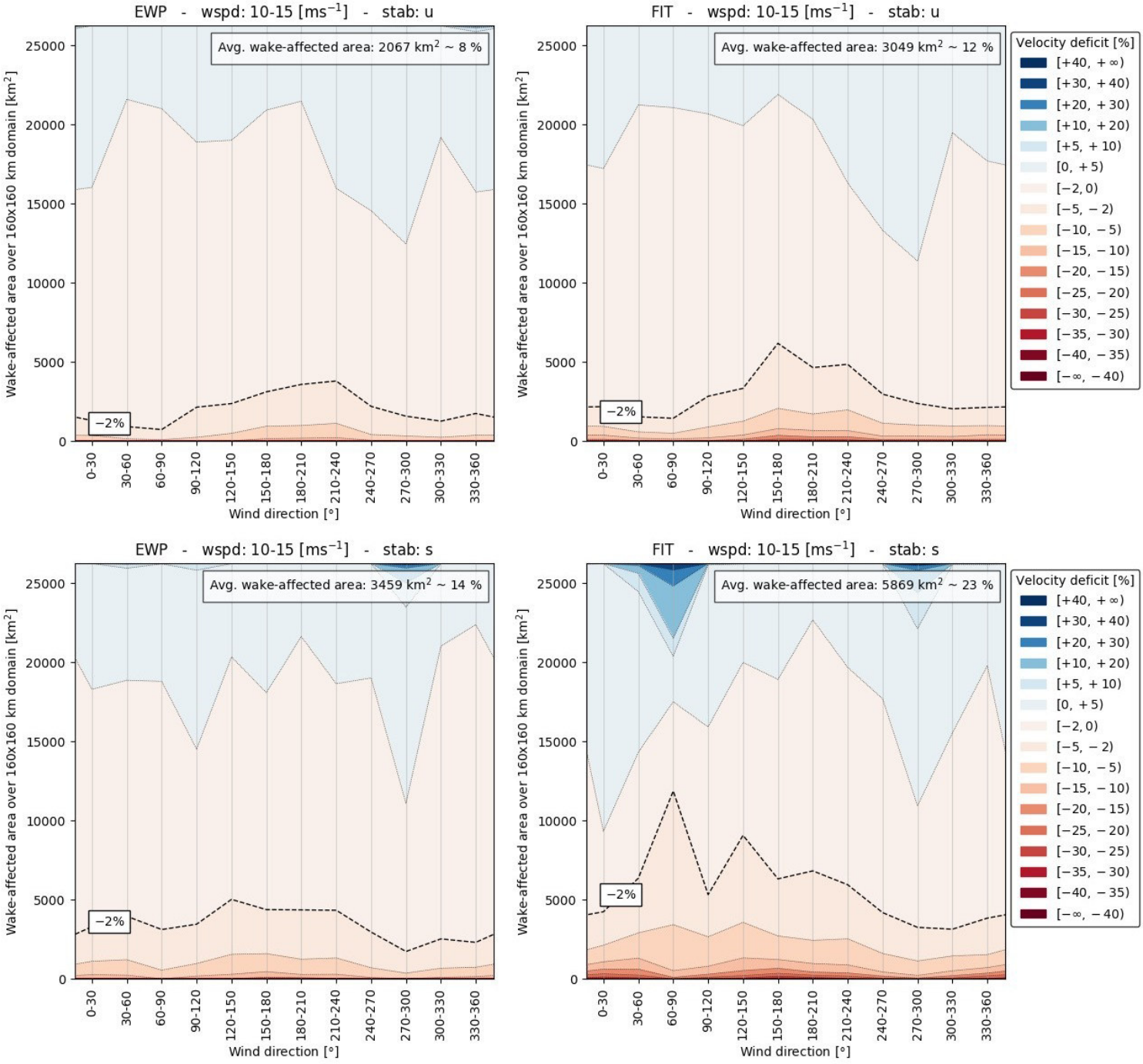

Figure 6.9: Wake-affected area of 160×160 km domain for wind speeds 10-15 ms^{-1}, displayed in [km^2] and percentage [%] of the domain. The average values displayed are unweighted averages and do not account for the number of occurrences in each direction, but are simply the mean of the 12 points along the dashed line representing the 2% deficit wake-line.

6.2.3 Wake recovery

One of the significant differences found between EWP and FIT in the ideal simulation by Volker et al. (2015) was the recovery of the velocity behind the wind farm in question. The recovery profile at hub height for the first 6-7 km behind the wind farm when using EWP was approximately linear, while FIT displayed an exponential profile with a faster initial recovery (see Figure 5 in (Volker et al. 2015, p. 3723)). Data in their study was not filtered for stability, and a largely neutral atmosphere was assumed.

A study is conducted to inspect the velocity recovery profile's dependence on wind farm parameterization and on atmospheric stability, and to examine the behaviour of overlapping wakes commonly observed in wind farm clusters. For this, data for winds between 250-270° with speeds 5-10 ms^{-1} are studied, with the wind speed along a 260° line passing through Sandbank and DanTysk used to represent the winds upstream and downstream of the wind farms. This wake-line is marked in Figure 6.10, and the data is taken from the nearest grid points, which are also marked on the map. The wind speed along the wake-line is plotted below the map (blue line), and the free stream velocity, defined as the wind speed two grid points (roughly 4 km) upstream of Sandbank, is plotted (solid line) along with a dashed line representing 98 % recovery. The velocity in the wake of Sandbank is verified using SCADA data for DanTysk turbines, which is illustrated by a star in the plots. It should be noted that the choice to bin data according to the grid cell containing FINO3 can result in large discrepancies between the FIT and EWP binned data. The difference in SCADA wind speed for EWP-stable and FIT-stable in Figure 6.10 is a result of this. A more detailed study of this SCADA data can be found in Chapter 7.

By examining the wind speed plots in Figure 6.10, the WRF wind speed at the western edge of DanTysk generally shows good agreement with the SCADA measurements. When examining the velocity decrease over Sandbank, stable conditions result in a greater reduction than unstable conditions. The recovery behind Sandbank is very similar when comparing the two different stability classes. The difference between EWP and FIT is very clear, however. For EWP, the velocity immediately after Sandbank increases slightly and quickly flattens, barely recovering further before encountering DanTysk. In the wake of Sandbank, the FIT wind speed displays a sharp increase for the entire distance between the two wind farms. The velocity reduction over DanTysk shows the same tendencies as over Sandbank. For unstable conditions, the velocity after DanTysk has decreased to roughly the same velocity as after Sandbank, which is unexpected. The scenario we would expect is displayed under stable conditions, where the velocity has only partially recovered before encountering DanTysk, decreasing further while passing the turbines in DanTysk. The reduction in wind speed over the individual wind farms is largely determined by the turbine type, and number of turbines in operation. The shape of both farms and their turbine types are quite similar, but it has not been inspected which turbines were operating for the data used in this analysis. The recovery profile in the wake of DanTysk shows a great disparity between FIT and EWP. The recovery for EWP is close to linear, especially in the stable case, while the FIT recovery shows a more exponential profile, recovering more quickly in the immediate wake. As there are no met masts in the wake of DanTysk, it cannot be determined which parameterization scheme portrays the wake recovery more accurately. However, the results are in agreement with research made by Volker et al. (2015) described in the beginning of this section, where measurements from two met masts agreed better with recovery simulated with EWP. However, the wake lengths in Figure 6.10 are also noticeably longer for FIT than for EWP, which is inconsistent with their

findings but in agreement with most subsequent literature and the previous analyses in this report. In Figure 6.11, the recovery behind DanTysk is examined in closer detail.

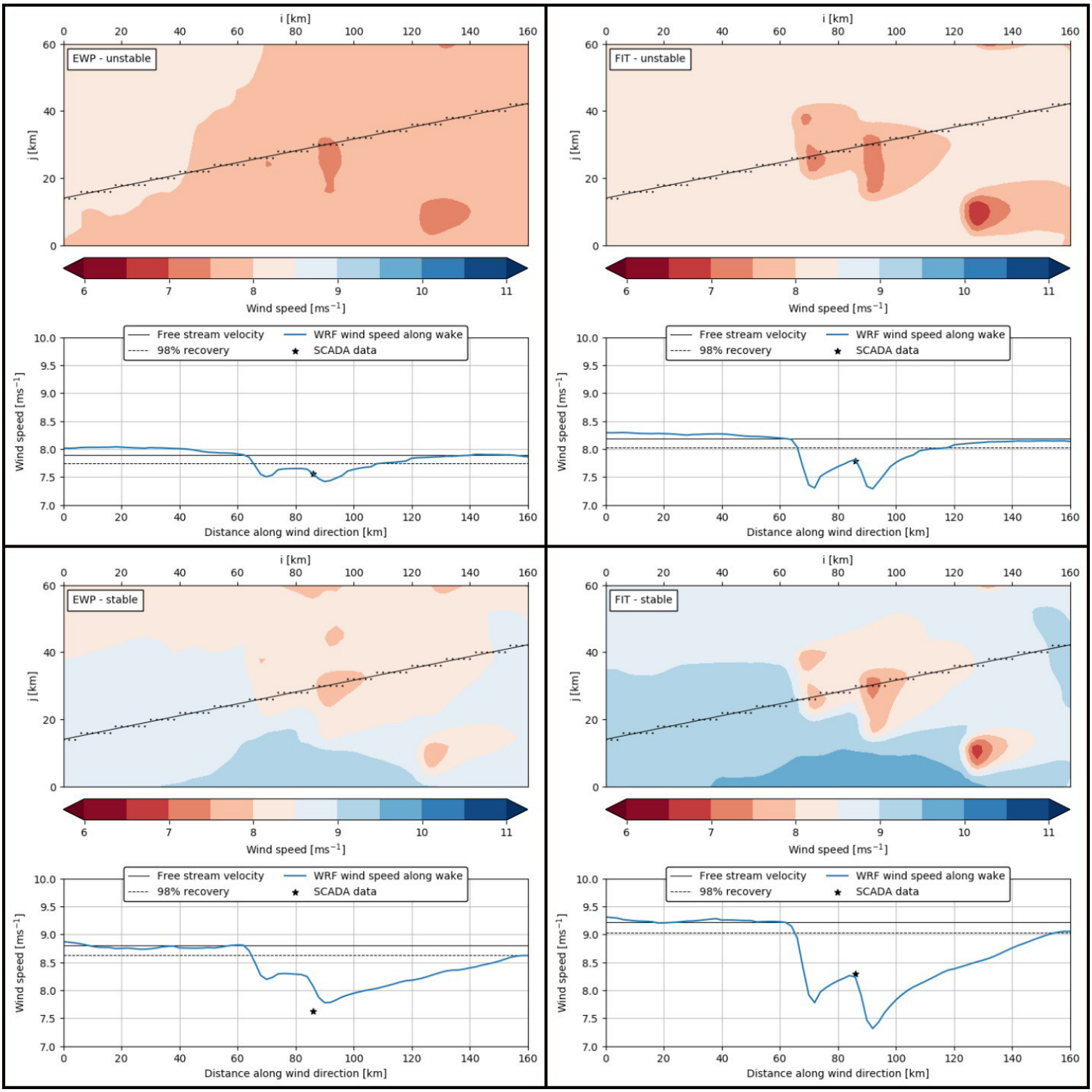

Figure 6.10: Hub-height velocity recovery under stable and unstable conditions for EWP and FIT using data from directions 250-270°and with velocities 5-10 ms^{-1}.

The hub height velocity recovery profile in the wake of DanTysk has been expressed as an exponential function with the form $y = a \cdot \exp(bx) + c$, and the expression is displayed in the plots. Comparing EWP simulations to FIT simulations, both stability cases show lower exponential coefficients b for EWP than their FIT counterparts, approaching a linear expression. The wake length is considerably shorter for unstable conditions, with 98% recovery after roughly 15 km and 20 km for EWP and FIT respectively, while both parameterizations result in wake lengths of roughly 65 km for stable conditions. This suggests that the overlapping of wakes has little influence on the wake length under unstable conditions, but impacts the wake greatly under stable conditions.

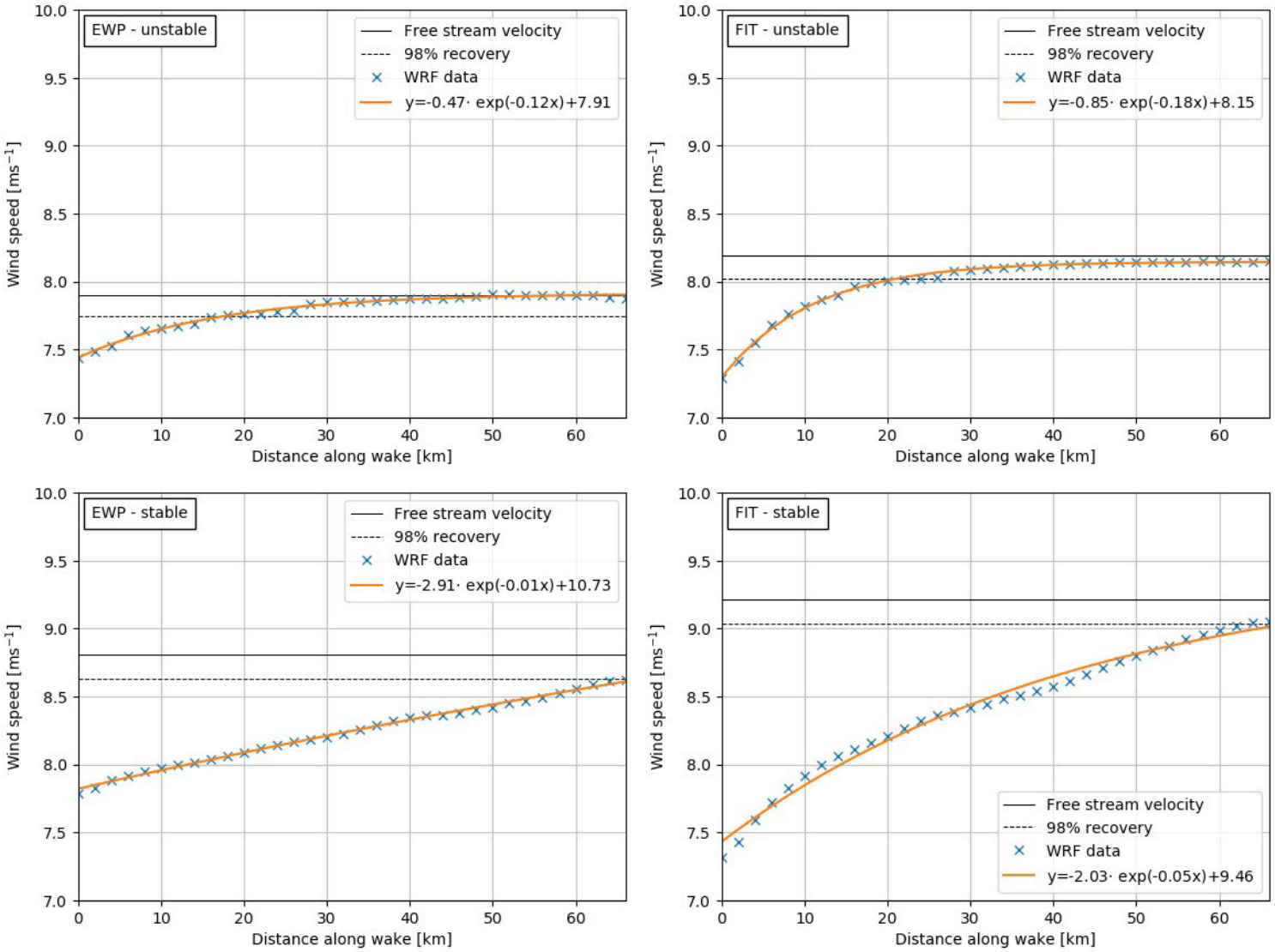

Figure 6.11: Hub-height velocity recovery profile in the wake of DanTysk, where 0 km on the x-axis corresponds to the trailing edge of DanTysk.

On the topic of wake interaction, with Figure 6.10 in mind we can speculate how the wake recovery profile of each individual farm may look without any influence from the other farm, and whether the superposition of these individual wakes would result in a velocity profile similar to those seen in the plots where both wind farms are present. This information would be very valuable in the

study of wakes, perhaps making it possible to use simple methods to predict combined wind farm wake effects inside wind farm clusters. The subject of wake superposition is not dealt with in this report but is a field of study that would be beneficial for future investigation.

6.3 TKE field

One of the fundamental differences between the EWP and Fitch schemes is in the treatment of TKE, where Fitch treats wind turbines as a source of TKE, and the TKE in EWP is generated solely by shear production. As a result, the TKE increase when using the Fitch scheme is much greater than when using EWP. In Figure 2.7, we saw Volker's comparison of the TKE field for EWP and FIT behind a wind farm for an ideal simulation using a wind speed of $10\,\mathrm{ms}^{-1}$, and found that the maximum TKE difference occurred inside the rotor area for FIT, while the maximum TKE increase in EWP, which was much smaller in magnitude, occurred downstream of the wind farm above hub height. EWP also displayed a decrease in TKE below the rotor area which continued downstream. The TKE difference found in Fitch et al. (2012, Figure 2d, p. 3023) displays similar behaviour to the FIT simulation by Volker, also showing that a TKE decrease near the surface evolves further downstream than the distance plotted by Volker.

A study of the TKE field is made by assessing the TKE difference shown in Figure 6.13. As stable conditions are expected to cause the longest wakes, the TKE under stable conditions is examined first. The data used for this analysis is for winds from 265-275° where the wind speed is between 9-$11\,\mathrm{ms}^{-1}$. The TKE difference for the filtered data points is time-averaged and plotted for EWP and for FIT. The cross-section shown is along the line displayed in Figure 6.12, which passes through both Sandbank and DanTysk. It should be noted that TKE advection is turned off in Langor's simulation, but turned on in Volker's and Fitch's simulations. Fitch et al. (2012) states that the representation of TKE is improved when horizontal TKE advection is included in the model. With TKE advection turned on, there is a connection between adjacent grid cells and TKE is transported horizontally to neighbouring cells. With TKE advection turned off, TKE develops inside grid cells but is not transported downwind. The TKE advection only affects the horizontal transportation, thus the TKE is distributed vertically in all cases.

The TKE for EWP is of much lower magnitude than FIT, as is expected due to the extra TKE source term included in the Fitch scheme. FIT shows a maximum TKE increase almost 7 times that of EWP. The maximum TKE difference for both schemes is located above the hub height of each wind farm, which is not in agreement with the profiles found by Volker and Fitch. There is a development of TKE downwind of the farms for both schemes of comparable magnitudes. Both schemes show a similar decrease in TKE below hub height which extends downstream, and the maximum decrease in TKE for FIT is 1.7 times that of EWP.

To better be able to compare the TKE profile found in Volker et al. (2015) and Fitch et al. (2012) where there was no filtering of stability, the TKE profile is plotted for the same wind speeds and directions as before; however it is not filtered for stability, and a predominantly unstable atmosphere can be assumed. The results are shown in Figure 6.14. Here, the disparity between the maximum TKE increase displayed by both schemes is lower than the stable case, and it is roughly 4 times greater for FIT. The TKE increase does not extend very far beyond the wind farms, and the downstream TKE exhibits rapid changes with distance. However, the TKE decrease below the

wind farms shows similar behaviour downstream as found by Volker and Fitch, extending above hub height. The maximum TKE decrease for FIT is roughly twice as great as for EWP. The shorter extension of the TKE increase above hub height is possibly due to the higher rate of mixing under the largely unstable atmosphere, but the reason for the behaviour of the turbulence further downstream is unknown.

There are considerable differences between the TKE profiles from Langor's simulations and the TKE profiles from Fitch's and Volker's simulations. The reason for these differences are unclear; differences in the simulations include the model's TKE advection physics and whether the simulations are real or ideal in WRF. Langor's real simulations include the developing of weather over time, and the downstream wake behaviour can be expected to be more dynamic than in idealized simulations, where a number of parameters are kept constant. The TKE profiles in this study are made by averaging over a number of discontinuous data points, while Volker and Fitch used continuous data. It is possible that this discontinuity influences the resulting TKE profile. The study of the TKE field in the wake of wind farms using WRF is sparse in current literature and is a topic for future research. In this study, it has not been possible to run simulations including TKE advection and has therefore not been explored further.

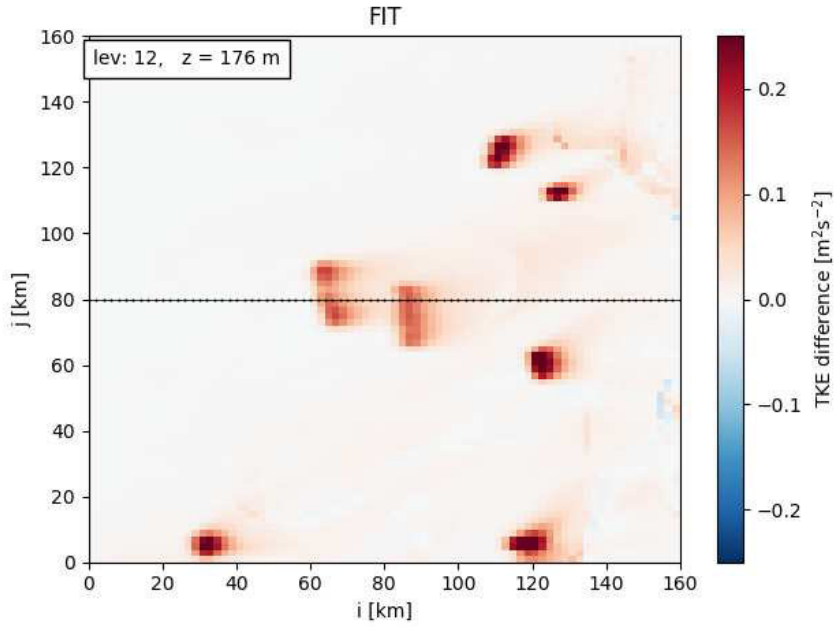

Figure 6.12: TKE difference between FIT and NWF at 176 m for wind directions 265-275°, wind speeds 9-11 ms^{-1} and stable conditions. The domain shown is the 160 × 160 km area centred around Sandbank and DanTysk studied earlier in this report.

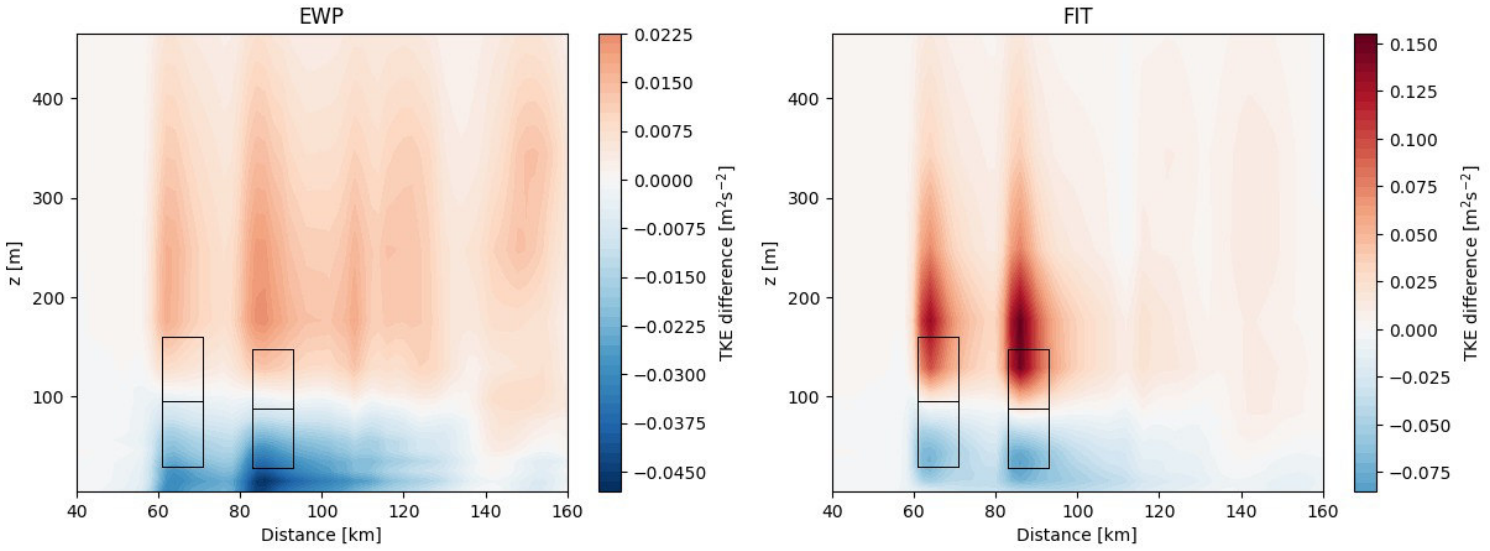

Figure 6.13: TKE difference profile for EWP and FIT for wind directions 265-275°, wind speeds 9-11 ms^{-1} and stable conditions.

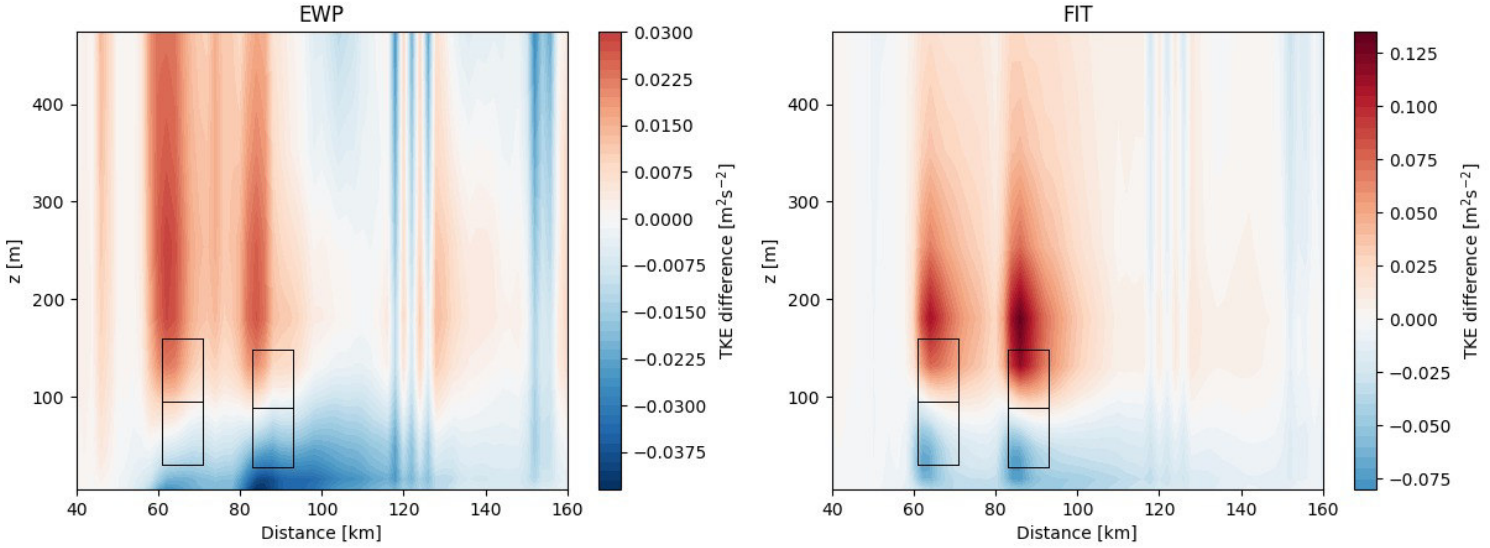

Figure 6.14: TKE difference profile for EWP and FIT for wind directions 265-275°and wind speeds 9-11 ms^{-1}, unfiltered for stability.

CHAPTER 7

In situ analysis

In this chapter, an analysis of SCADA data from DanTysk is carried out in order to determine the consequence of the wake effects between wind farms. The analysis is conducted using data ensuring that the northernmost turbines of DanTysk are affected by the wake of Sandbank, and the southernmost are outside the wake and are unaffected by the presence of Sandbank. The wake effect is expressed by the change in the capacity factor of the turbines, calculated from the SCADA wind speed and the power curve, and the dependence on stability is assessed.

7.1 Effect of Sandbank wake on DanTysk capacity factor

7.1.1 Low-velocity wakes using SCADA data

Data has been filtered using the same method as in Chapter 6.2, with bins for wind direction, wind speed and stability applied to the output data from WRF simulations. Wind directions 250-270° are chosen to ensure that DanTysk is partially affected by Sandbank's wake, and wind speeds 5-10 ms^{-1} are used as it has been determined as the range of wind speeds where the wake effect is strongest, as well as the fact that a reduction in wind speeds above rated speed may not affect power production. Figure 7.1 shows the wake effect for the chosen range of wind speeds and directions. Turbines on the western edge of DanTysk are examined to assess the wake effects, with the four northernmost used as the wake-affected sample group and the four southernmost as the control sample group unaffected by the wake. The turbines evaluated are shown in Figure 7.2 and Table 7.1.

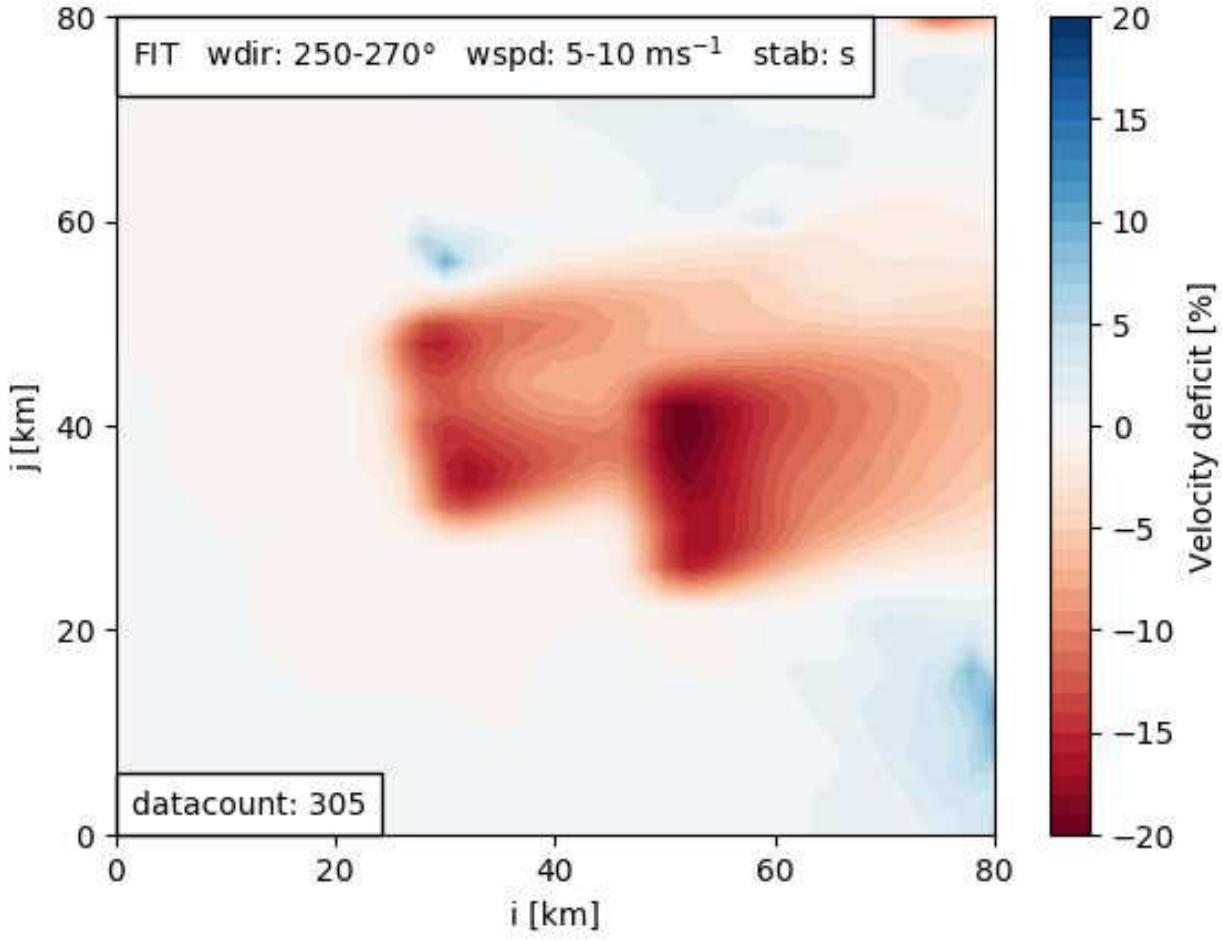

Figure 7.1: Velocity deficits at hub height, with the northern part of DanTysk affected by the wake from Sandbank.

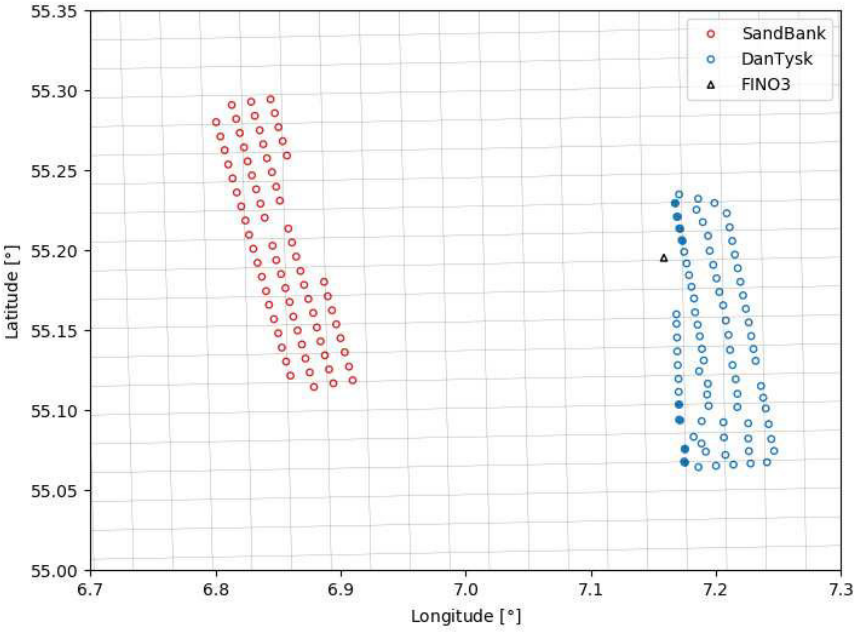

Figure 7.2: Location of the 8 DanTysk turbines (filled circles) chosen to assess wake effects from Sandbank.

Table 7.1: DanTysk turbines to be evaluated.

Control turbines (south)	**Wake-affected turbines (north)**
GDT001	GDT018
GDT002	GDT019
GDT004	GDT020
GDT005	GDT021

The capacity factor for four scenarios will be investigated: EWP-stable, EWP-unstable, FIT-stable and FIT-unstable. As an example, the data filtering process for FIT-stable will be explained here. WRF data from the FIT simulation is filtered for wind directions 250-270°, wind speeds 5-10 ms^{-1} and stable conditions. Each instance where the data fulfills these criteria has a timestamp associated, and these timestamps are used to filter SCADA data. A validation is needed to show that the nacelle direction in SCADA matches the wind direction in WRF for these timestamps. The SCADA data for the nacelle direction of each DanTysk wind turbine is found, and for each timestep a wind farm average is found by averaging over all 80 turbines. Figure 7.3 shows the average nacelle direction of the wind farm. The majority of the cases are within or close to the range of 250-270° as expected, thus the data is validated with regard to wind direction. The wind speed is not validated, as the SCADA wind speed recorded by each turbine is not expected to match velocity used in the WRF data binning process, and stability conditions are not validated either. The corresponding figures validating wind direction for FIT-unstable, EWP-unstable and EWP-stable can be seen in Appendix C.1.

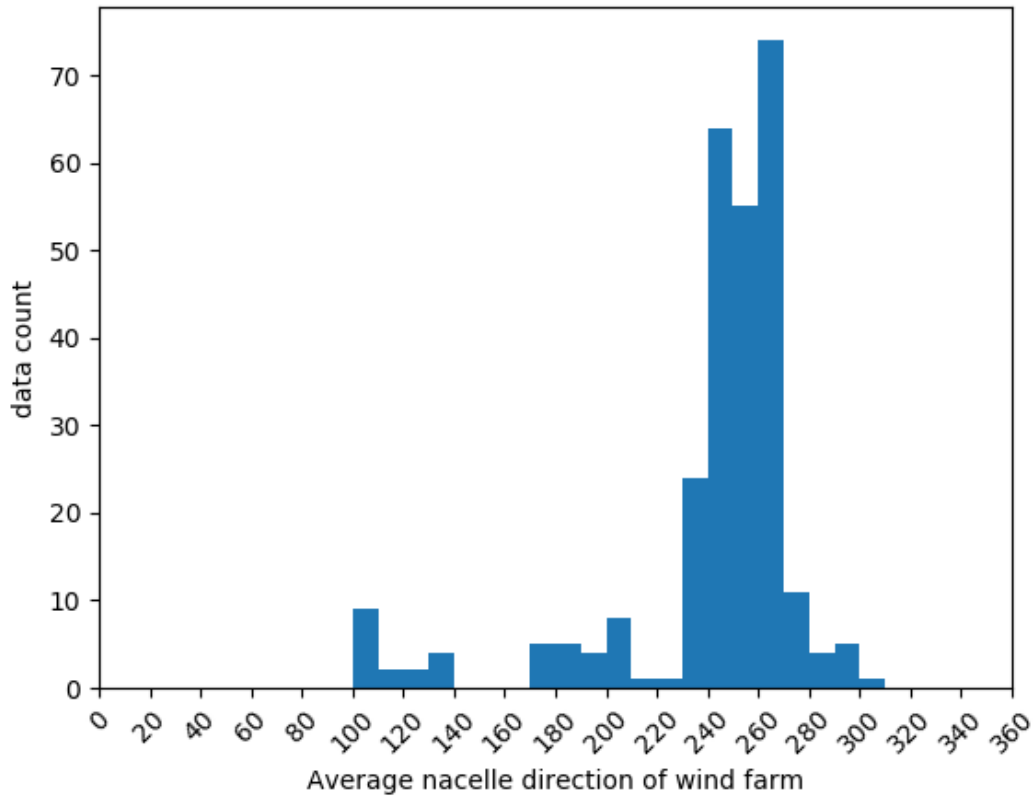

Figure 7.3: Average nacelle direction [°] of wind farm for FIT-stable filtered data.

The capacity factor for the 8 turbines are calculated using Equation 7.1:

$$\text{Capacity Factor} = \frac{\text{Actual Energy Generated [MWh]}}{\text{Capacity [MW]} \times \text{Time [hr]}}\,, \tag{7.1}$$

where the numerator is calculated using the power curve and the SCADA wind speed for the relevant timestamps, and the denominator is the maximum possible energy that can be generated over these timestamps. For each of the 4 scenarios, an average capacity factor $\overline{CF}$ is calculated for the control turbines and for the wake-affected turbines. The same is done calculating the average SCADA wind speed $\overline{U}$, and the results are displayed in Figure 7.4, where the wake effect is quantified by the percentage-wise decrease in wind speed ΔU and the decrease in capacity factor ΔCF between the two turbine groups. Figures illustrating the wind speed for all DanTysk turbines can be seen in Appendix C.2.

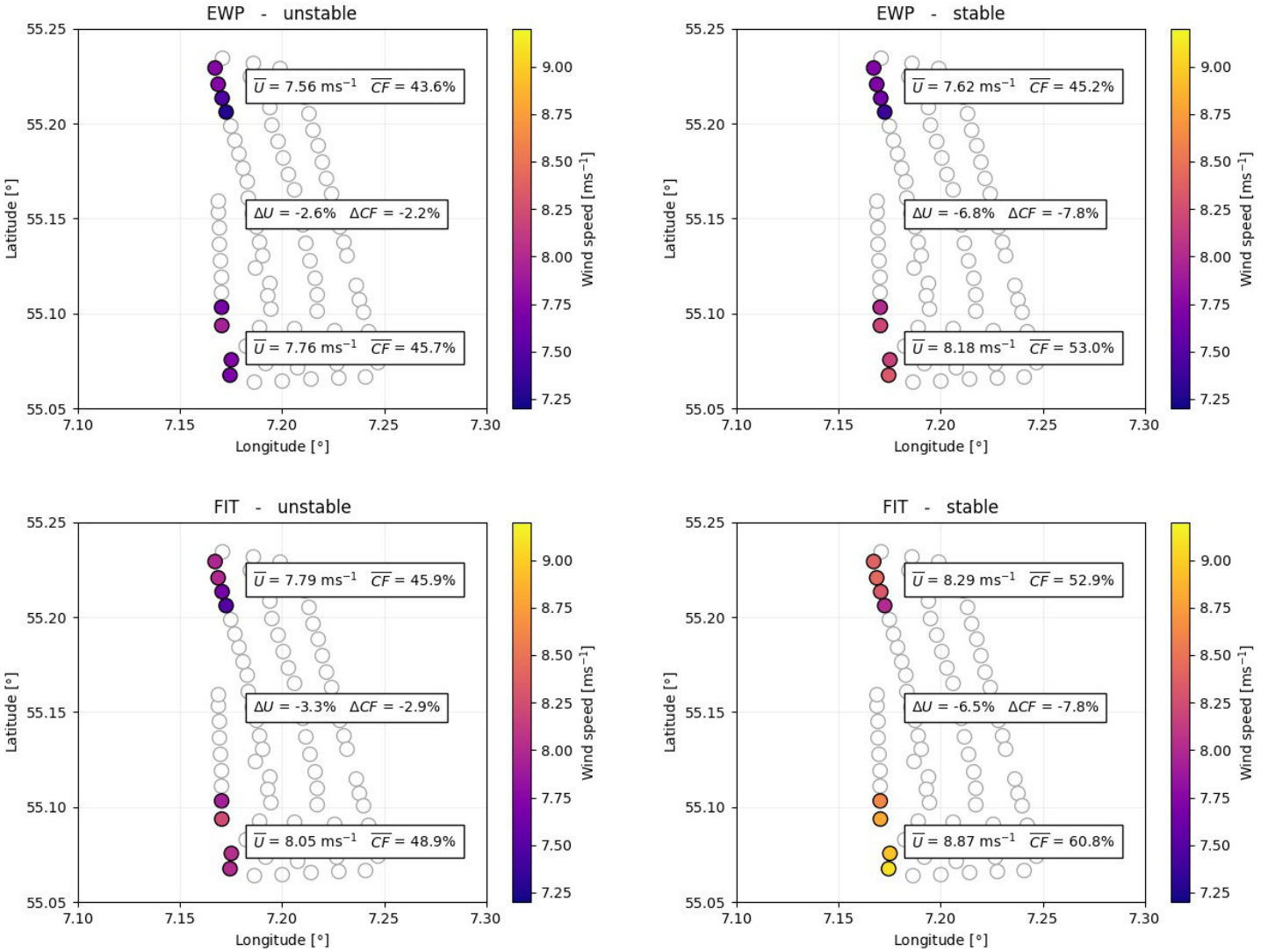

Figure 7.4: Average wind speeds and capacity factors for wake-affected turbines and control turbines.

For all four cases, the in situ data shows that the wake-affected group of turbines experiences a lower average wind speed and has a lower average capacity factor than the control group of turbines experiencing the freestream velocity. This confirms that a wind farm lying in the wake of another experiences reduced wind speeds and a reduction in power production when those winds are below rated wind speed. It is also apparent that the reductions in wind speed and capacity factor are much greater under stable conditions than unstable conditions. There is a reduction in capacity factor of around 2-3% under unstable conditions, while the reduction in capacity factor under stable conditions is almost 8%. This is in agreement with findings in Pryor et al. (2020), where reductions in capacity factors of onshore turbines were found to be greater at night, where stable conditions prevailed.

The difference between the EWP and FIT cases displayed in Figure 7.4 arises from the data filtering process, where small differences in the binned data lead to more high winds included in the FIT

cases and fewer low winds. As velocity deficits are generally higher for FIT than EWP, a larger portion of winds above $10\,\mathrm{ms}^{-1}$ in the NWF simulation will drop below that speed in the FIT simulation, where they will become included in the 5-$10\,\mathrm{ms}^{-1}$ bin range, increasing the average wind speed and thereby also increasing the capacity factor for the given cases. This difference would be reduced by choosing to filter data according to an undisturbed upwind grid cell, where the difference in wind speed between EWP and FIT would be negligible.

7.1.2 Annual capacity factor

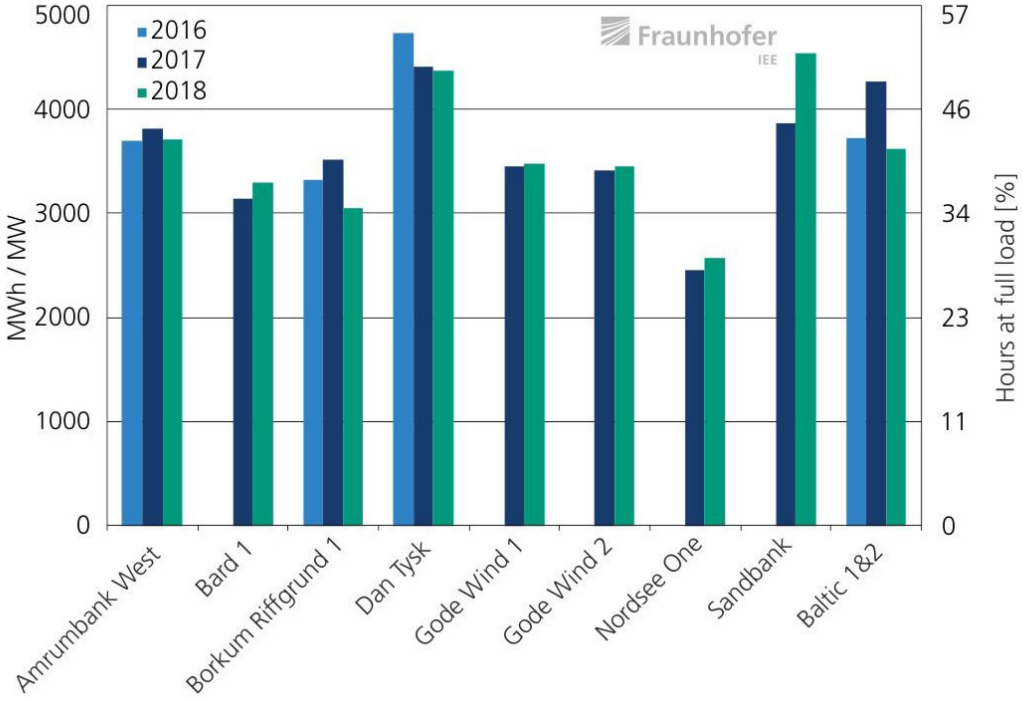

Figure 7.5: Full load hours and capacity factor of offshore wind farms wind farms for 2016-2018. Source: Fraunhofer IEE, http://windmonitor.iee.fraunhofer.de/windmonitor_de/4_Offshore/5_betriebsergebnisse/1_Volllaststunden/

Using data for the annual electricity generation from offshore wind power plants, Fraunhofer Institute for Energy Economics and Energy System Technology (Fraunhofer IEE) compares the performance of a number of offshore wind farms. The performance is quantified by full load hours and capacity factor of the wind farms for the years 2016, 2017 and 2018. The results are shown in Figure 7.5, where the performance of DanTysk is seen to decrease considerably from 2016 to 2017, and the capacity factor of Sandbank in 2018, its first fully operational year, is higher than the capacity factor of DanTysk the same year. Being situated to the west of DanTysk, Sandbank is expected to leave DanTysk experiencing lower velocities in the case of westerly winds, which is the prevailing wind direction. As Sandbank began operation in January 2017, there is a high possibility that the presence of Sandbank reduced the performance of DanTysk, underlining the importance of understanding wakes from offshore wind farm clusters.

CHAPTER 8

Conclusion

In this study, the behaviour of wakes in large offshore wind farm clusters was investigated using the wind farm parameterizations Fitch and EWP in the mesoscale model WRF. The purpose of this was to quantify the wake effects through analyzing long-term mesoscale modelling data and SCADA data, and to quantify the differences between the two wind farm parameterizations.

In order to characterize wakes seen behind offshore wind farms, wind velocity deficits at hub height and turbulence kinetic energy were examined as functions of wind speed, wind direction, and atmospheric stability. The analysis was based on year-long simulations of the 2018 climate over a domain in the North Sea.

The 2018 climatology of the region was studied using met mast measurements from offshore research platform FINO3, showing westerly winds to be the strongest and most frequent. A largely unstable atmosphere was identified, with a higher frequency of stable conditions occurring in the spring and summer months. The 2018 climate was put into perspective by comparing it to the long-term climate from 2010-2018, showing evidence that the wind speed was reduced by the presence of the Sandbank and DanTysk wind farms.

The WRF simulations were validated against FINO3 measurements, showing that WRF on average slightly overpredicted wind speeds. Winds between 5-20 ms^{-1} were estimated to a high degree of accuracy, but winds that were measured to be below and above this range were overestimated and underestimated in WRF, respectively. The directional distribution of wind speeds matched well between FINO3 and WRF, and the atmospheric stability simulated in WRF was marginally more stable than observed.

Mean wind speed deficits at hub height were used for analysis, and velocity deficits in excess of 2% were defined as the wake. Velocity deficits were found to be highest at 10 ms^{-1}, corresponding with the peak in the thrust force curve, and the highest percentage-wise deficits were in the 5-10 ms^{-1} range of wind speeds. FIT simulations consistently exhibited greater deficits than EWP simulations, with the greatest disparity between the two schemes occurring in the wind speed range 5-10 ms^{-1}. The higher velocity deficits exhibited when using the Fitch scheme agrees with findings in most prior studies.

Quantifying wakes using characteristics such as wake length and wake-affected area, the average length and size of wakes simulated with FIT were roughly 50% greater than when simulated with EWP. Additionally, the intensity of wakes using FIT was higher inside and near the wind farms. It is important to note that the nonuniform distribution of wind farms inside clusters means wakes are highly dependent on wind direction, and it can be difficult to correctly estimate the length of certain wakes.

The effect of atmospheric stability on the wake characteristics was quantified, showing a 50% increase in wake length for stable conditions compared to unstable conditions. Furthermore, the wake-affected area under stable conditions was almost 2 times larger than for unstable. Due to the low number of samples in the neutral stability class, wakes under these conditions had an increased level of uncertainty; however, the results indicated that wakes of similar magnitudes to those under stable conditions could occur.

Studying the recovery of the hub height velocity, the recovery profiles when using the two schemes differed greatly, with FIT displaying an exponential recovery and EWP displaying a near-linear recovery. This behaviour was also seen in Volker et al. (2015), which included the first comparison of the EWP and Fitch schemes.

An investigation of the TKE field in the wake of Sandbank and DanTysk for winds of 9-11 ms^{-1} yielded considerably different results than Fitch et al. (2012) and Volker et al. (2015), with an increase in TKE directly above the hub height of the wind farms and a decrease below for both EWP and FIT. Under stable conditions, the TKE increase continued further downstream for both parameterizations, but little downstream development was seen for the data unfiltered for stability. In agreement with Volker et al. (2015) however, the TKE increase was much greater for FIT than EWP due to the additional TKE source included in the Fitch scheme, with the FIT simulation showing a maximum TKE increase up to 7 times larger than seen for EWP.

Using SCADA data for the DanTysk wind speeds and the power curve for the SWT-3.6-120 turbine, the effect of wakes from Sandbank on DanTysk was quantified by the capacity factor of a number of DanTysk turbines. This was done for winds in the 5-10 ms^{-1} range, and the effects under stable and unstable conditions were assessed. Wakes under unstable conditions caused capacity factors to be reduced by 2-3%, while under stable conditions the reduction was almost 8%. This agrees with results from a study of an onshore wind farm cluster by Pryor et al. (2020).

This thesis has been a contribution to the OffshoreWake project and to the wider field of research on wakes from large offshore wind farm clusters, describing the wake behaviour in mesoscale simulations and quantifying differences between the two existing wind farm parameterizations. It serves as an important step forward in the understanding and application of the newest and most advanced wind farm parameterizations available in mesoscale modelling.

CHAPTER 9

Future work

The characteristics of wakes and the accuracy when estimating these in clusters of offshore wind farms is critical for power forecasting and when deciding on the location of new wind farms.

The analyses in this study can be expanded upon in a number of ways. The investigation of velocity recovery and the TKE profile could be extended to include all wind direction sectors for a more general description of the wake effect, and expanding the analyses to a larger area including more wind farms can further increase our understanding of wake behaviour in large offshore clusters of wind farms.

Further research is needed to definitively determine which wind farm parameterization performs with the highest fidelity. This is partly due to the small number of locations where measurements are available, and simulated data only at these locations can be compared with the observed data. Comparing WRF simulations to more wide-ranging measurement sources could help to determine whether the EWP or the Fitch scheme better represents observed wind speeds of wakes. Hasager et al. (2015) compared results from WRF simulations using the EWP scheme to satellite SAR images, Siedersleben et al. (2018) used aircraft measurements for comparison with WRF simulations using the Fitch scheme, and dual-Doppler radar or lidar measurements have been used in comparison with several wake models, as done by Gayle Nygaard and Newcombe (2018). Future studies could include these measurement methods for comparison with WRF simulations including both wind farm parameterizations.

As offshore wind farm clusters become more densely packed, the behaviour of multiple wind farm wakes overlapping and merging needs to be considered. This can be studied through mesoscale modelling with upwind farms removed, comparing the wake recovery to the scenario including the upwind farms. The spatial planning of new offshore wind farms could benefit greatly from being able to accurately predict this wake interaction. Due to the different recovery profiles exhibited by the EWP and Fitch schemes, the superposition of wakes in WRF would be highly dependent on the parameterization used, further increasing the need to establish the accuracy of both schemes.

In order to properly represent the influence of wind farms on the wind, the physics behind the simulations must be understood and carefully considered. The inclusion of TKE advection in future simulations could improve the performance of the simulations, and further research into

both schemes' treatment of TKE, the resulting turbulence, and its effect on wind velocity would be beneficial.

APPENDIX A

Climatology

A.1 Weibull distributions at FINO3

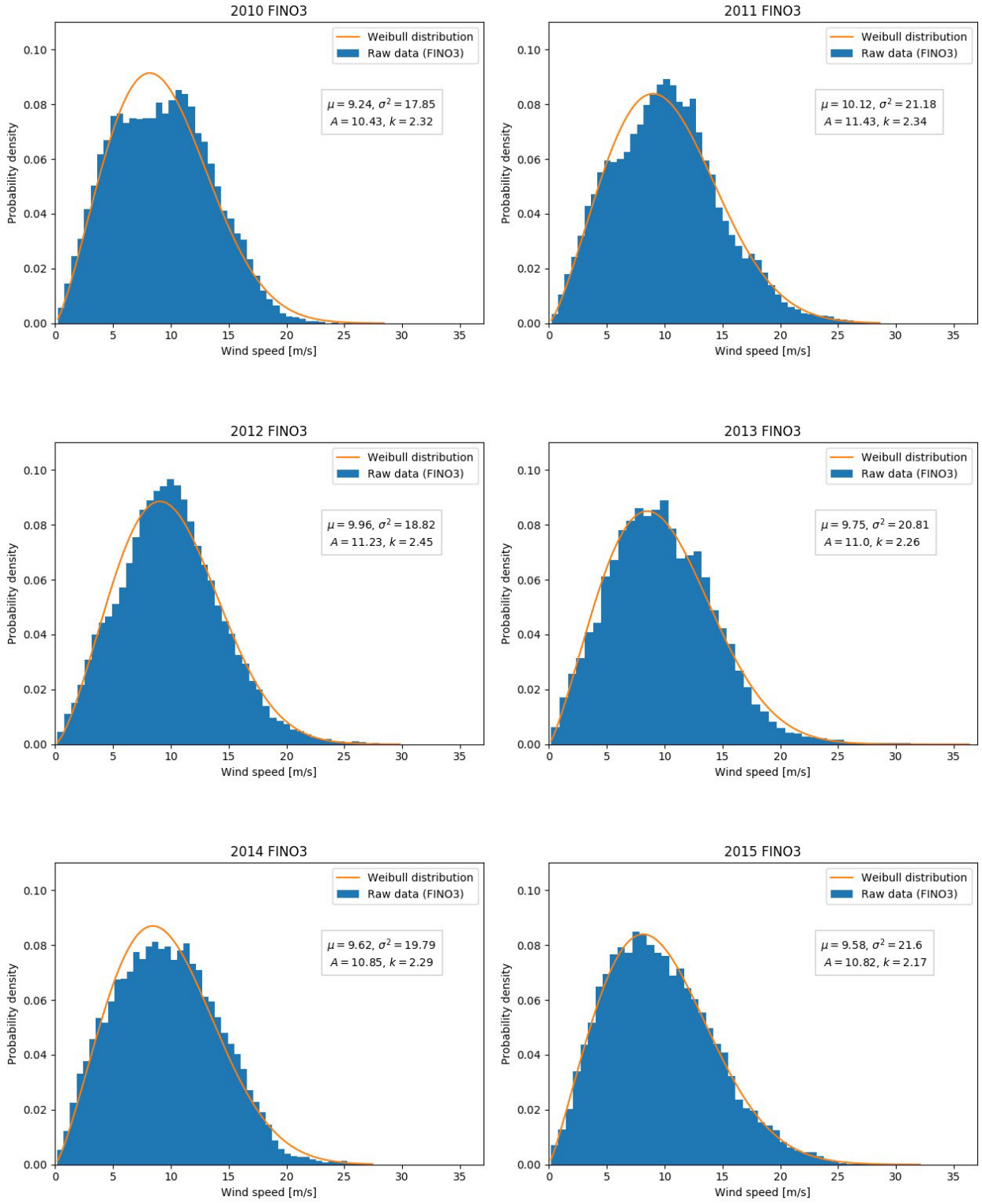

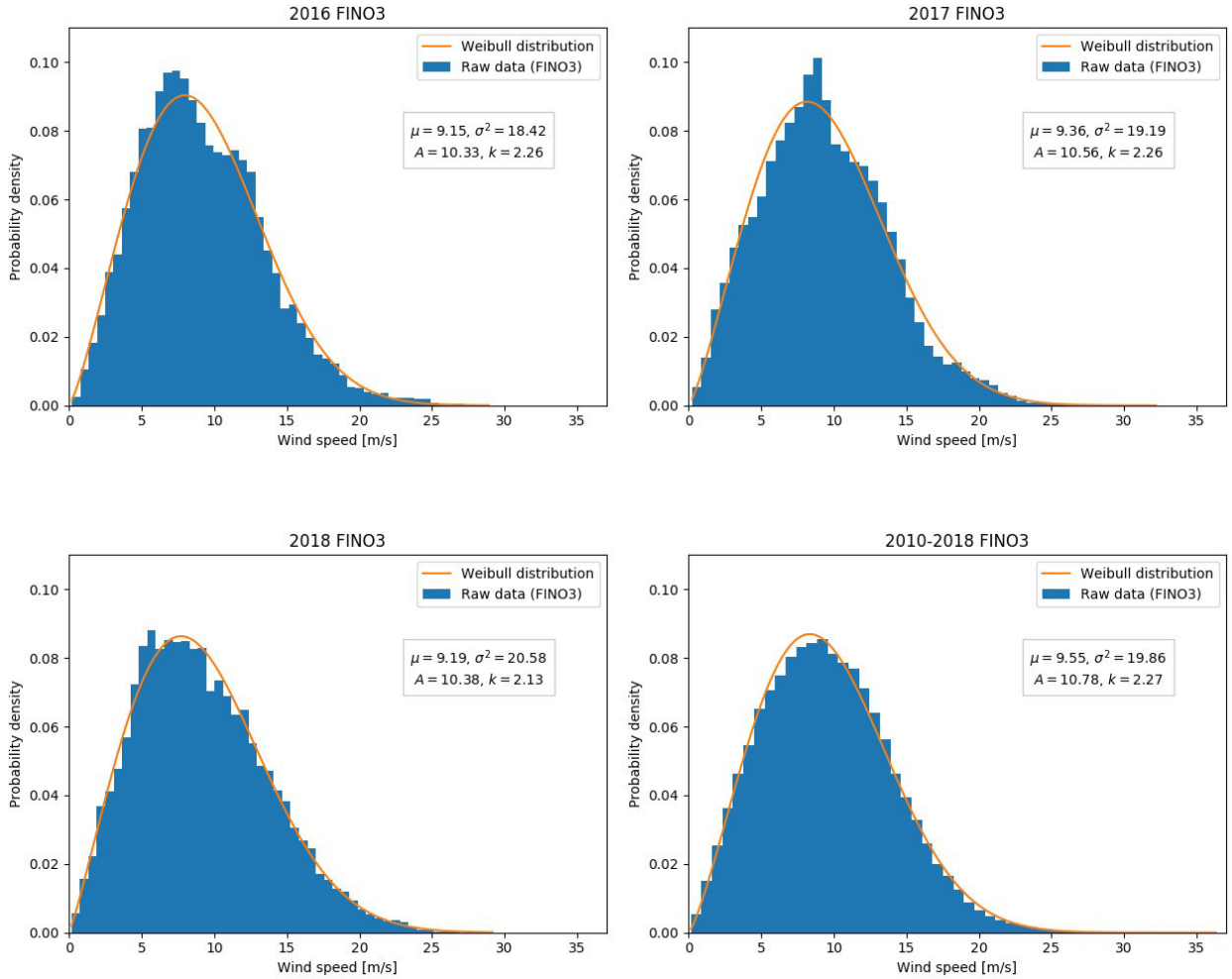

Figure A.1: Histograms and Weibull distributions of wind speeds observed at FINO3 for 2010-2018 and of period average. Values for the mean μ, variance σ^2, and Weibull scale parameter A are in [ms^{-1}].

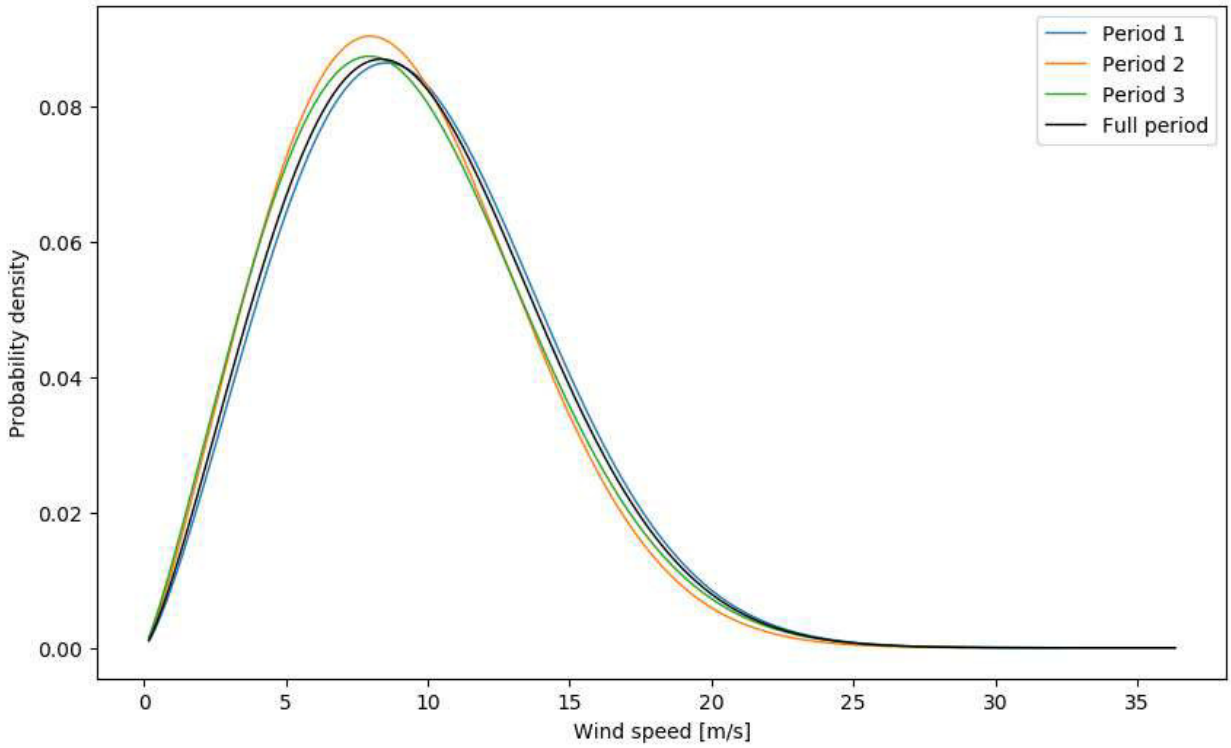

Figure A.2: Weibull distributions of wind speeds observed at FINO3 for periods.

A.2 Wind roses at FINO3

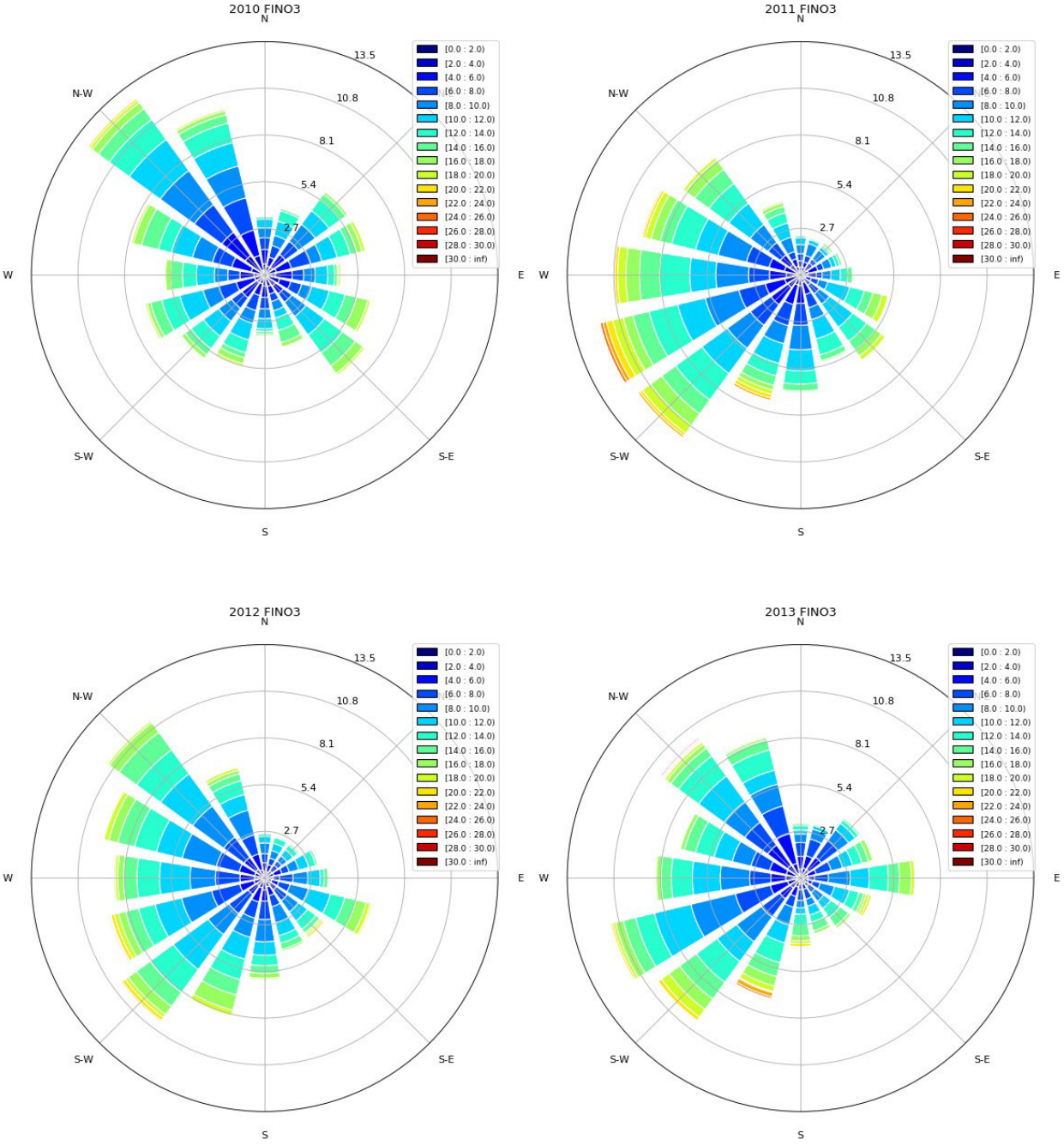

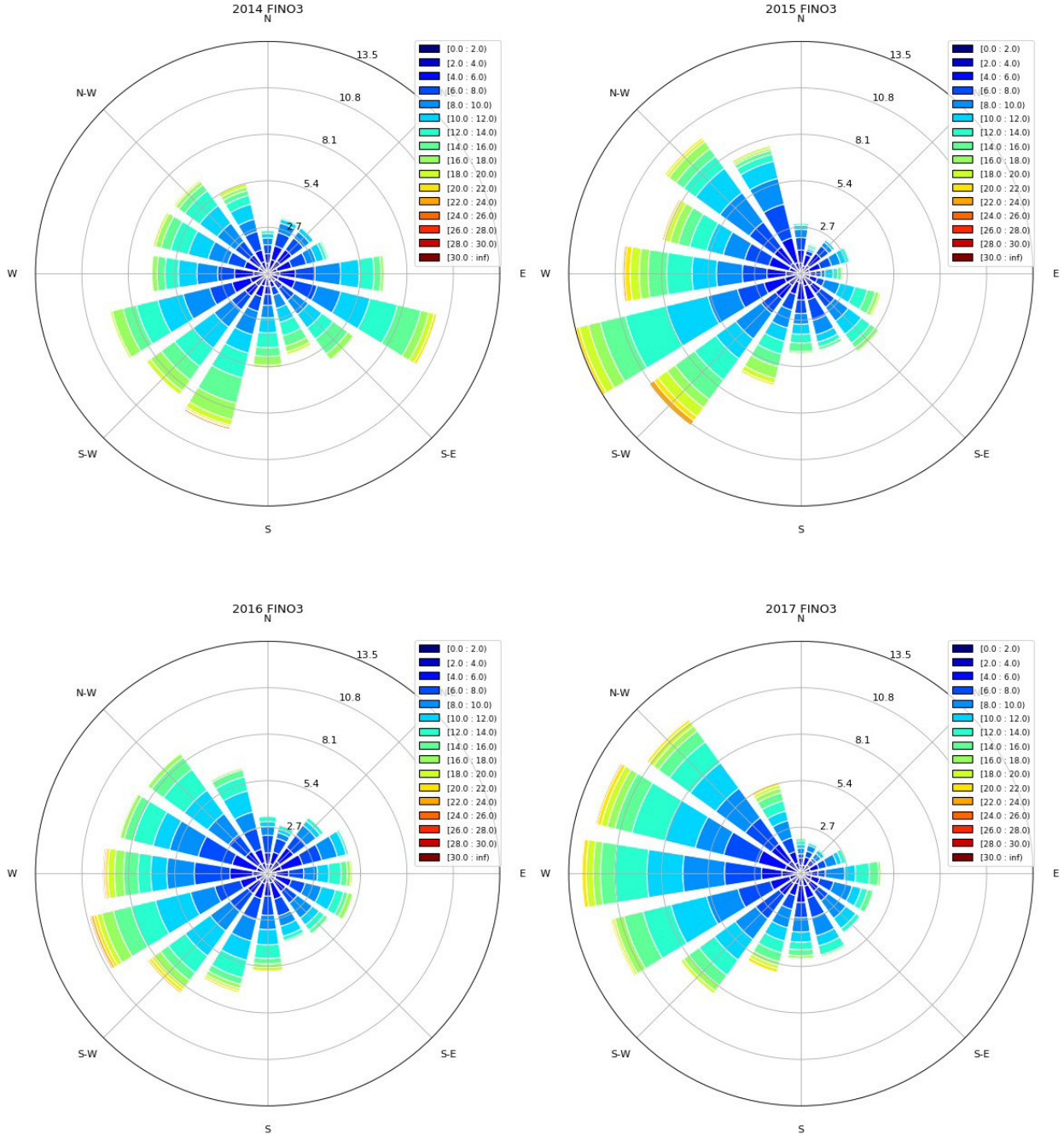
2014 FINO3
2015 FINO3
2016 FINO3
2017 FINO3
N
N-W
W
S-W
S
S-E
E
13.5
10.8
8.1
5.4
2.7
[0.0 : 2.0)
[2.0 : 4.0)
[4.0 : 6.0)
[6.0 : 8.0)
[8.0 : 10.0)
[10.0 : 12.0)
[12.0 : 14.0)
[14.0 : 16.0)
[16.0 : 18.0)
[18.0 : 20.0)
[20.0 : 22.0)
[22.0 : 24.0)
[24.0 : 26.0)
[26.0 : 28.0)
[28.0 : 30.0)
[30.0 : inf)

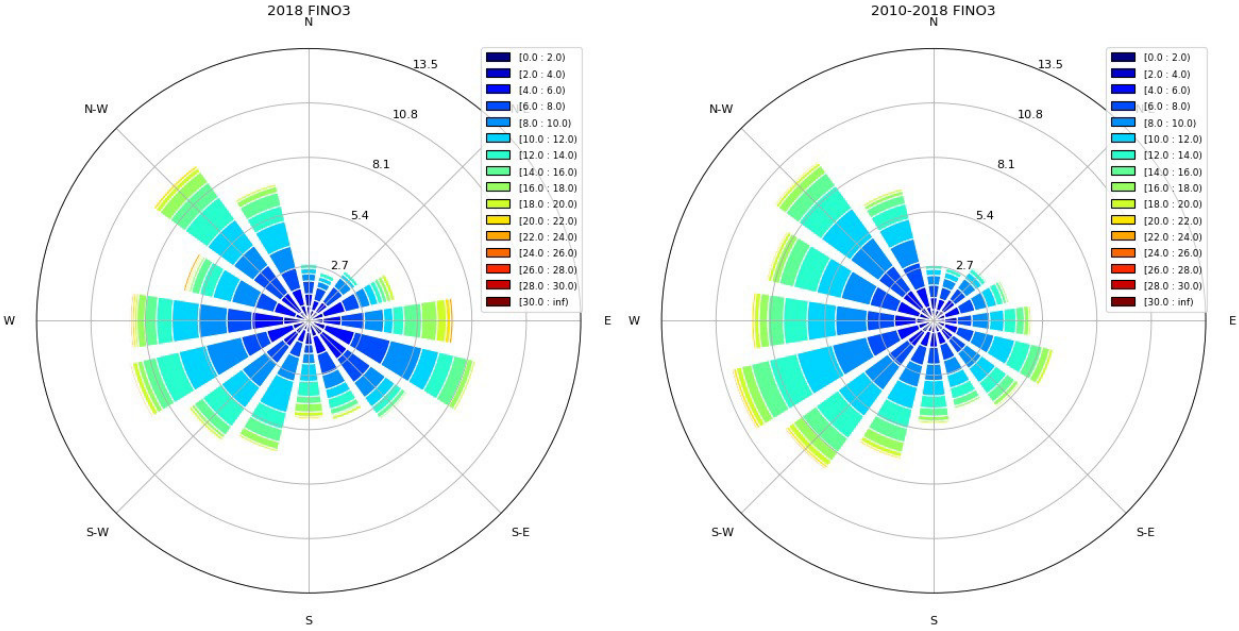

Figure A.3: Wind roses for observations at FINO3 for each year from 2010-2018 and for period average.

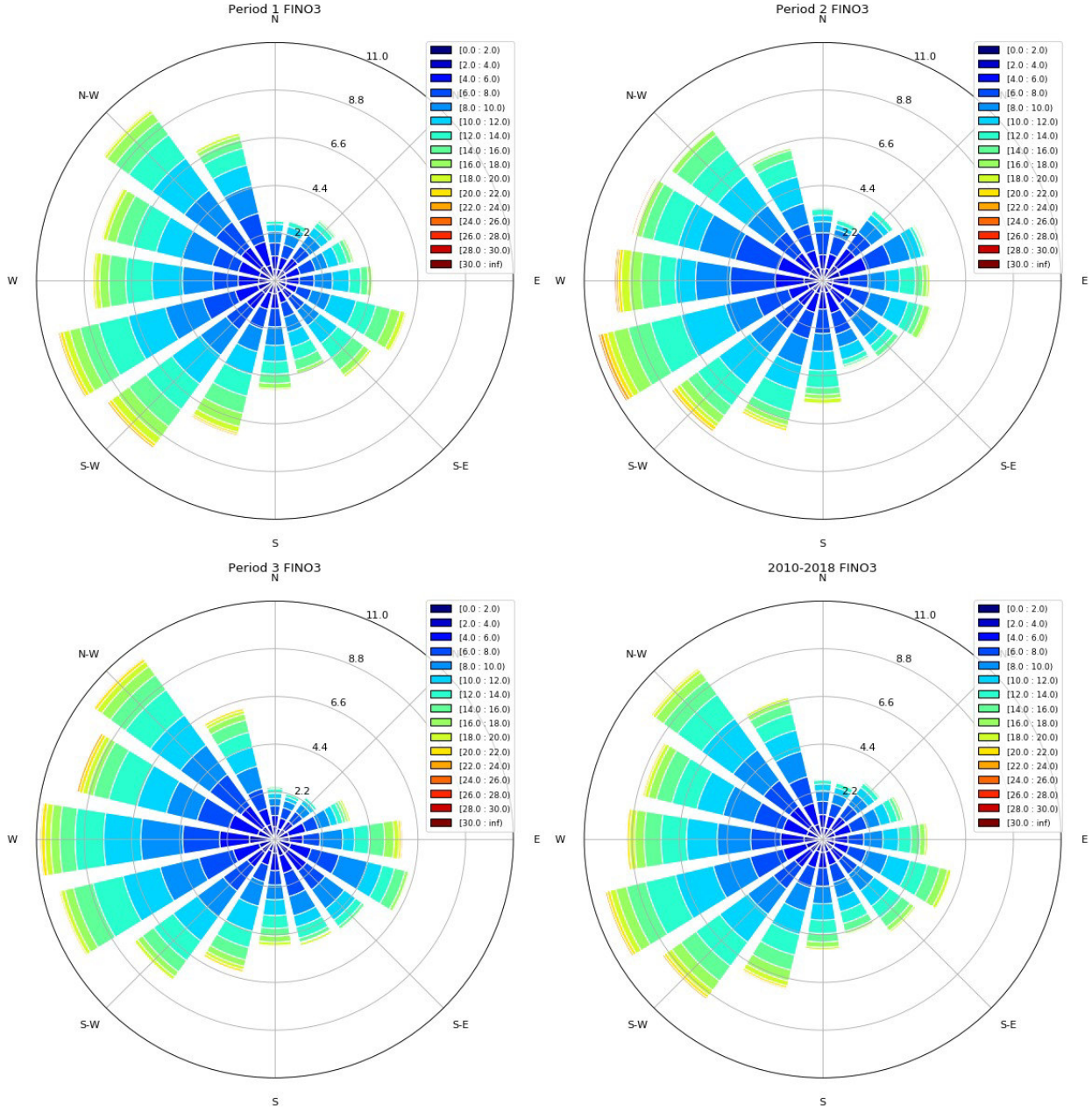

Figure A.4: Wind roses for observations at FINO3 for periods.

APPENDIX B

Wake effects

B.1 Hub height velocity deficit

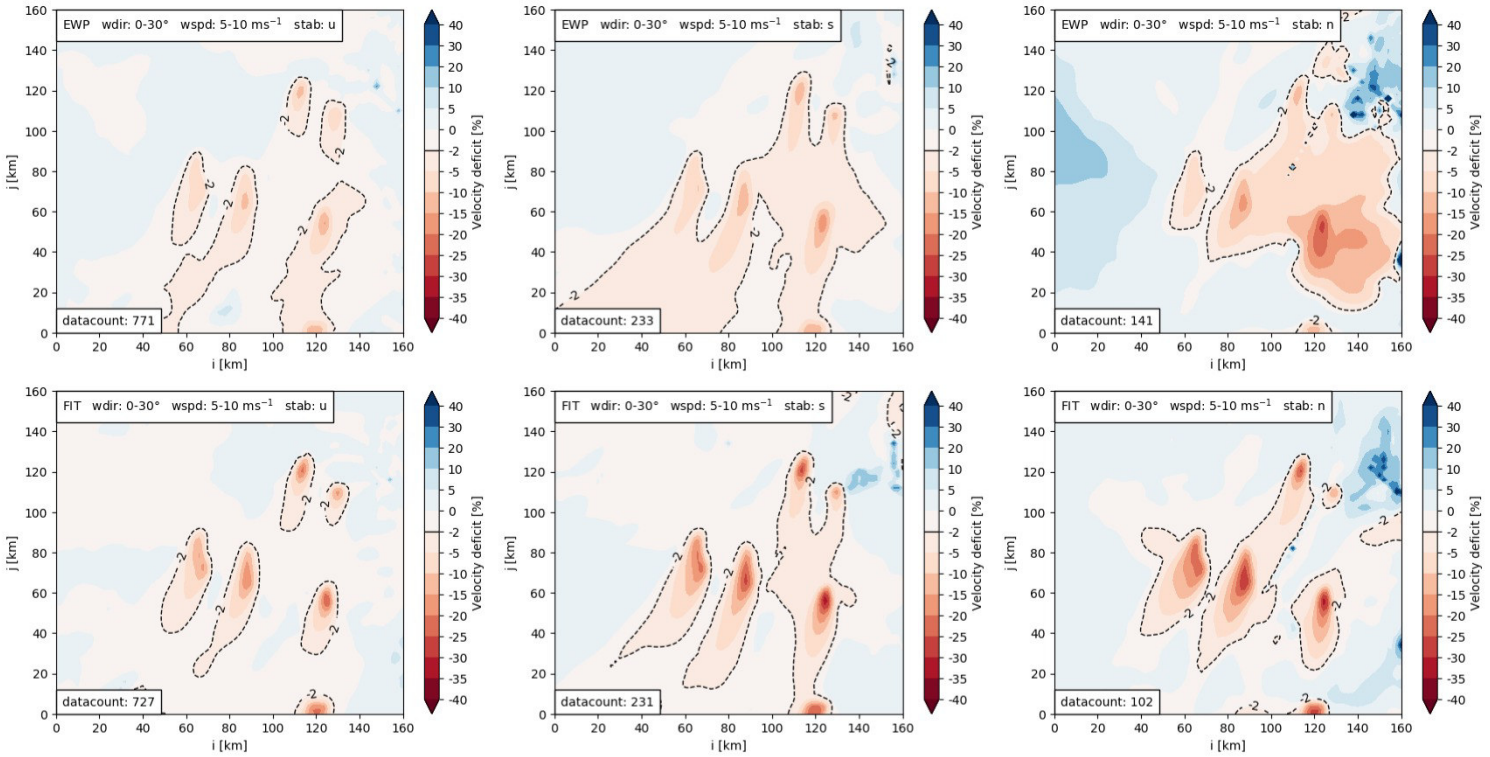

Figure B.1: Wind speed deficit at hub height for wind directions 0-30° and wind speeds 5-10 ms^{-1}.

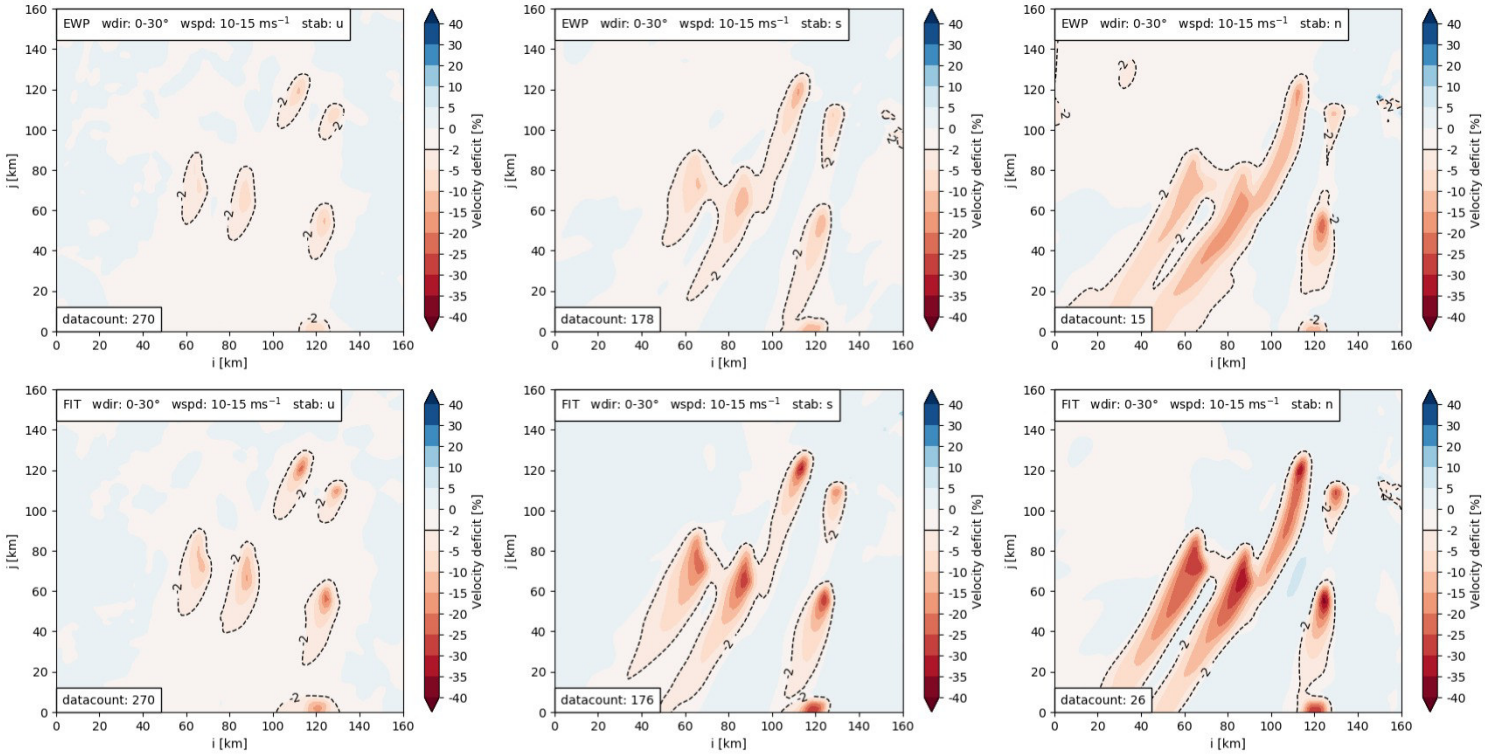

Figure B.2: Wind speed deficit at hub height for wind directions 0-30° and wind speeds 10-15 ms^{-1}.

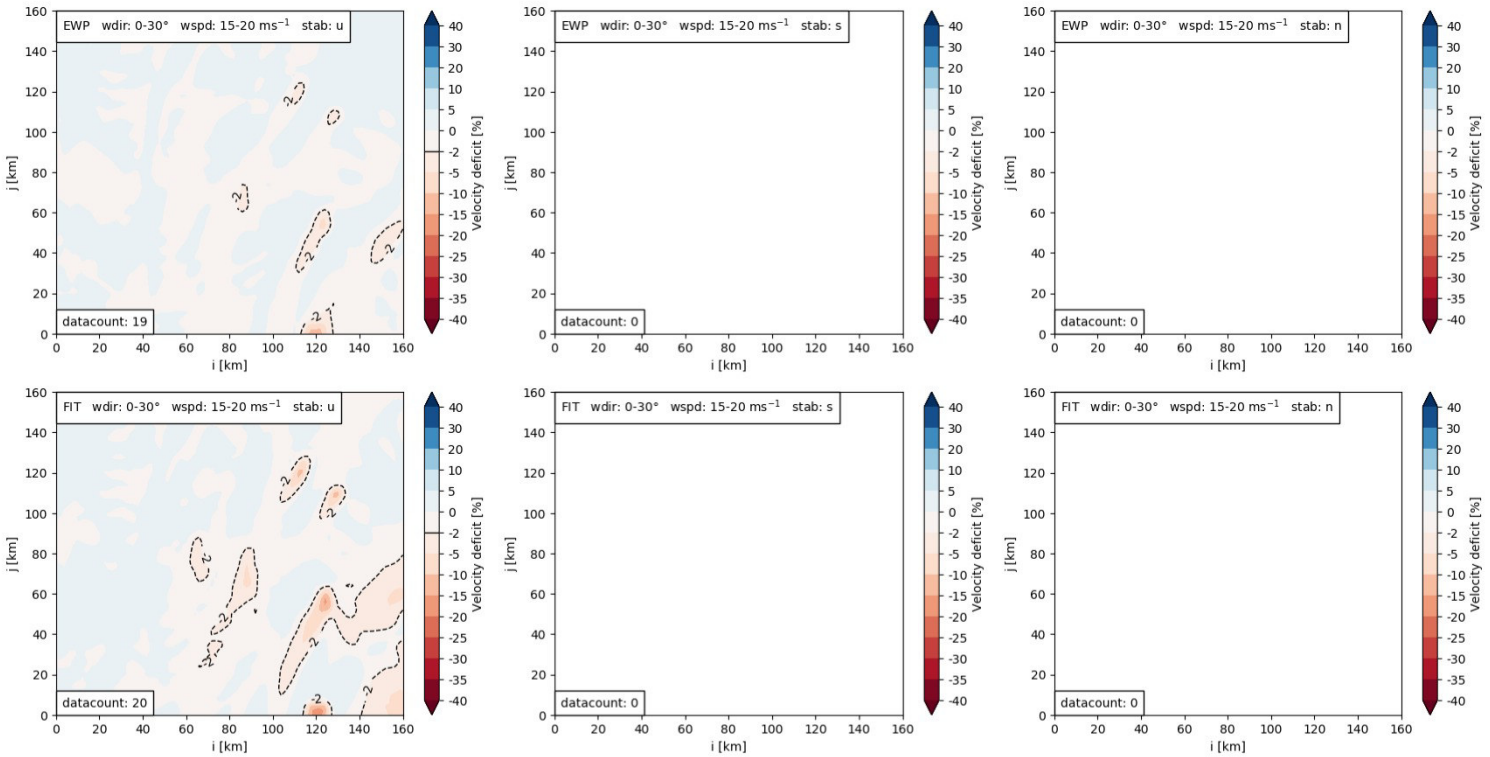

Figure B.3: Wind speed deficit at hub height for wind directions 0-30° and wind speeds 15-20 ms^{-1}.

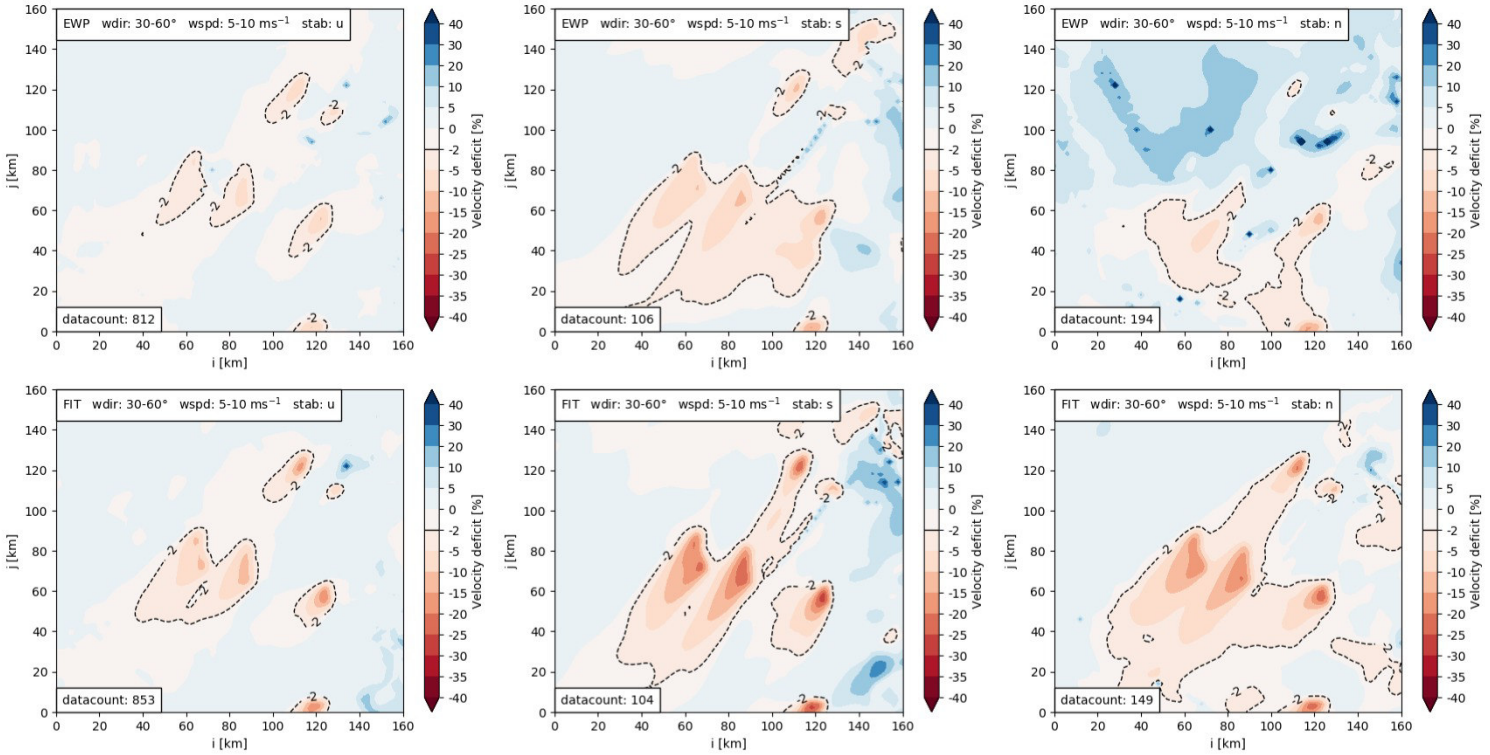

Figure B.4: Wind speed deficit at hub height for wind directions 30-60° and wind speeds 5-10 ms^{-1}.

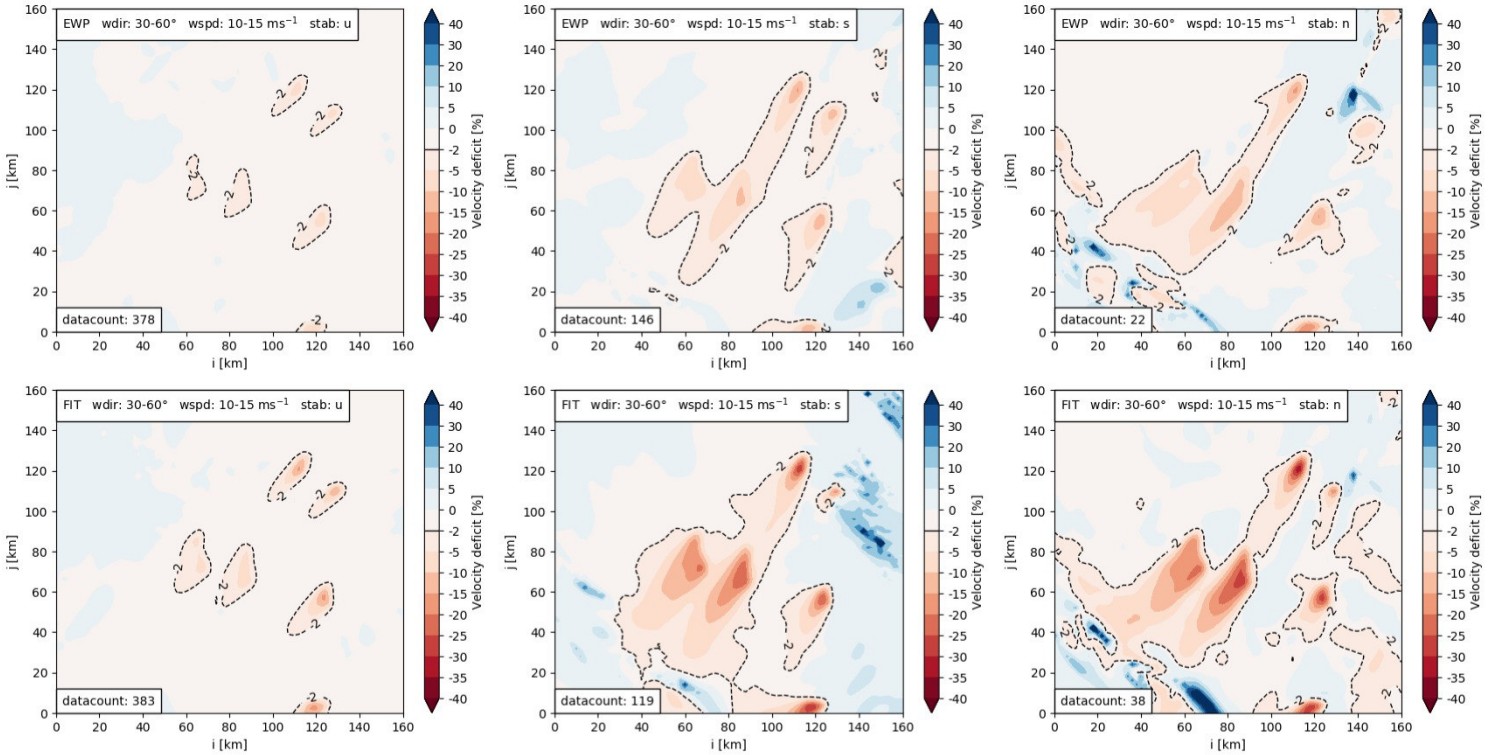

Figure B.5: Wind speed deficit at hub height for wind directions 30-60° and wind speeds 10-15 ms^{-1}.

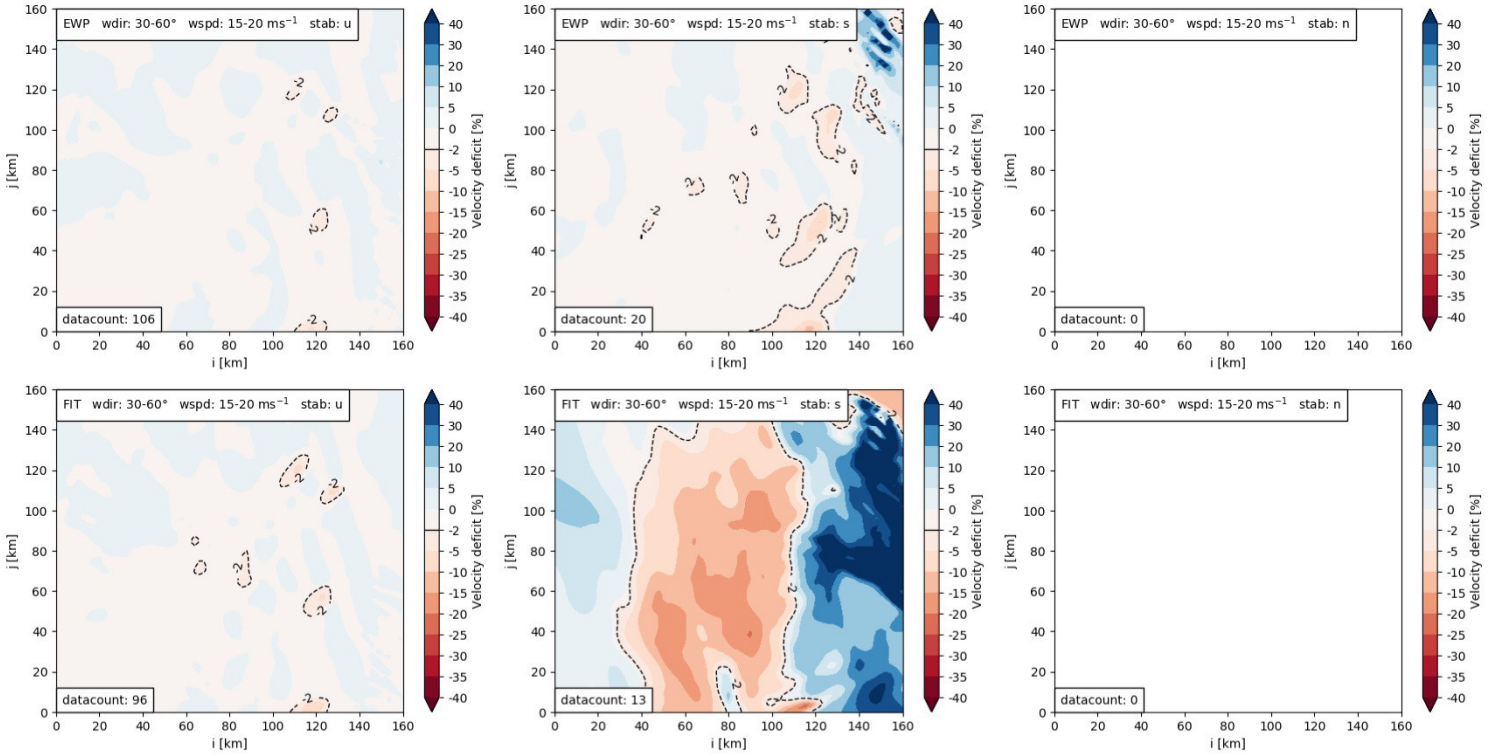

Figure B.6: Wind speed deficit at hub height for wind directions 30-60° and wind speeds 15-20 ms^{-1}.

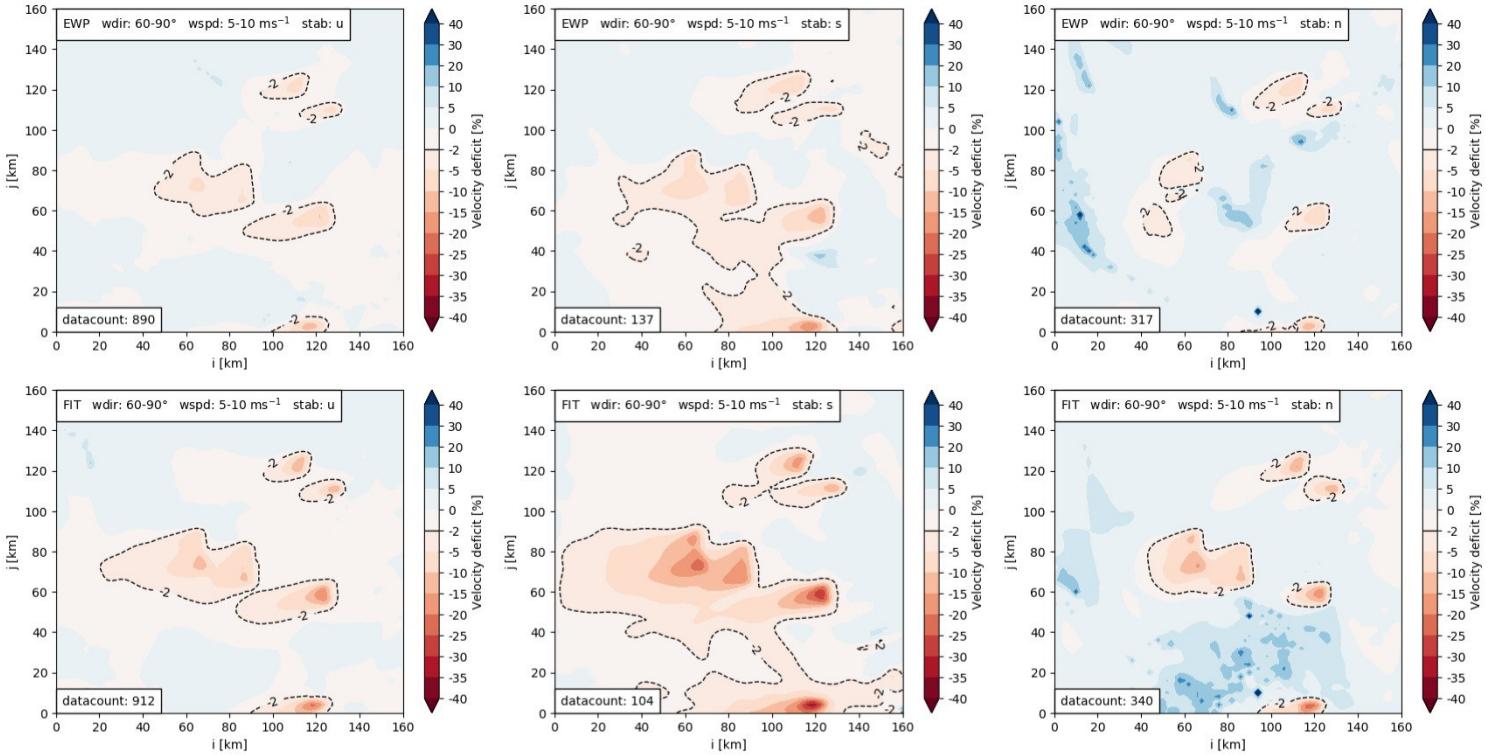

Figure B.7: Wind speed deficit at hub height for wind directions 60-90° and wind speeds 5-10 ms^{-1}.

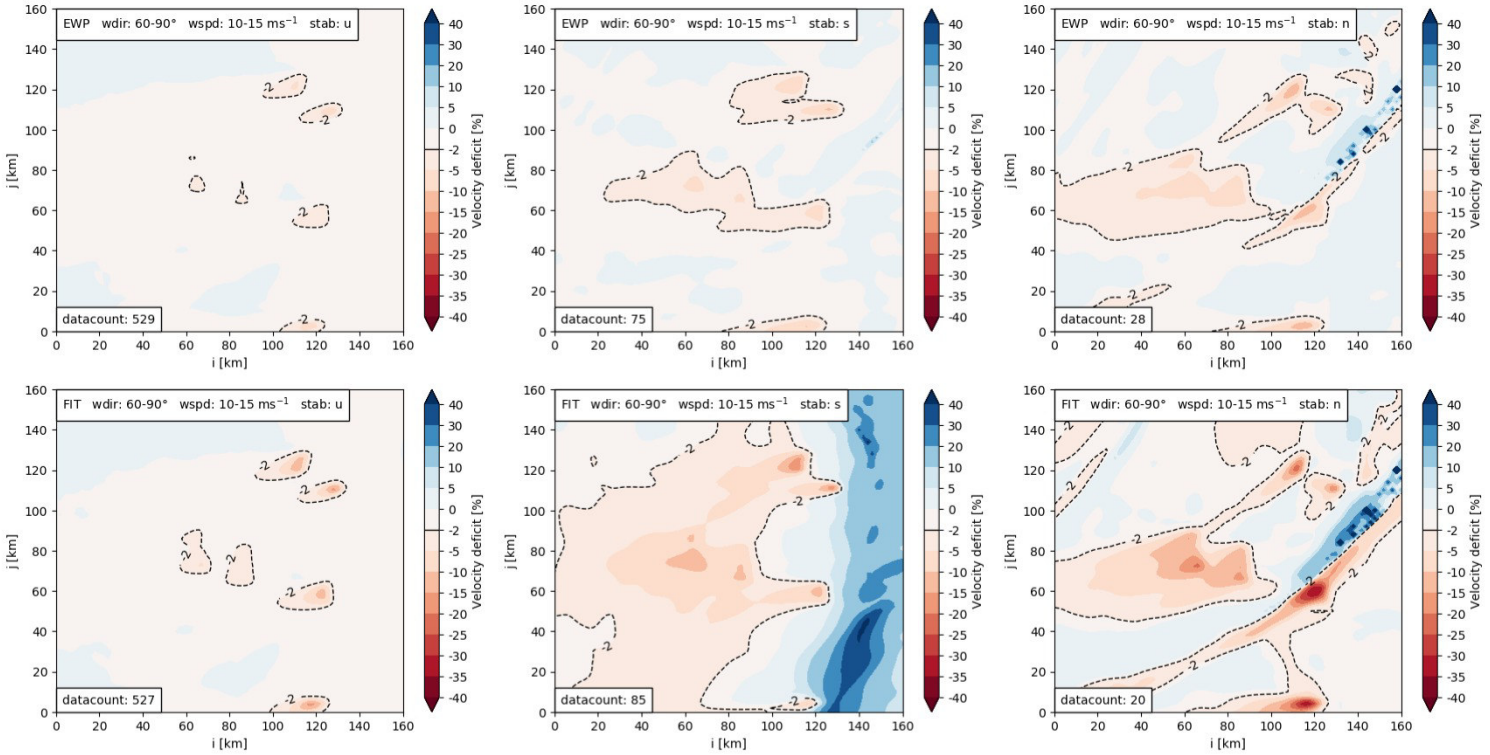

Figure B.8: Wind speed deficit at hub height for wind directions 60-90° and wind speeds 10-15 ms^{-1}.

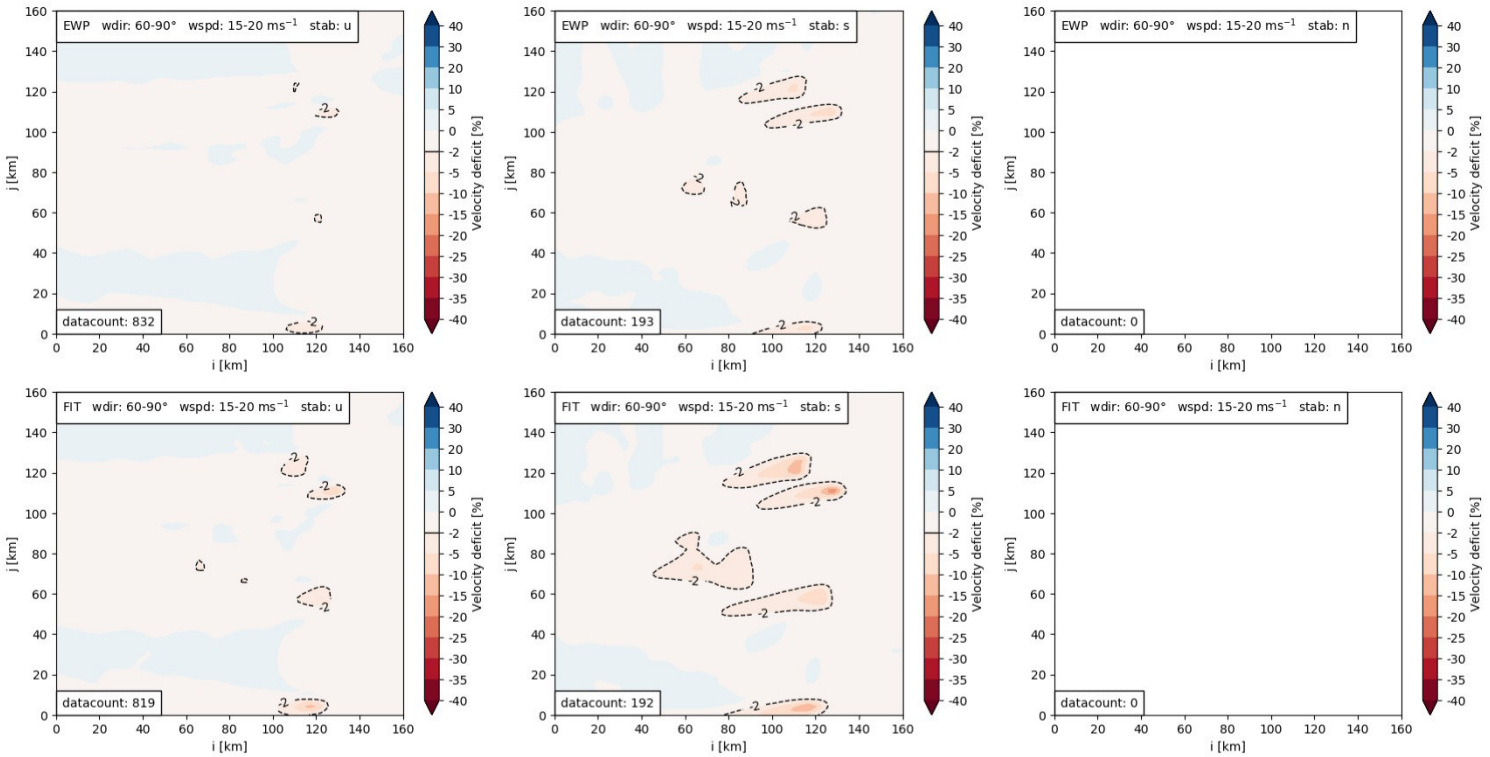

Figure B.9: Wind speed deficit at hub height for wind directions 60-90° and wind speeds 15-20 ms^{-1}.

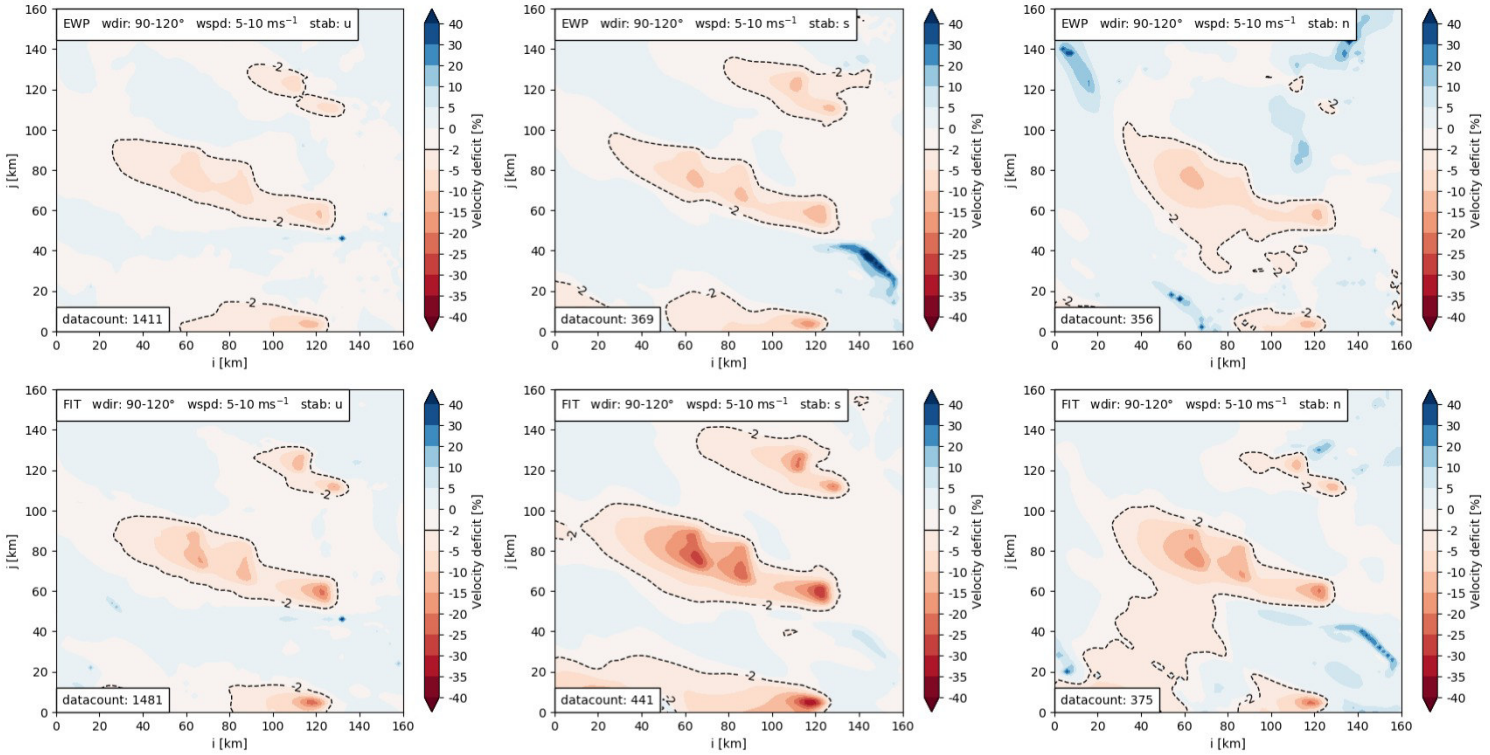

Figure B.10: Wind speed deficit at hub height for wind directions 90-120° and wind speeds 5-10 ms^{-1}.

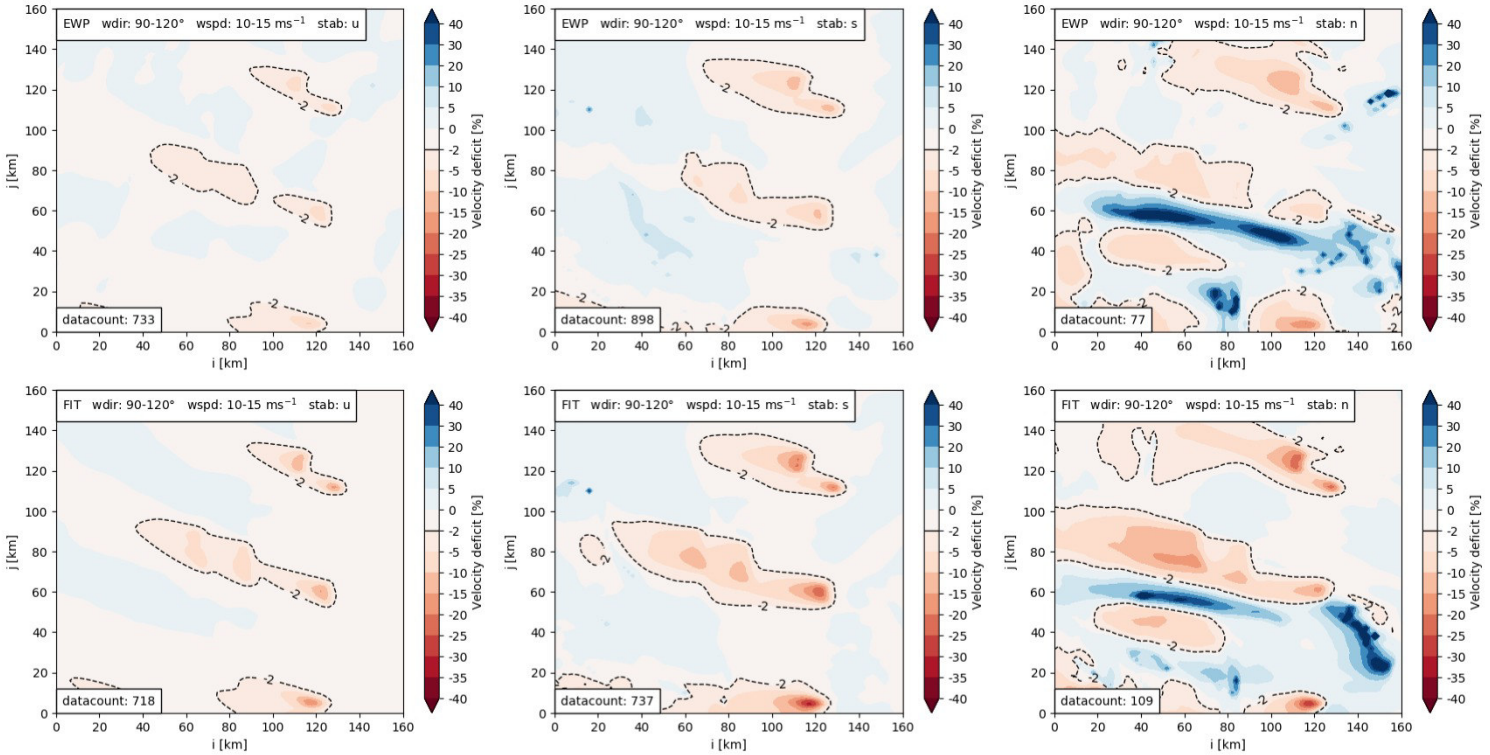

Figure B.11: Wind speed deficit at hub height for wind directions 90-120° and wind speeds 10-15 ms^{-1}.

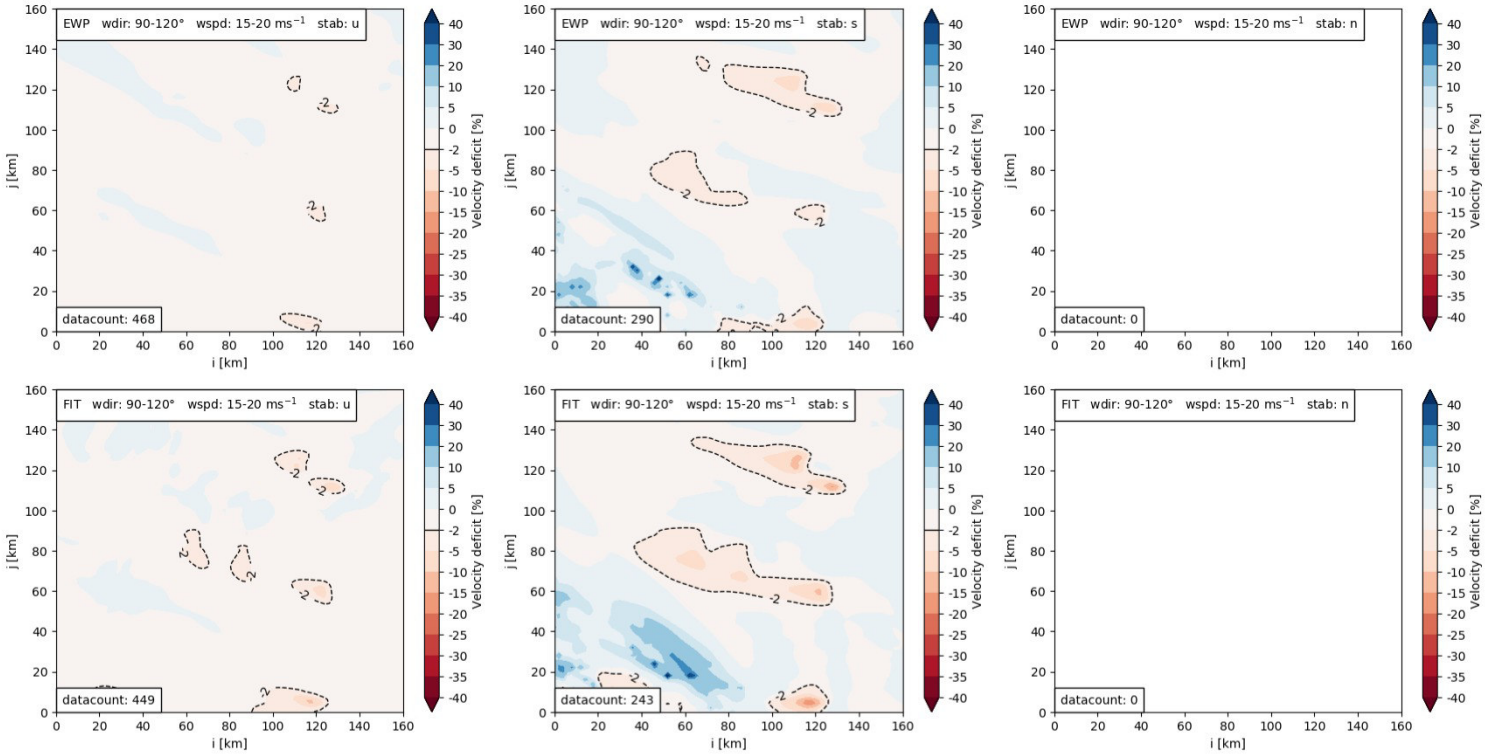

Figure B.12: Wind speed deficit at hub height for wind directions 90-120° and wind speeds 15-20 ms^{-1}.

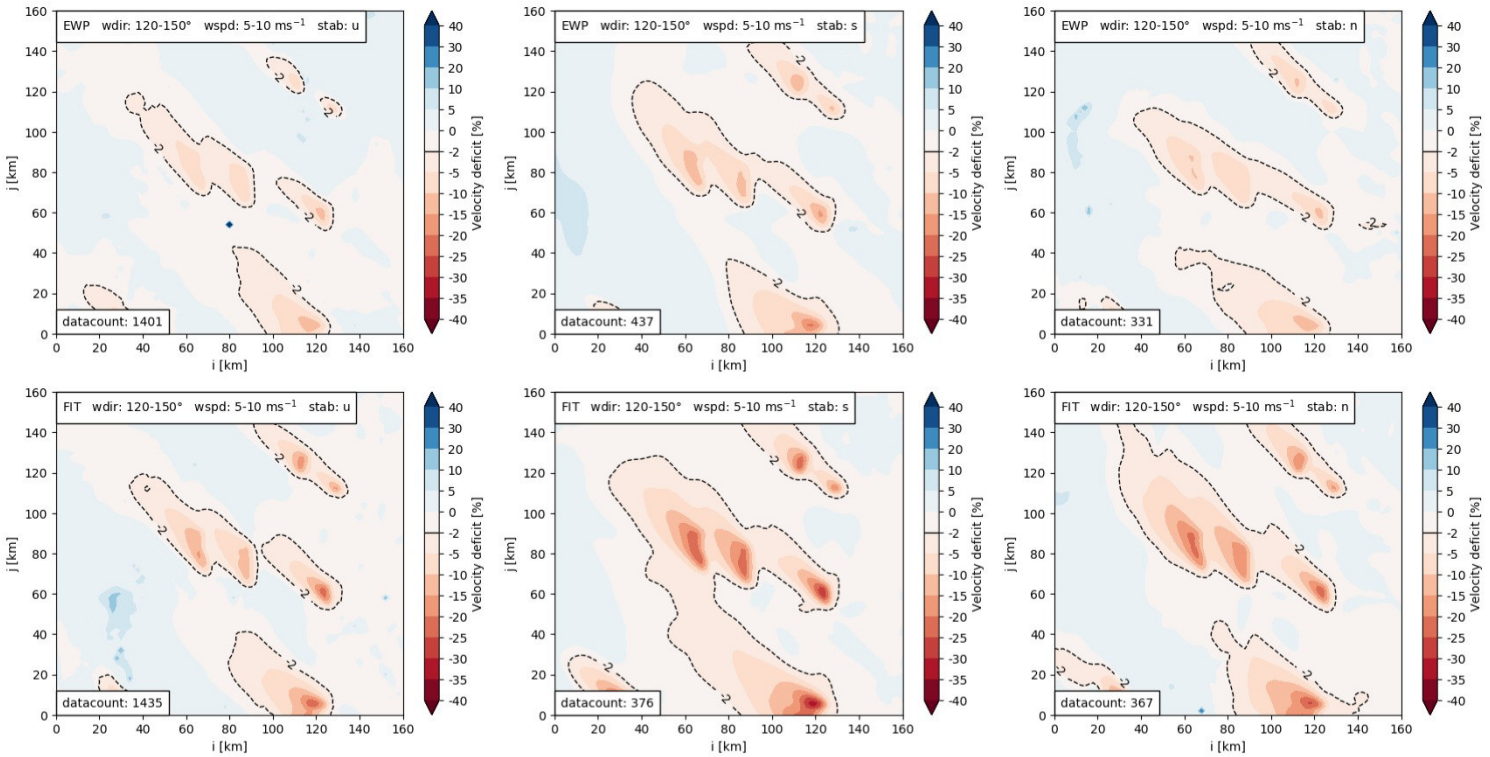

Figure B.13: Wind speed deficit at hub height for wind directions 120-150° and wind speeds 5-10 ms^{-1}.

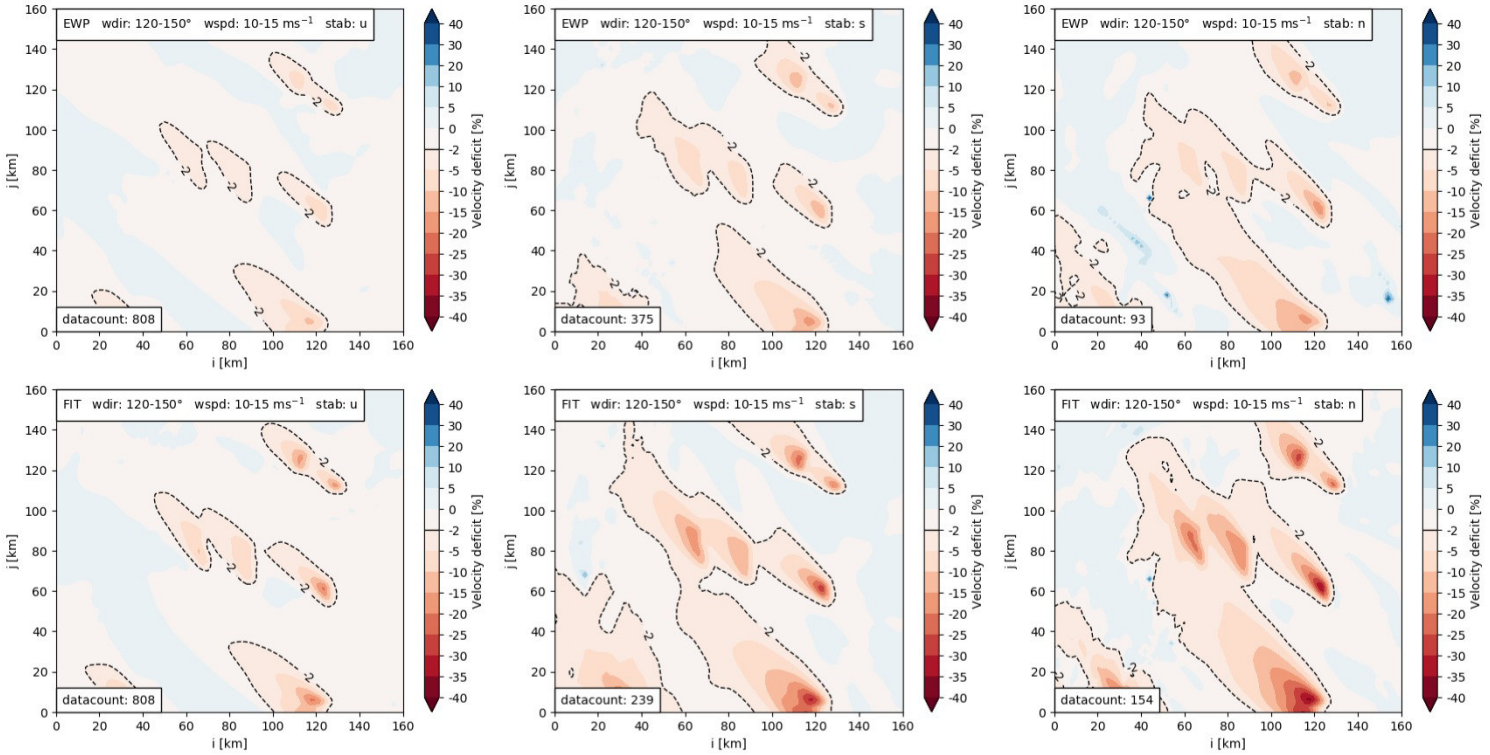

Figure B.14: Wind speed deficit at hub height for wind directions 120-150° and wind speeds 10-15 ms^{-1}.

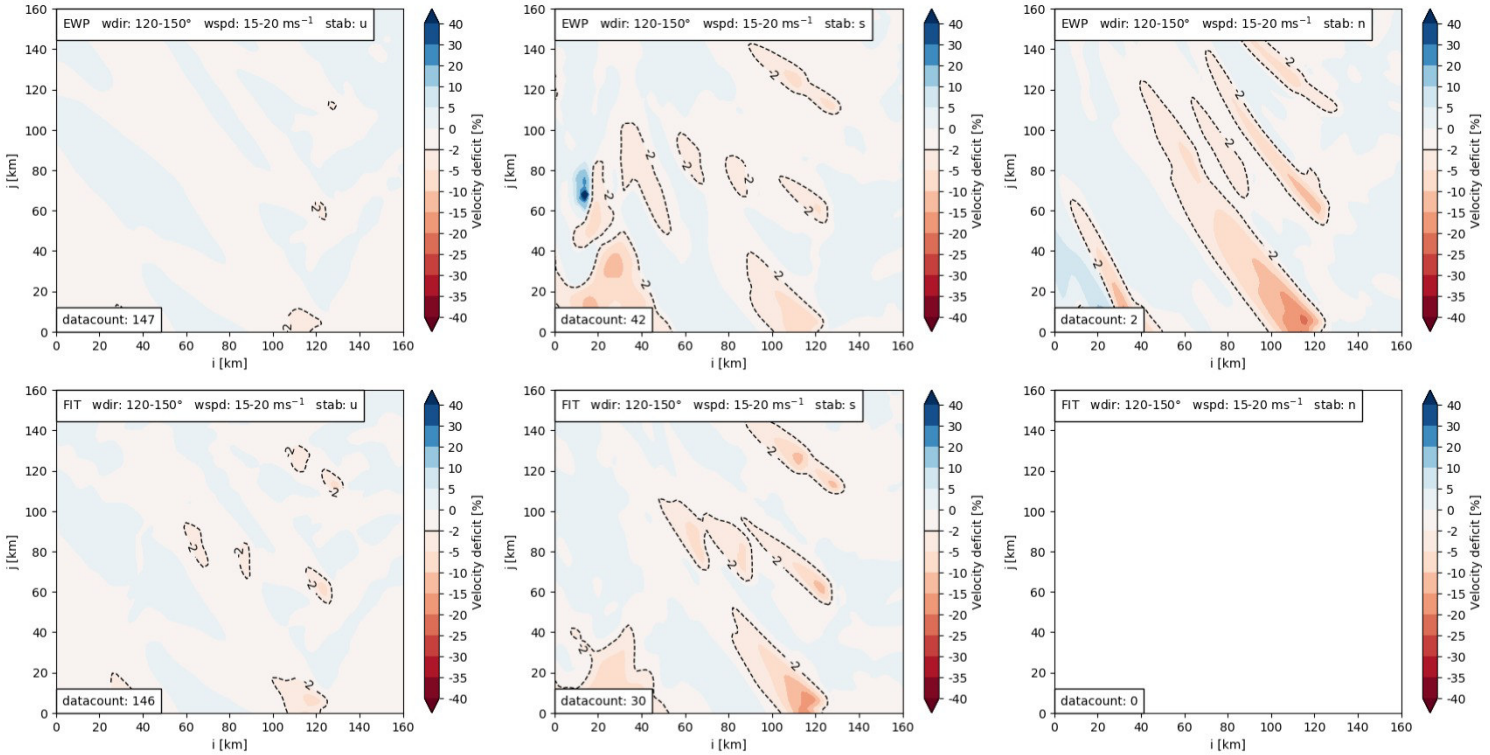

Figure B.15: Wind speed deficit at hub height for wind directions 120-150° and wind speeds 15-20 ms^{-1}.

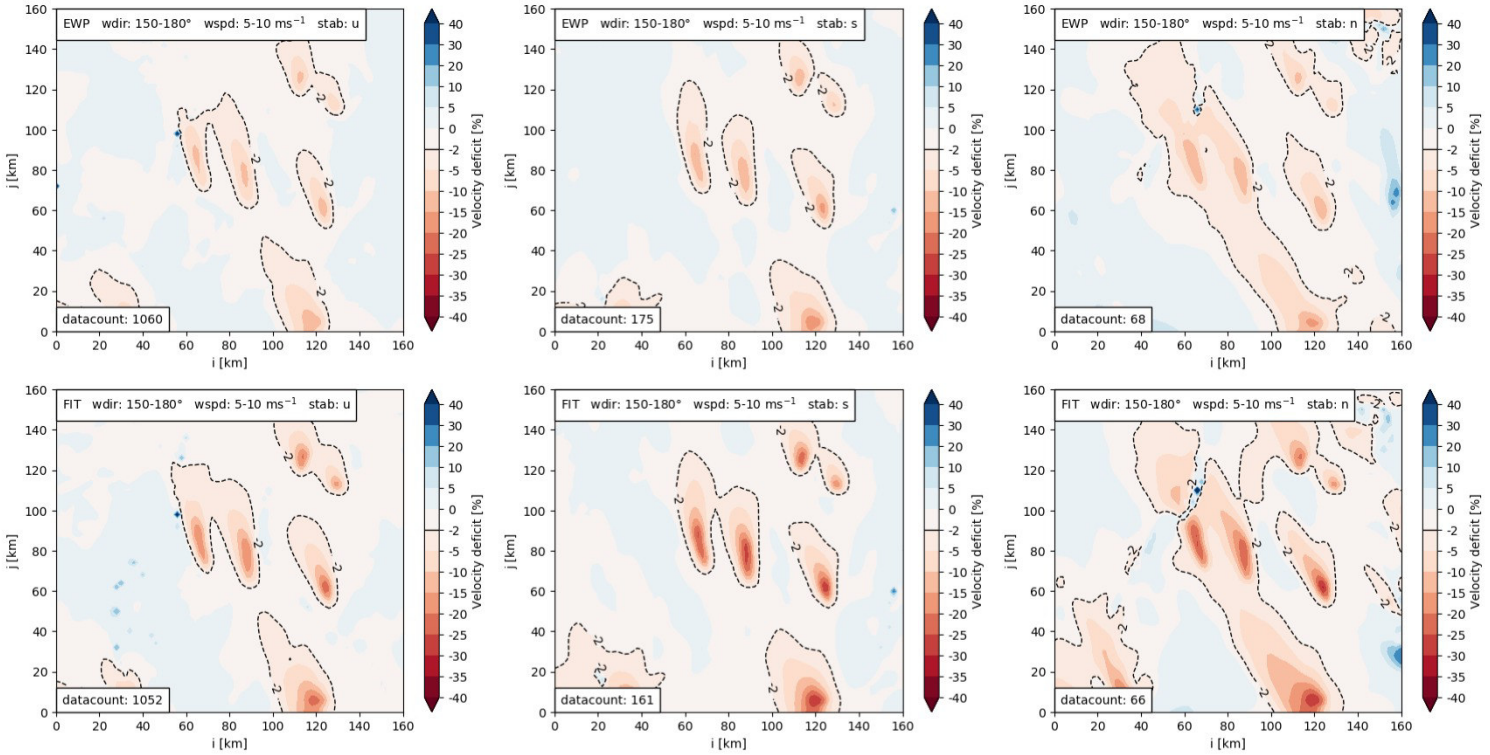

Figure B.16: Wind speed deficit at hub height for wind directions 150-180° and wind speeds 5-10 ms^{-1}.

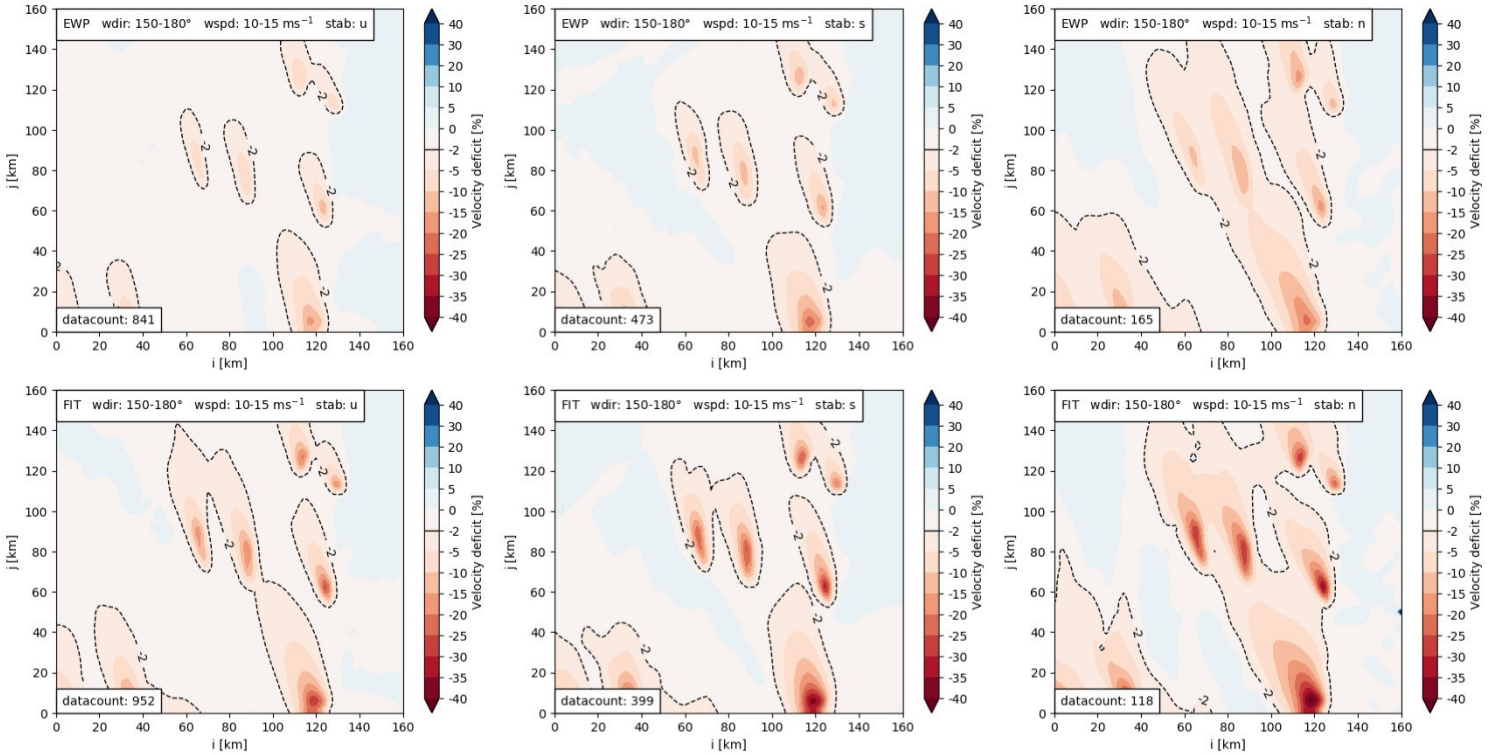

Figure B.17: Wind speed deficit at hub height for wind directions 150-180° and wind speeds 10-15 ms^{-1}.

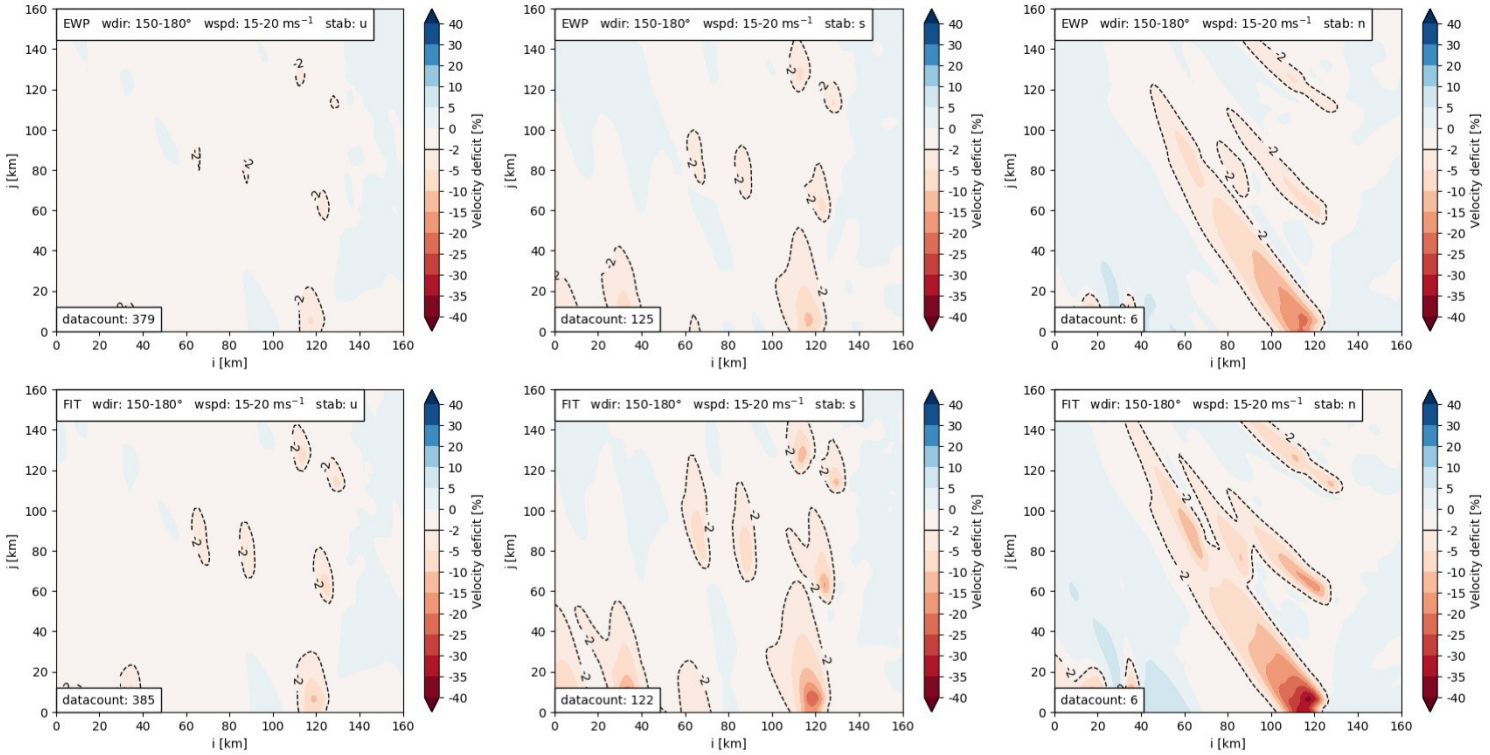

Figure B.18: Wind speed deficit at hub height for wind directions 150-180° and wind speeds 15-20 ms^{-1}.

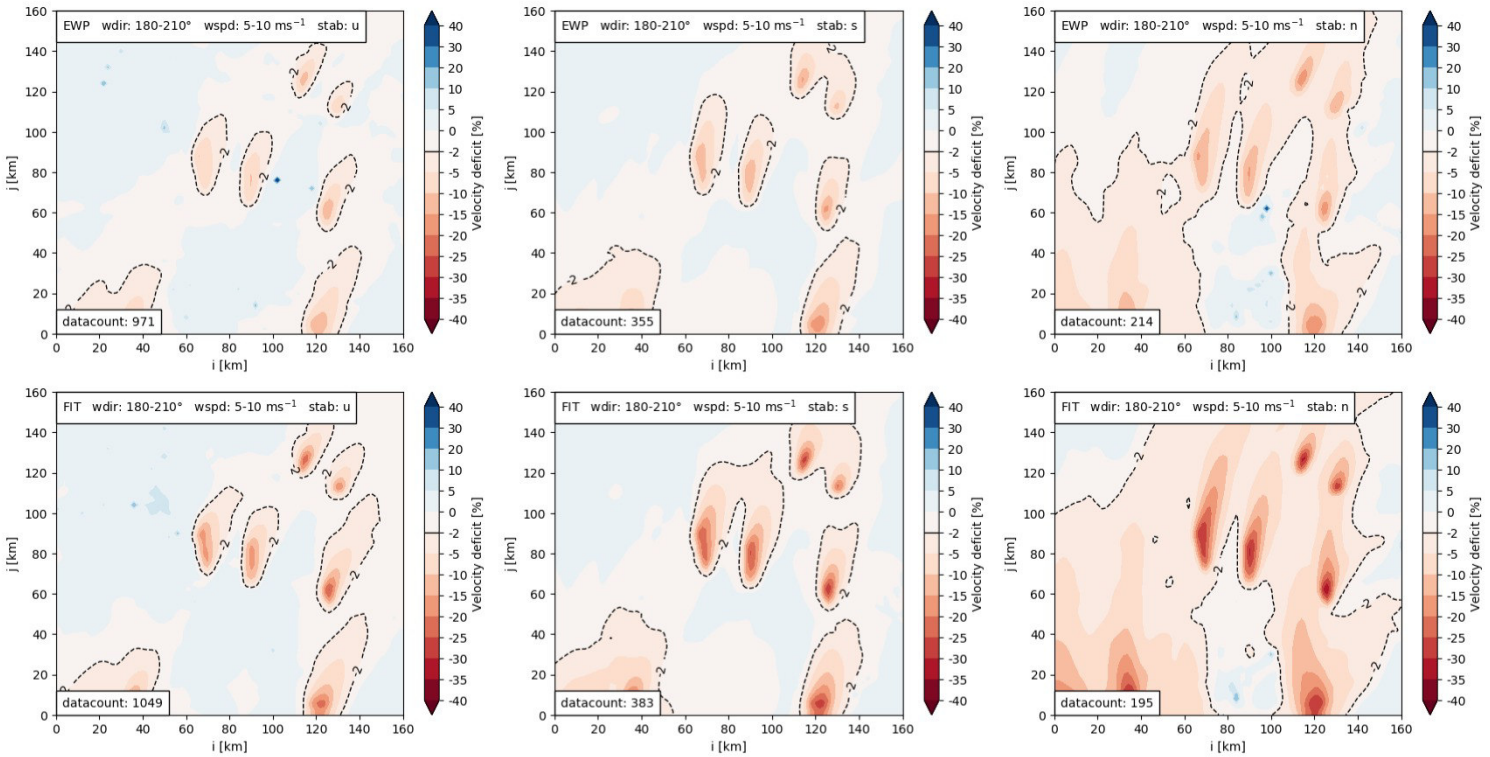

Figure B.19: Wind speed deficit at hub height for wind directions 180-210° and wind speeds 5-10 ms^{-1}.

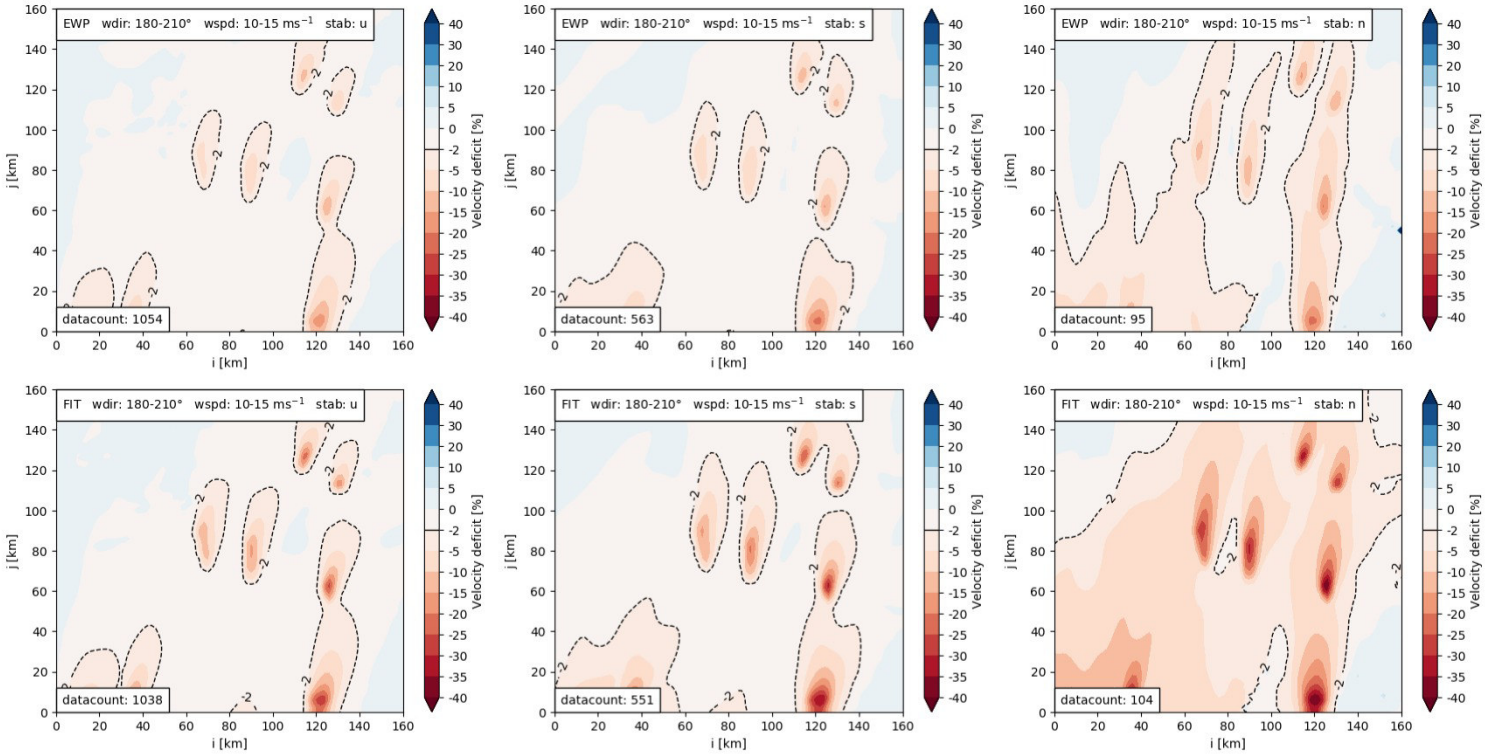

Figure B.20: Wind speed deficit at hub height for wind directions 180-210° and wind speeds 10-15 ms^{-1}.

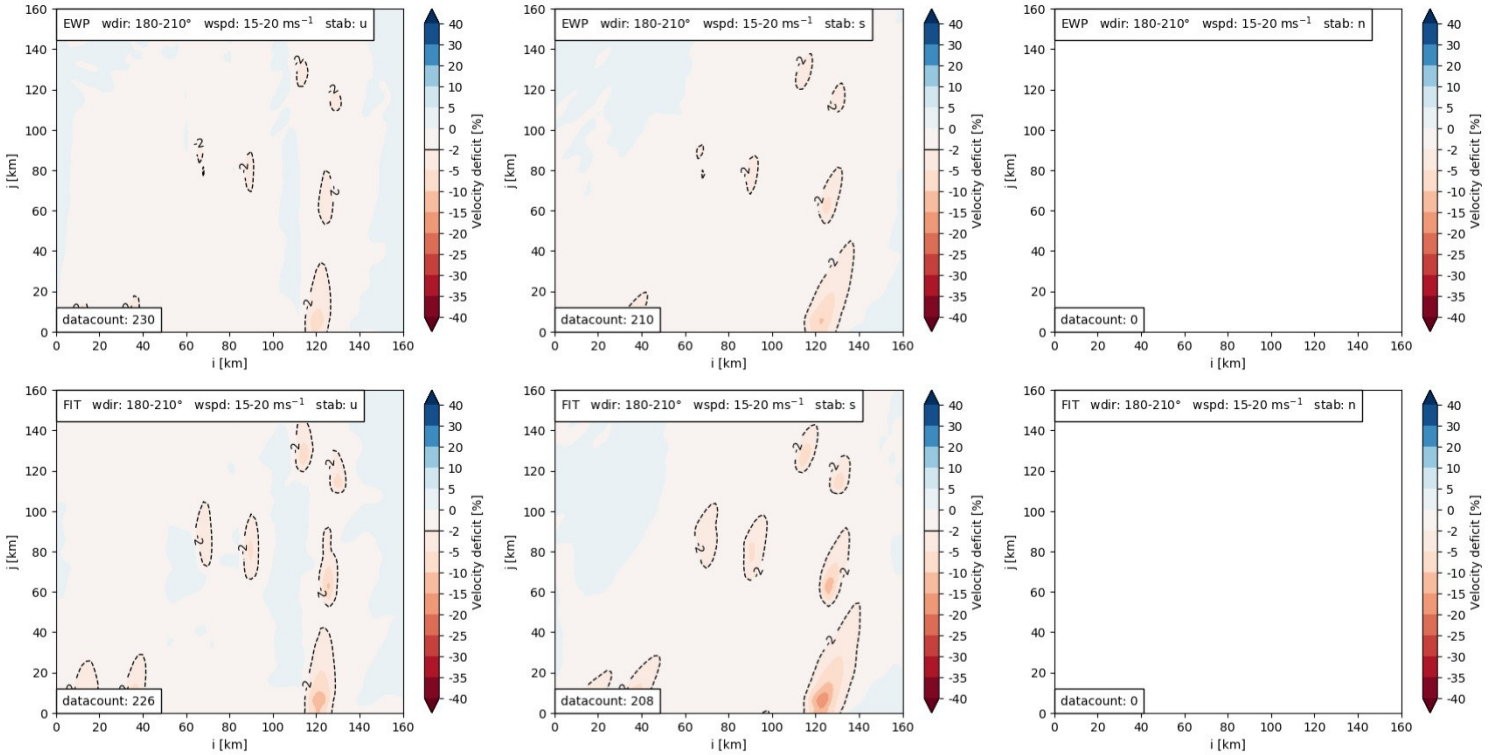

Figure B.21: Wind speed deficit at hub height for wind directions 180-210° and wind speeds 15-20 ms^{-1}.

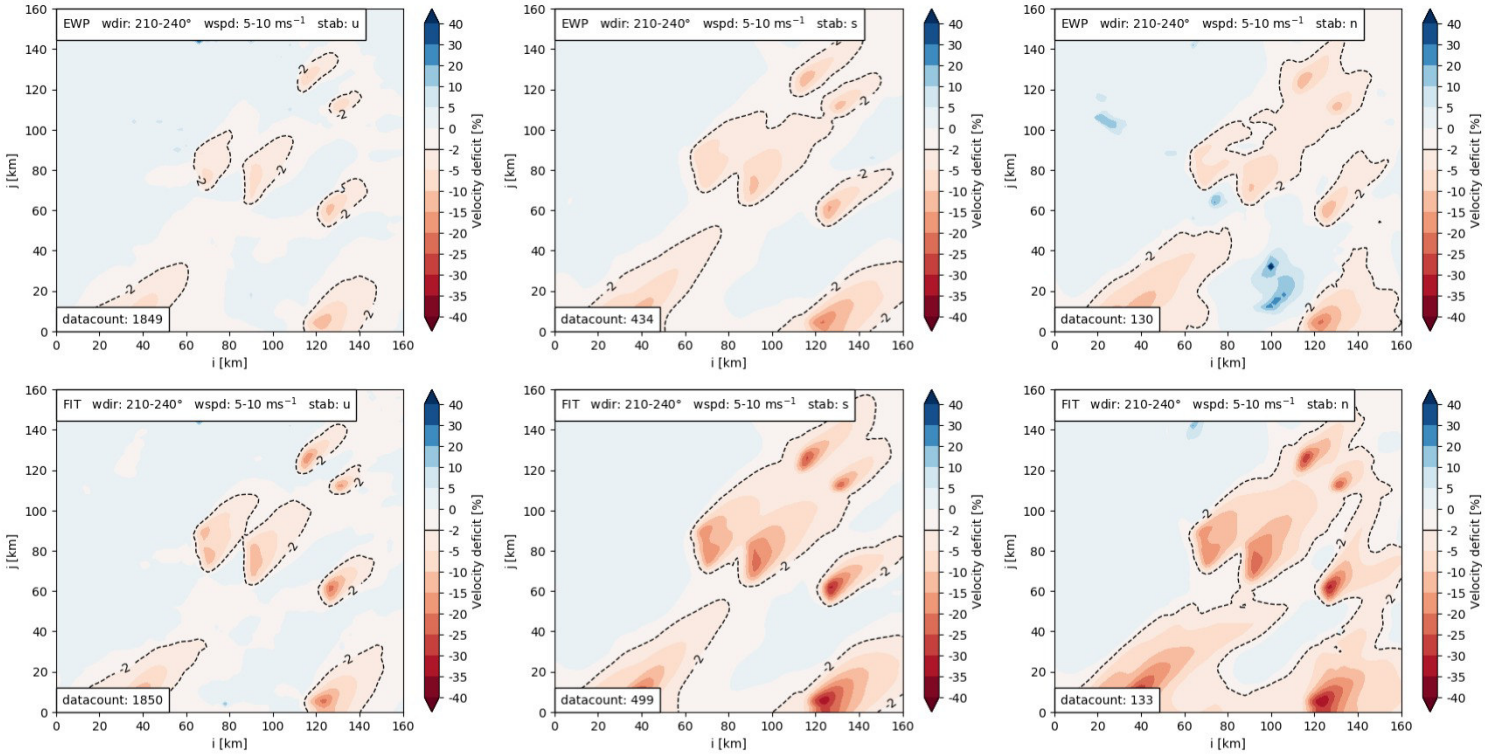

Figure B.22: Wind speed deficit at hub height for wind directions 210-240° and wind speeds 5-10 ms^{-1}.

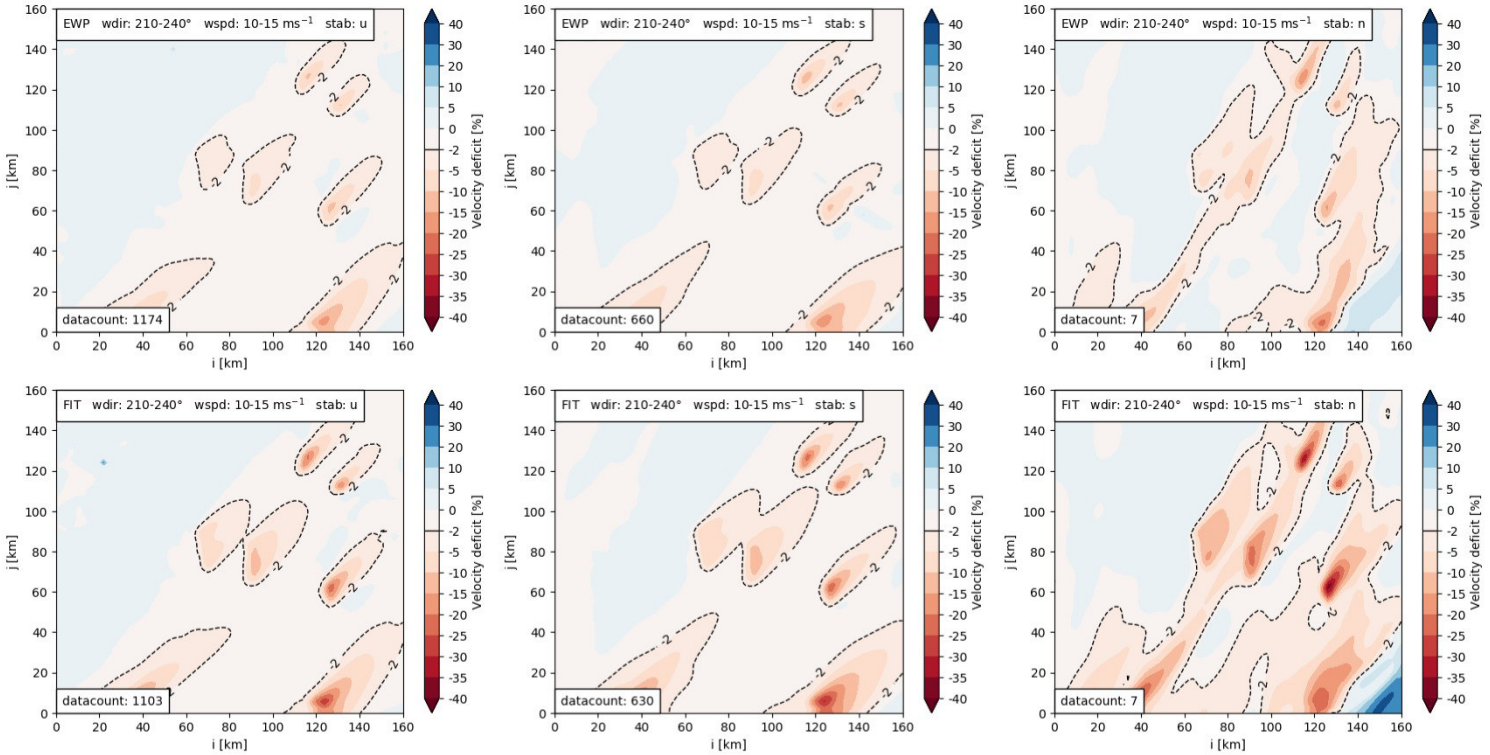

Figure B.23: Wind speed deficit at hub height for wind directions 210-240° and wind speeds 10-15 ms^{-1}.

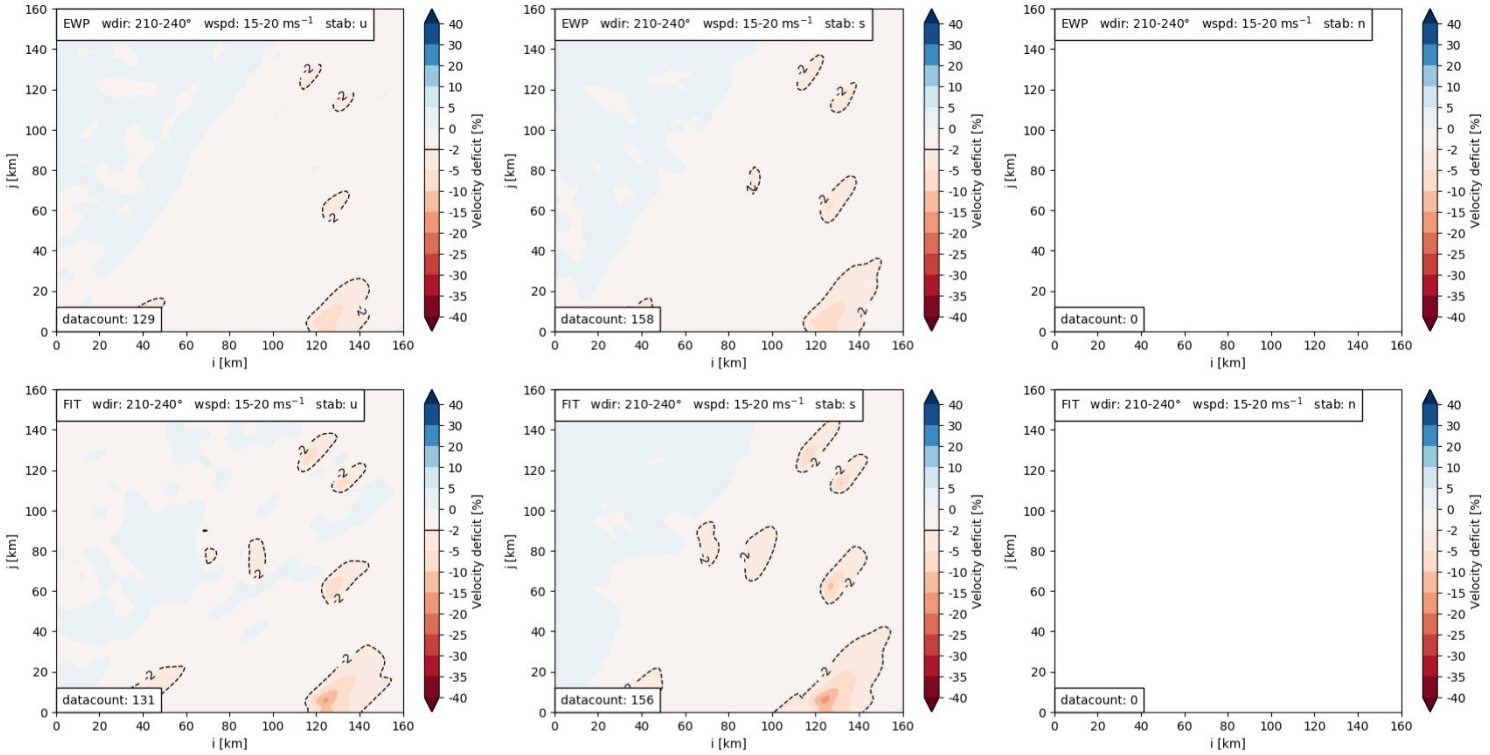

Figure B.24: Wind speed deficit at hub height for wind directions 210-240° and wind speeds 15-20 ms^{-1}.

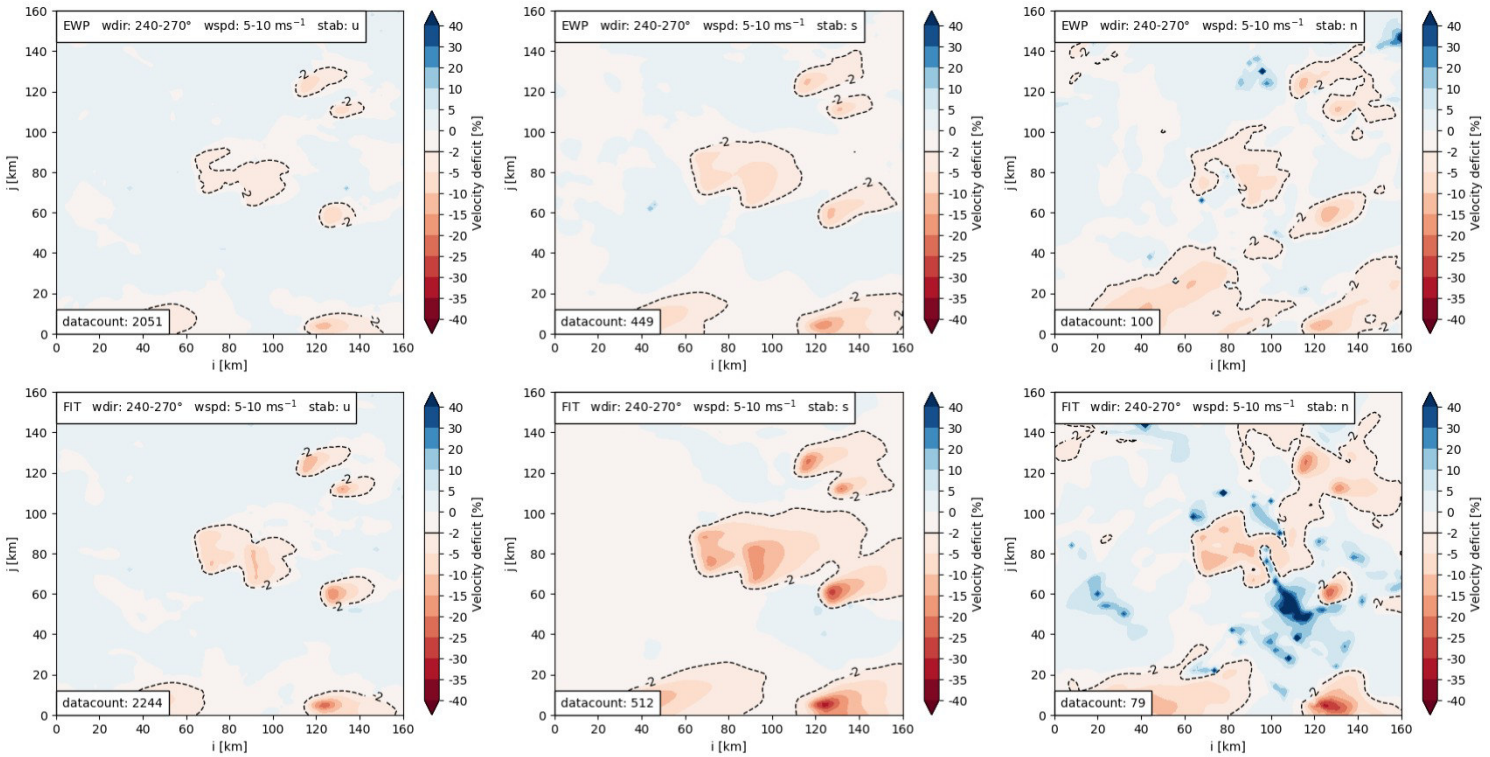

Figure B.25: Wind speed deficit at hub height for wind directions 240-270° and wind speeds 5-10 ms^{-1}.

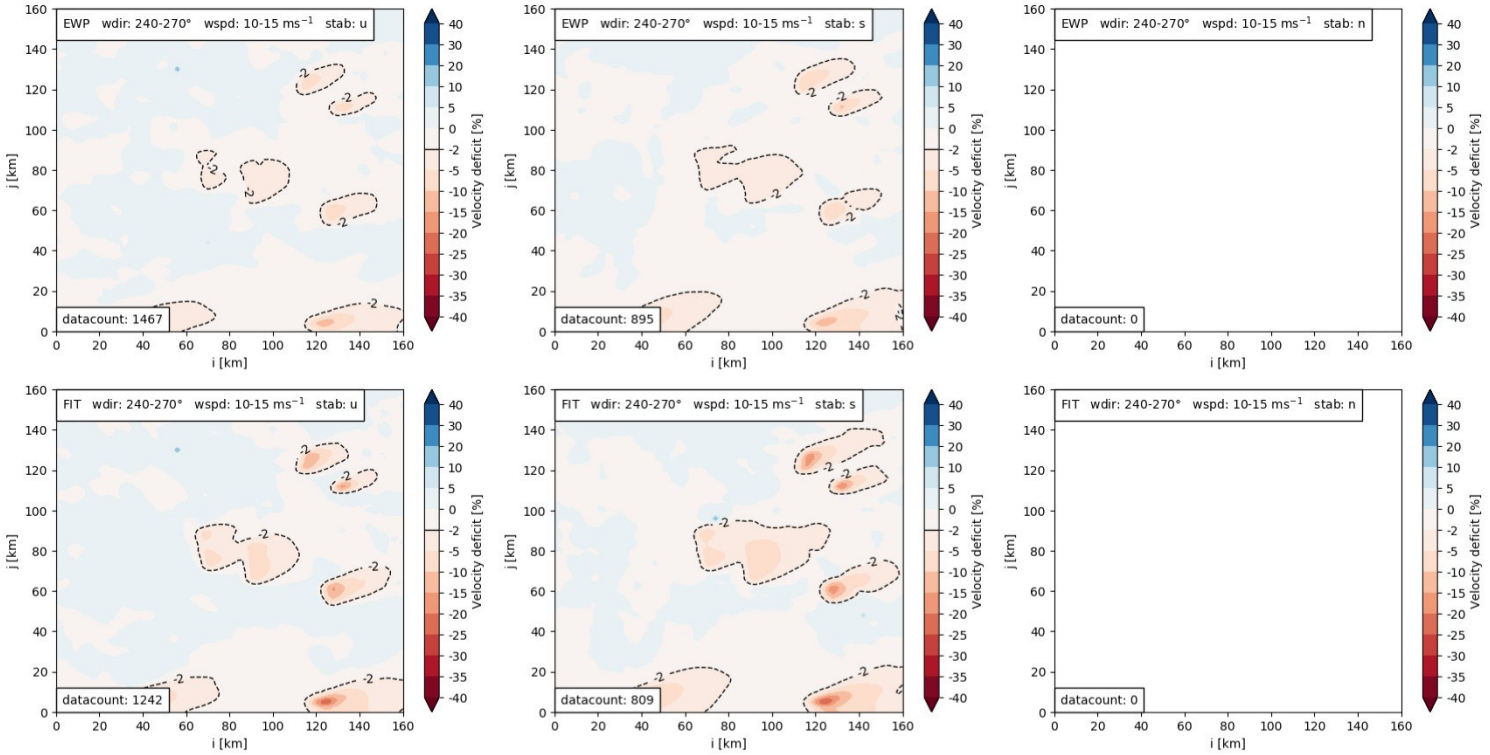

Figure B.26: Wind speed deficit at hub height for wind directions 240-270° and wind speeds 10-15 ms^{-1}.

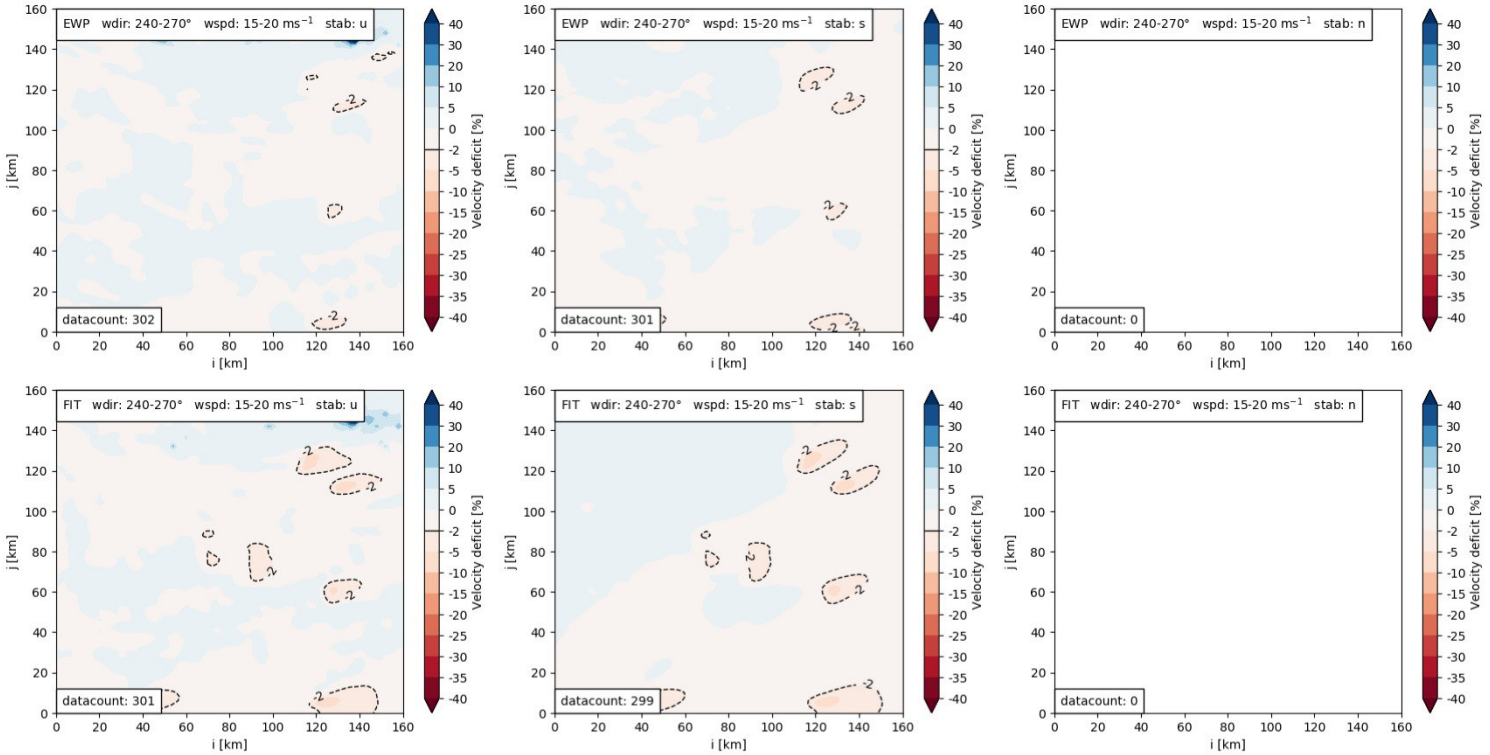

Figure B.27: Wind speed deficit at hub height for wind directions 240-270° and wind speeds 15-20 ms^{-1}.

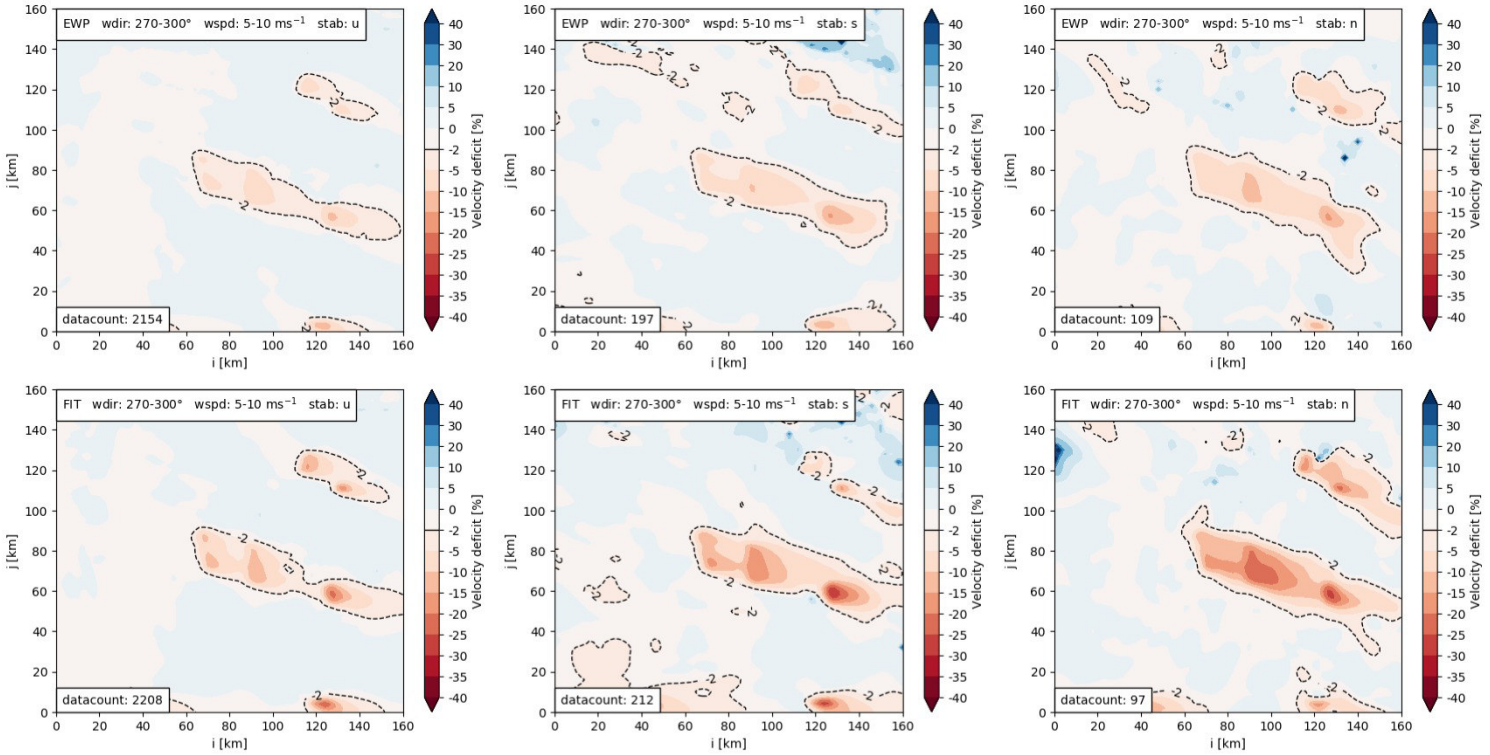

Figure B.28: Wind speed deficit at hub height for wind directions 270-300° and wind speeds 5-10 ms^{-1}.

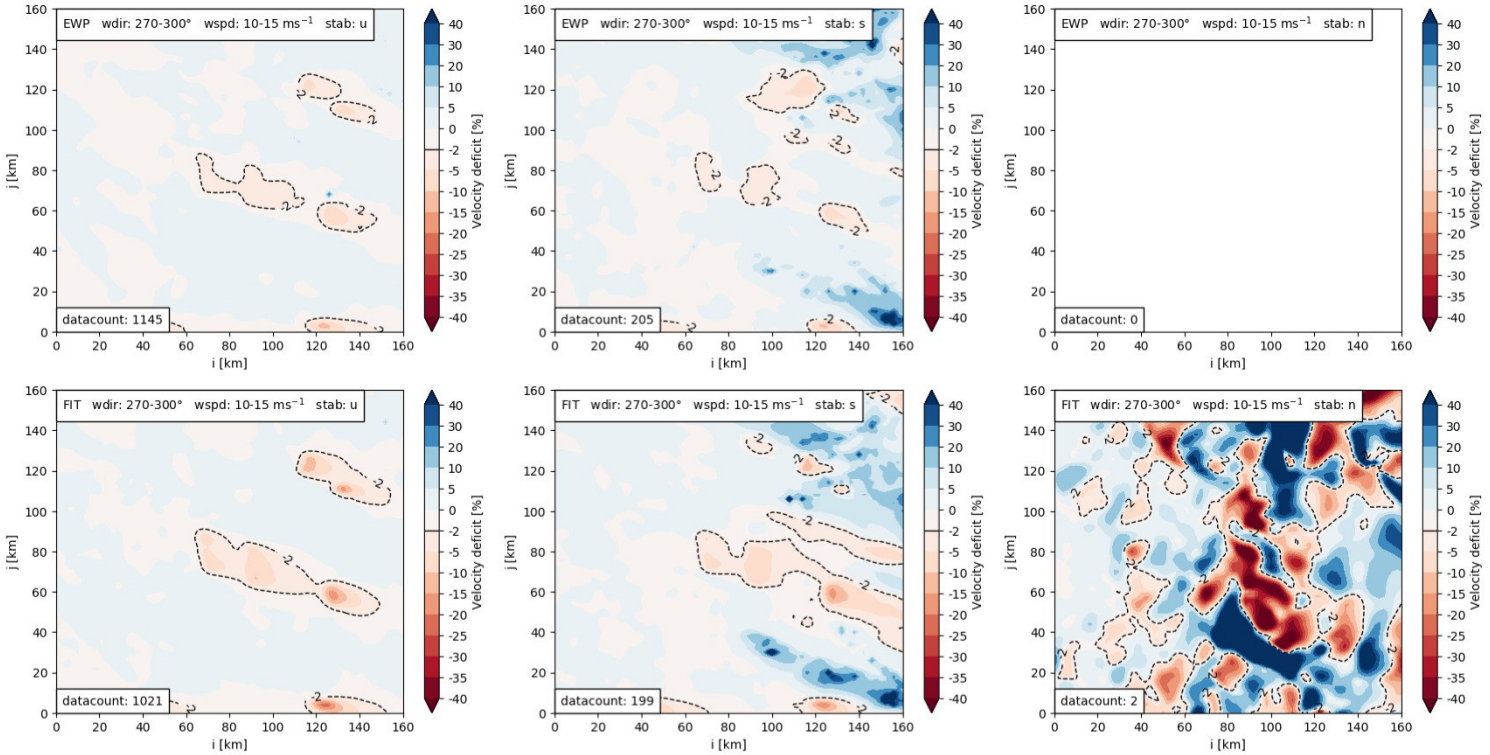

Figure B.29: Wind speed deficit at hub height for wind directions 270-300° and wind speeds 10-15 ms^{-1}.

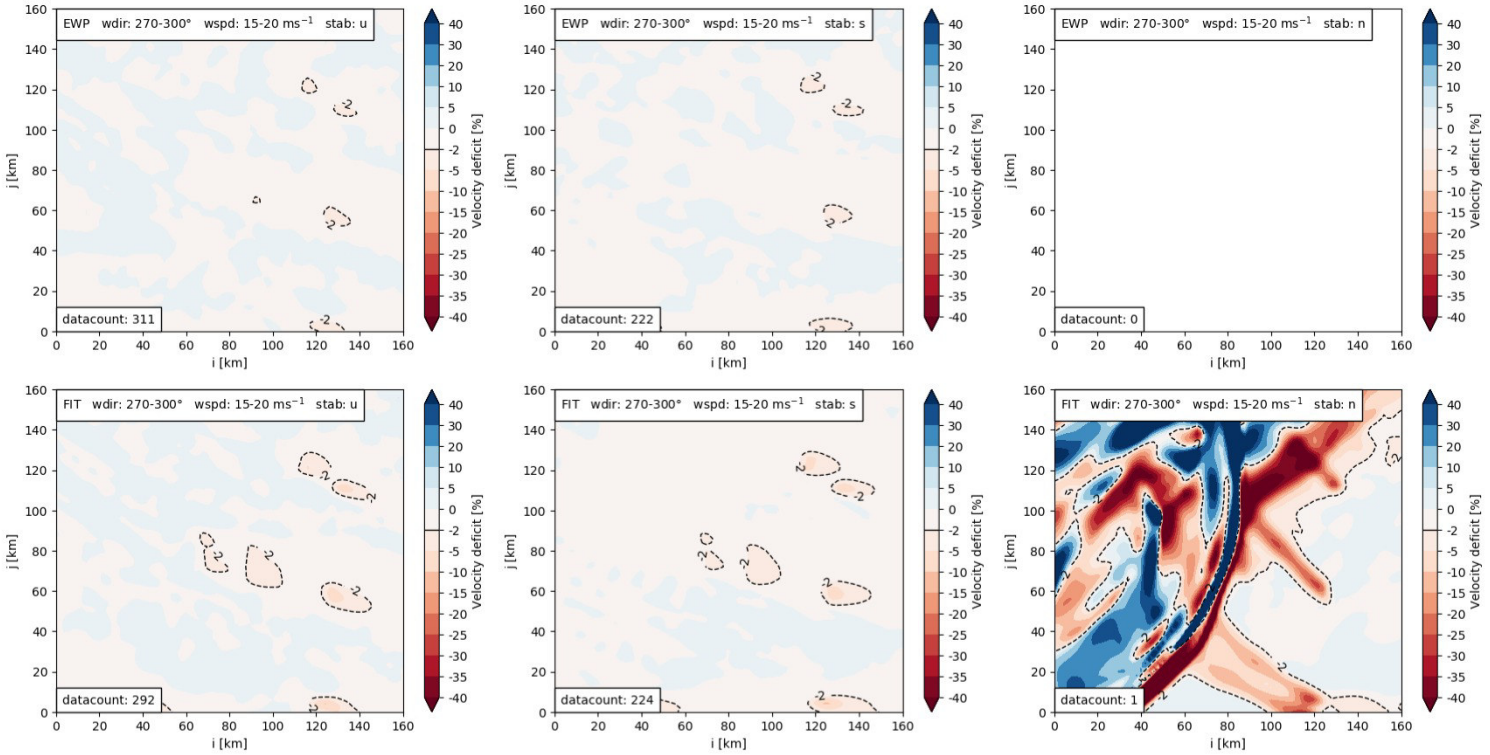

Figure B.30: Wind speed deficit at hub height for wind directions 270-300° and wind speeds 15-20 ms^{-1}.

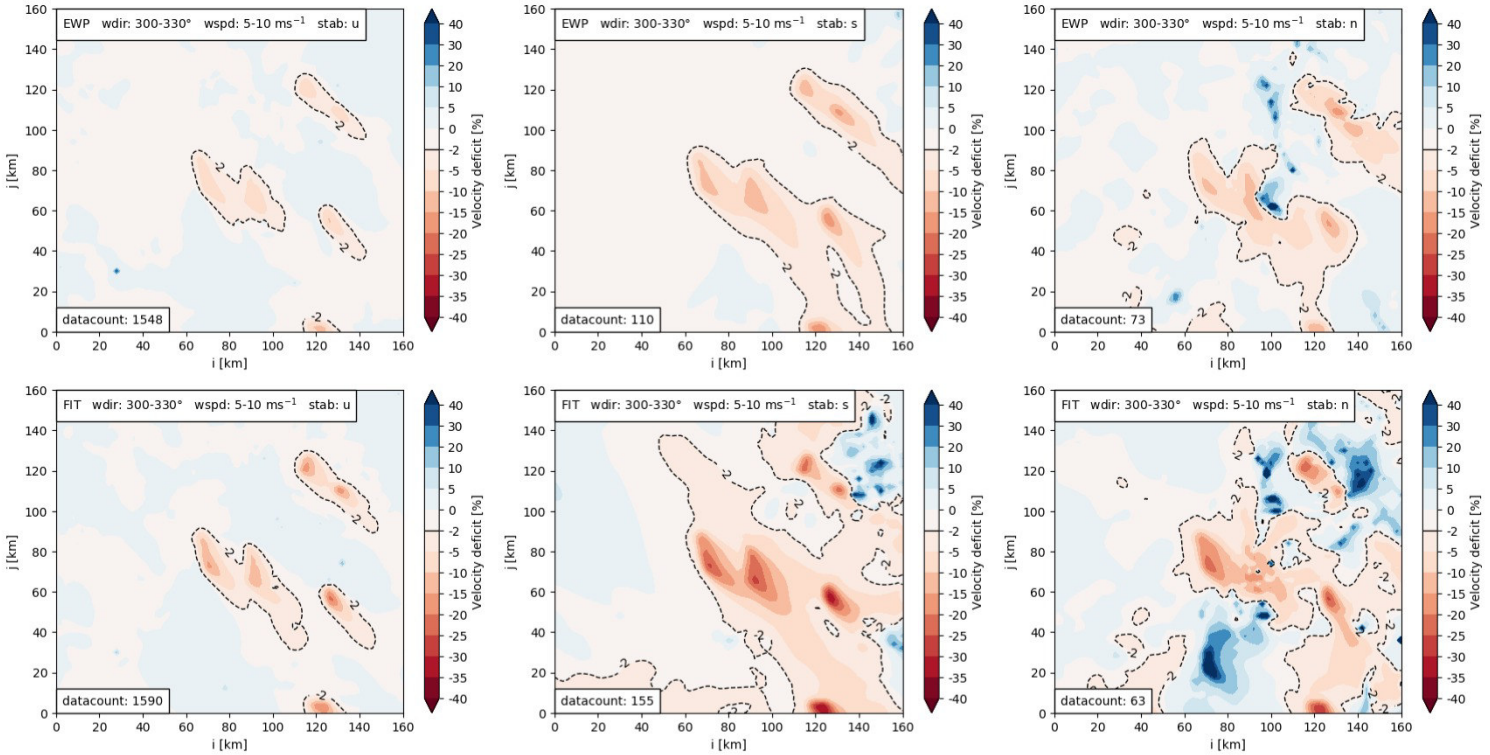

Figure B.31: Wind speed deficit at hub height for wind directions 300-330° and wind speeds 5-10 ms^{-1}.

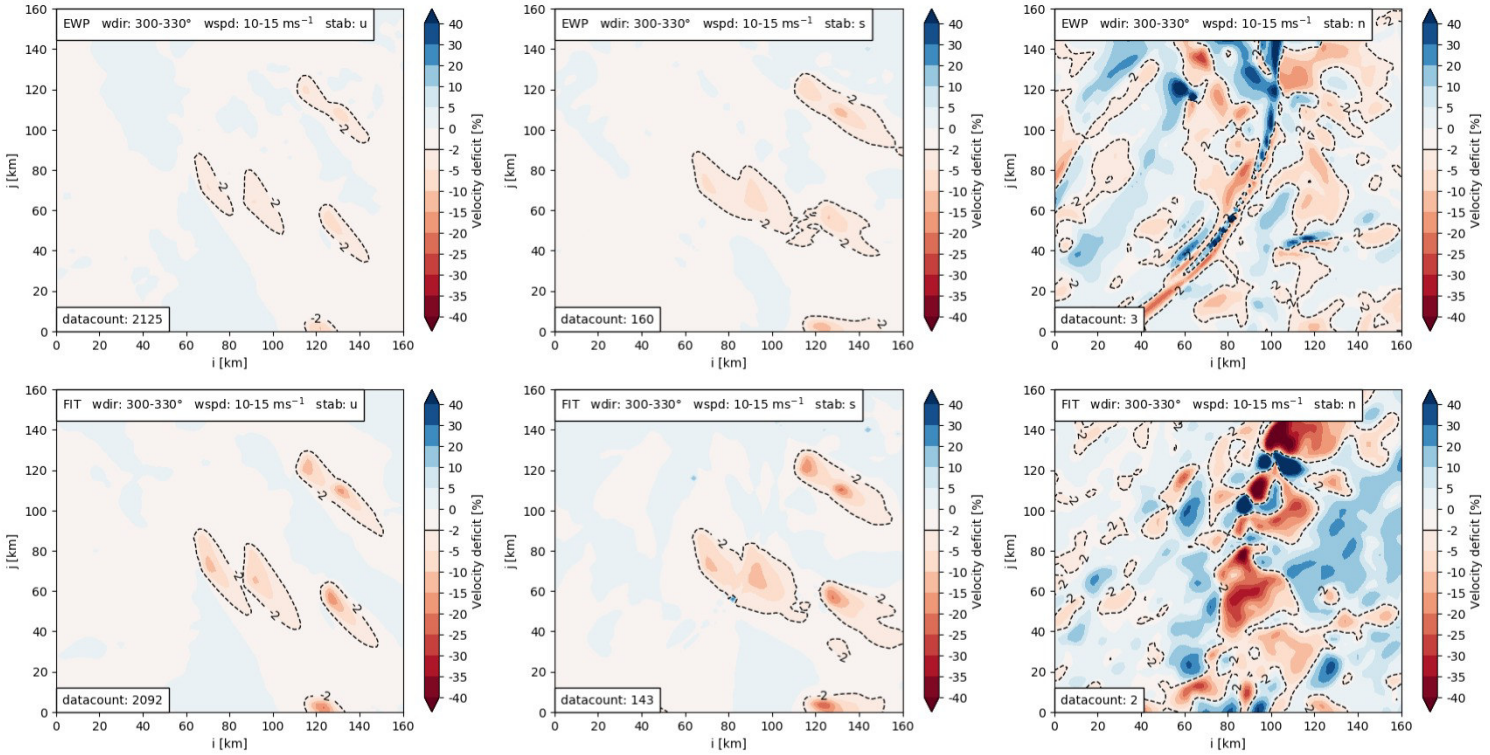

Figure B.32: Wind speed deficit at hub height for wind directions 300-330° and wind speeds 10-15 ms^{-1}.

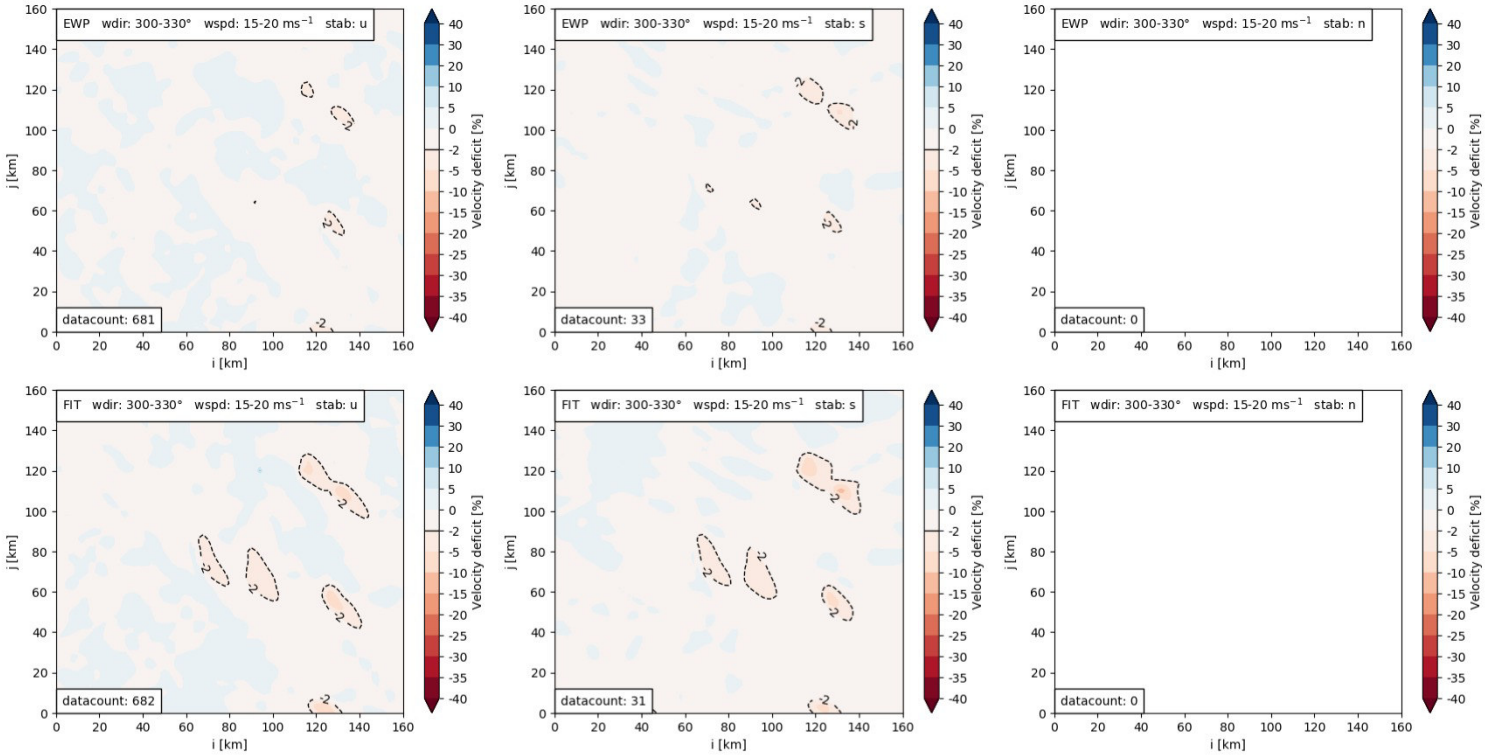

Figure B.33: Wind speed deficit at hub height for wind directions 300-330° and wind speeds 15-20 ms^{-1}.

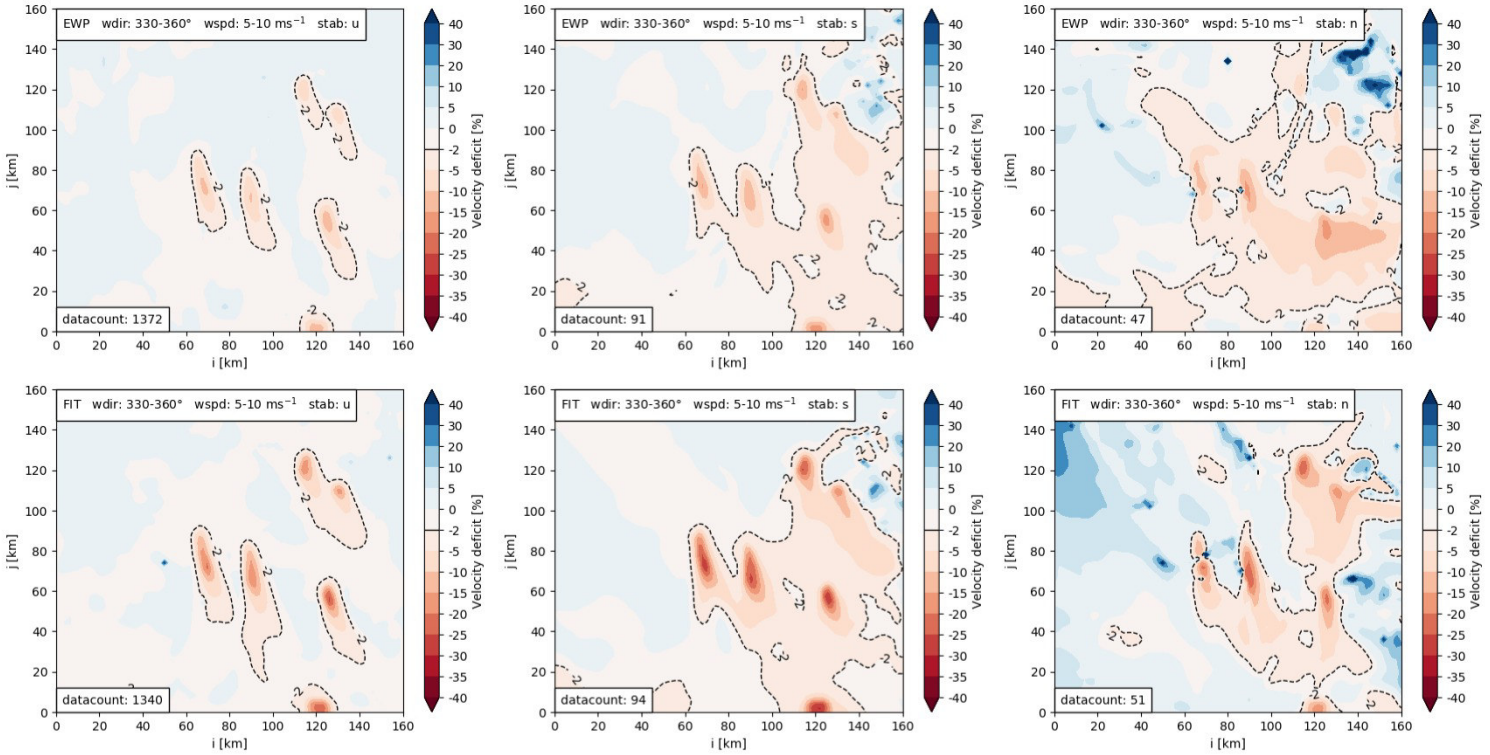

Figure B.34: Wind speed deficit at hub height for wind directions 330-360° and wind speeds 5-10 ms^{-1}.

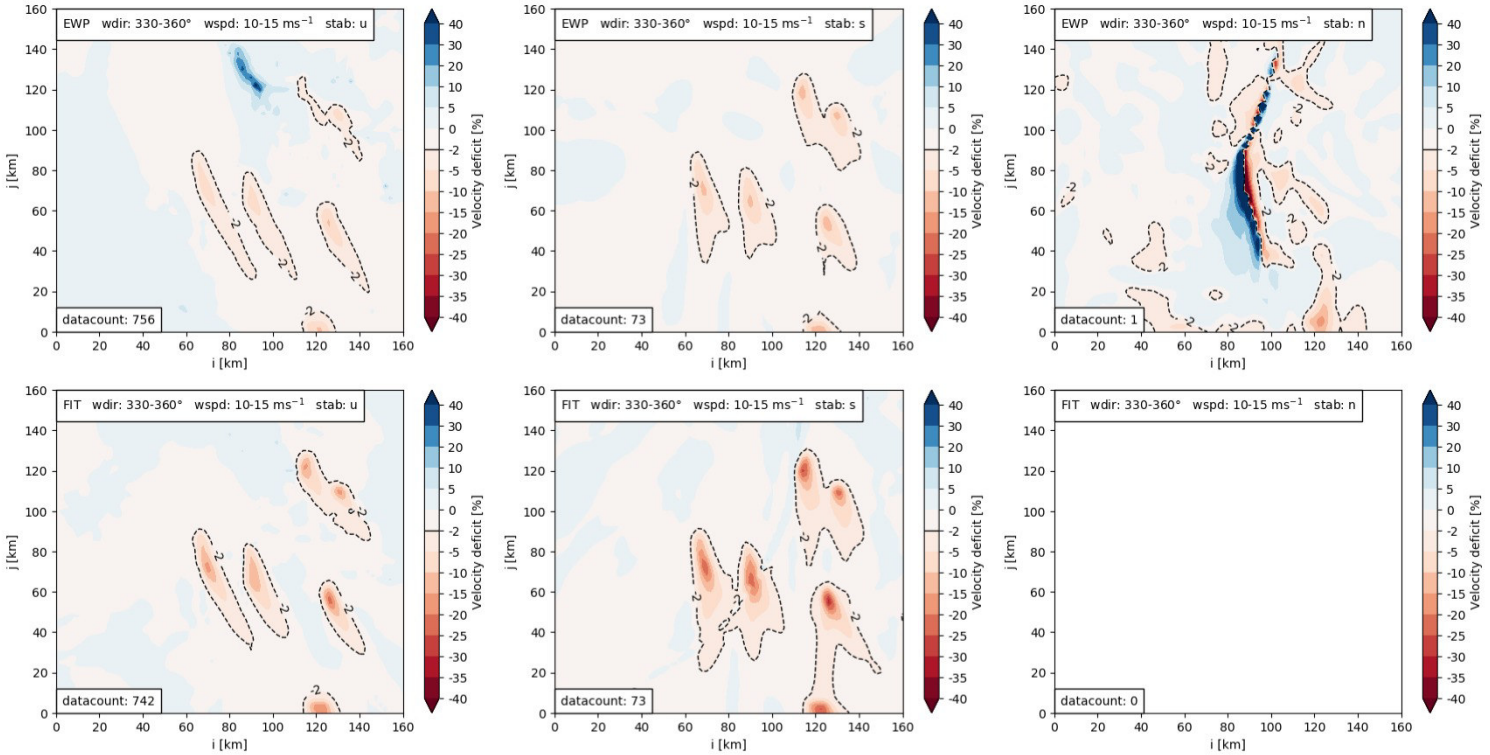

Figure B.35: Wind speed deficit at hub height for wind directions 330-360° and wind speeds 10-15 ms^{-1}.

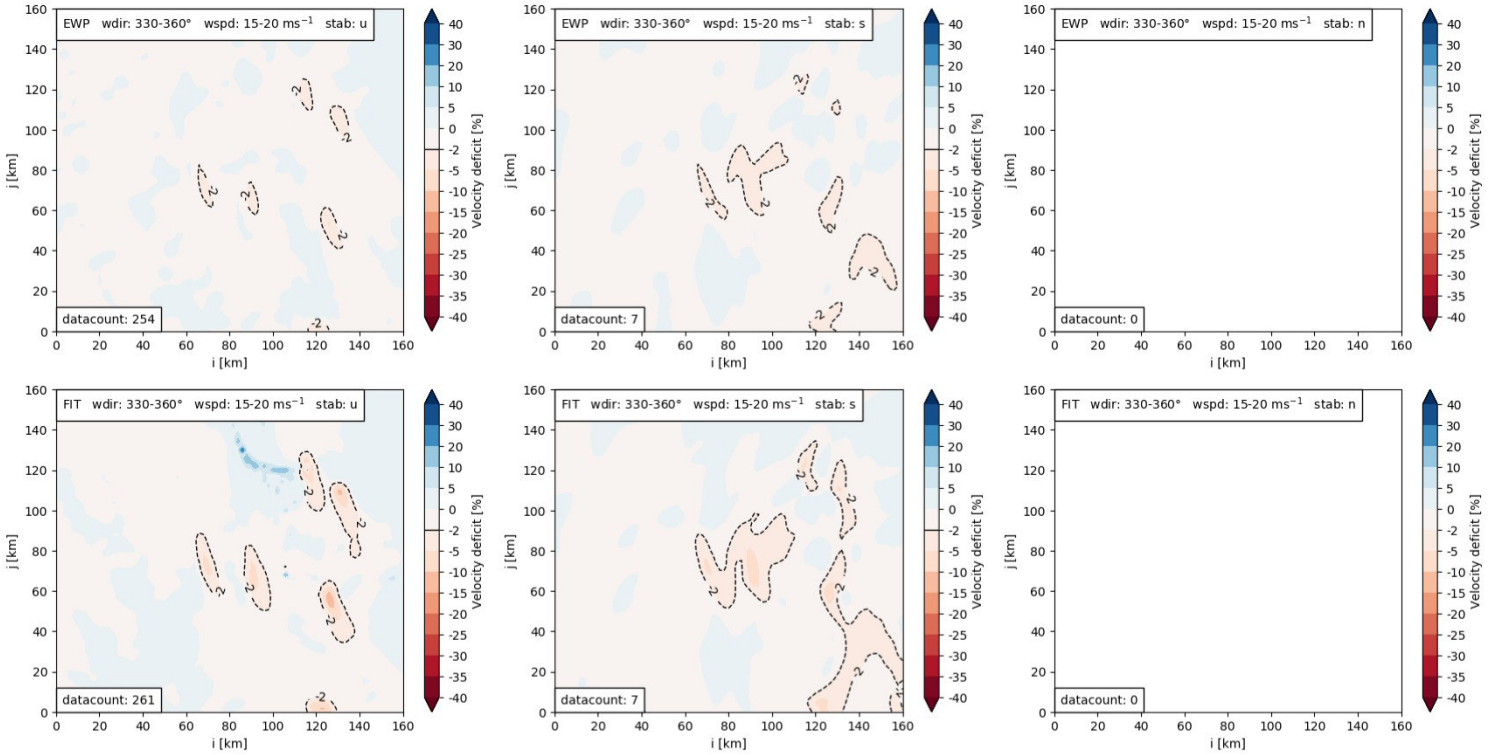

Figure B.36: Wind speed deficit at hub height for wind directions 330-360° and wind speeds 15-20 ms^{-1}.

APPENDIX C

In situ data

C.1 DanTysk SCADA data: Nacelle direction

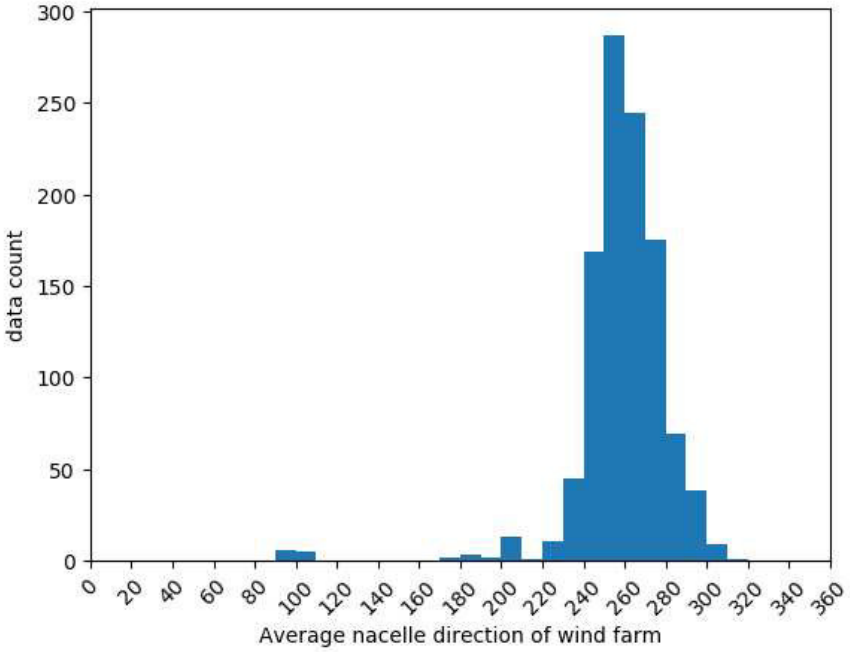

Figure C.1: Average nacelle direction [°] of wind farm for EWP-unstable filtered data.

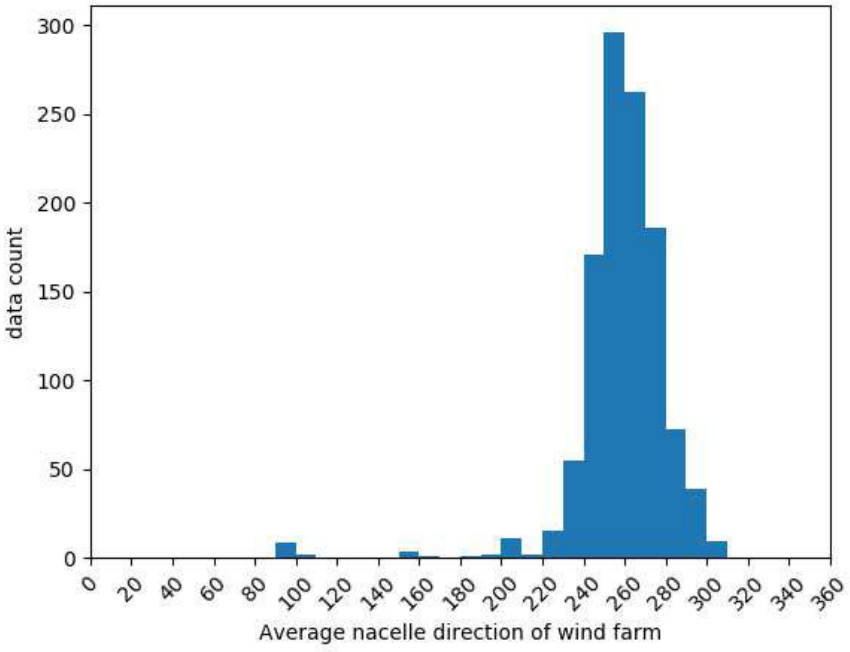

Figure C.2: Average nacelle direction [°] of wind farm for FIT-unstable filtered data.

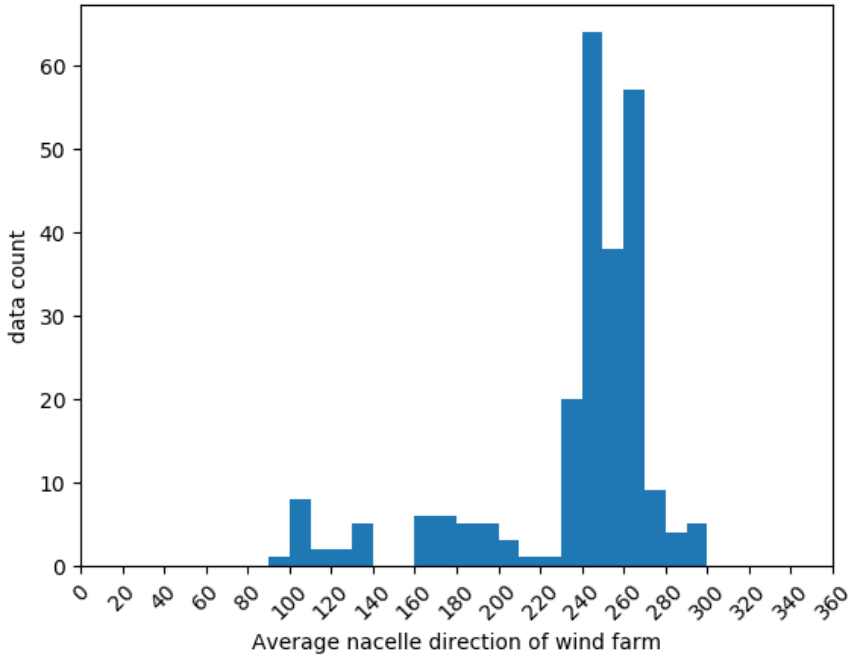

Figure C.3: Average nacelle direction [°] of wind farm for EWP-stable filtered data.

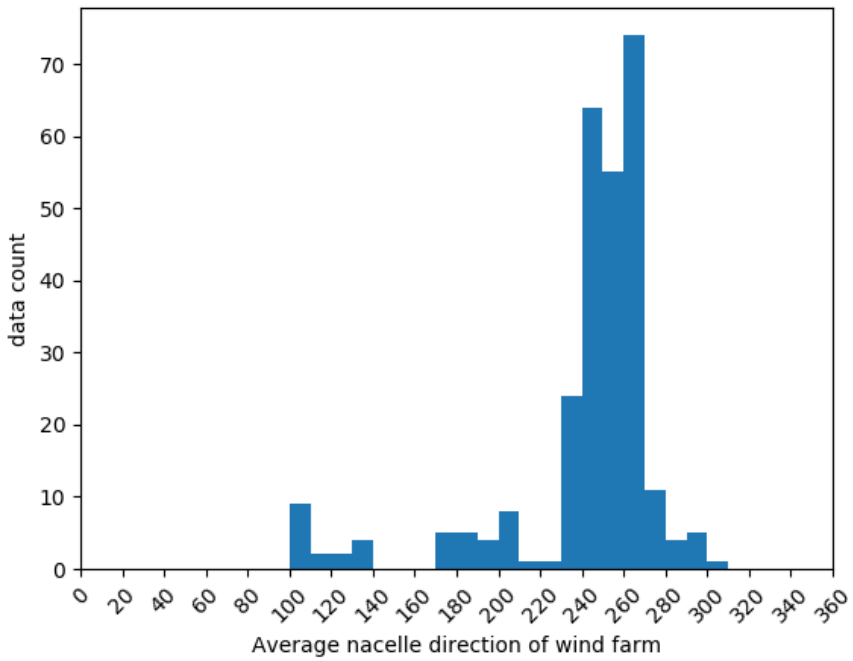

Figure C.4: Average nacelle direction [°] of wind farm for FIT-stable filtered data.

C.2 DanTysk SCADA data: Wind speed

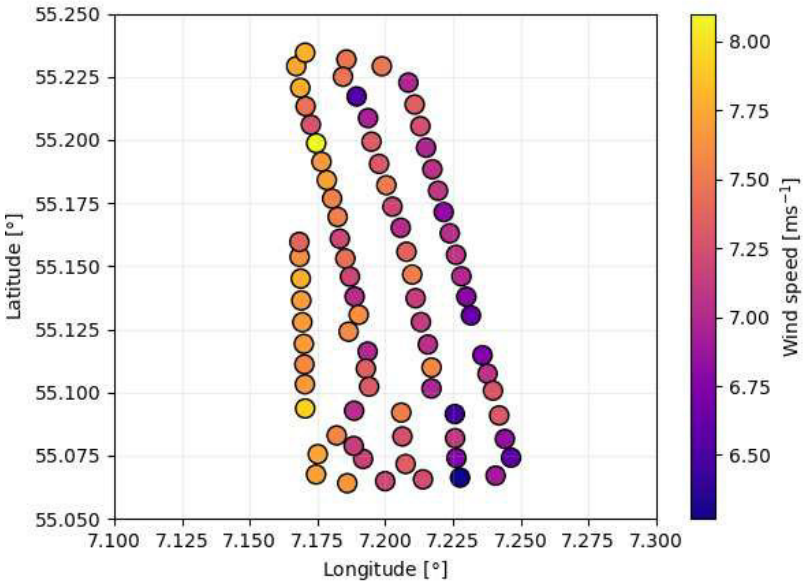

Figure C.5: Average wind speed [ms^{-1}] of wind turbines for EWP-unstable filtered data.

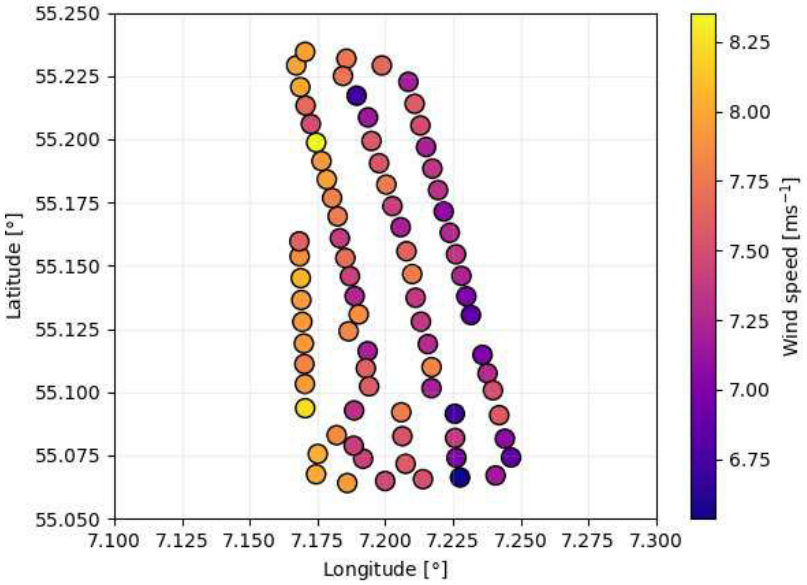

Figure C.6: Average wind speed [ms^{-1}] of wind turbines for FIT-unstable filtered data.

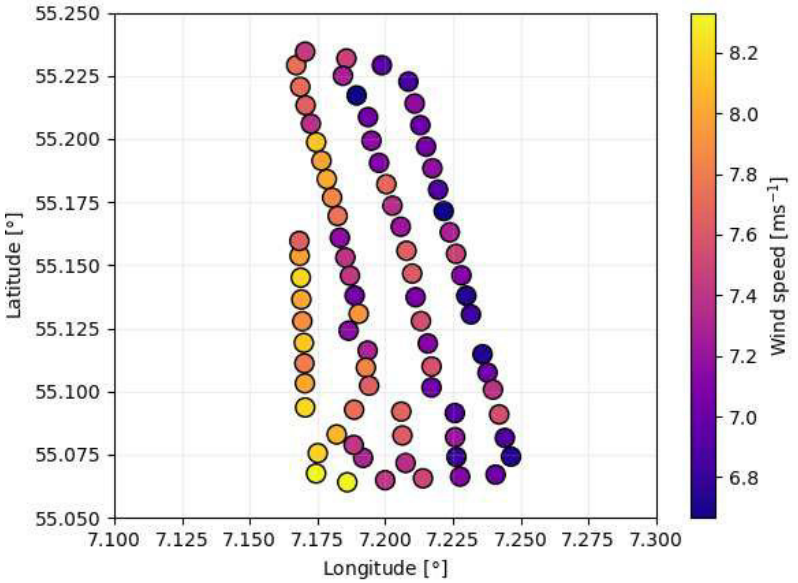

Figure C.7: Average wind speed [ms^{-1}] of wind turbines for EWP-stable filtered data.

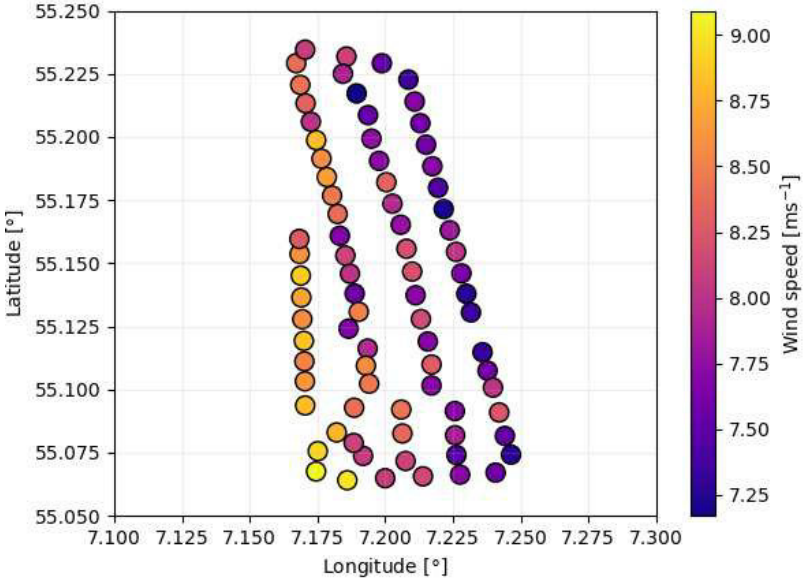

Figure C.8: Average wind speed [ms^{-1}] of wind turbines for FIT-stable filtered data.

References

Agora (2020). *Making the Most of Offshore Wind: Re-Evaluating the Potential of Offshore Wind in the German North Sea.* Agora Energiewende, Agora Verkehrswende, Technical University of Denmark and Max-Planck-Institute for Biogeochemistry.

Baidya Roy, S., S. W. Pacala, and R. L. Walko (2004). "Can large wind farms affect local meteorology?" In: *Journal of geophysical research* 109. DOI: 10.1029/2004JD004763.

Barthelmie, R. J., K. Hansen, K. Rados, W. Schlez, L. E. Jensen, and S. Neckelmann (2009). "Modelling the impact of wakes on power output at Nysted and Horns Rev". In: *European Wind Energy Conference and Exhibition 2009, EWEC 2009* 2.

Barthelmie, R. J. and L. E. Jensen (2010). "Evaluation of wind farm efficiency and wind turbine wakes at the Nysted offshore wind farm". In:

Blahak, U., B. Goretzki, and J. Meis (2010). "A simple parameterization of drag forces induced by large wind farms for numerical weather prediction models". In:

Christiansen, M. B. and C. B. Hasager (2005). "Wake effects of large offshore wind farms identified from satellite SAR". In: *Remote Sensing of Environment* 98.

Djath, B., J. Schulz-Stellenfleth, and B. Cañadillas (2018). "Impact of atmospheric stability on X-band and C-band synthetic aperture radar imagery of offshore windpark wakes". In: *Journal of Renewable and Sustainable Energy* 10. DOI: 10.1063/1.5020437.

Fitch, A. C., J. B Olson, J. K. Lundquist, J. Dudhia, A. K. Gupta, J. Michalakes, and I. Barstad (2012). "Local and mesoscale impacts of wind farms as parameterized in a mesoscale NWP model". In: *Monthly Weather Review* 140. DOI: 10.1175/MWR-D-11-00352.1.

Gayle Nygaard, N. and A. C. Newcombe (2018). "Wake behind an offshore wind farm observed with dual-Doppler radars". In: *Journal of Physics: Conference Series* 1037. DOI: 10.1088/1742-6596/1037/7/072008.

Hahmann, A. N., C. Vincent, A. Peña, J. Lange, and C. B. Hasager (2014). "Wind climate estimation using WRF model output: Method and model sensitivities over the sea". In: *International Journal of Climatology* 35. DOI: 10.1002/joc.4217.

Hansen, K. S., R. J. Barthelmie, L. E. Jensen, and A. Sommer (2012). "The impact of turbulence intensity and atmospheric stability on power deficits due to wind turbine wakes at Horns Rev wind farm". In: *Wind Energy* 15. DOI: 10.1002/we.512.

Hansen, M. O. L. (2015). "Aerodynamics of wind turbines: Third edition". In: *Aerodynamics of Wind Turbines: Third Edition.* DOI: 10.4324/9781315769981.

Hasager, C. et al. (2015). "Comparing satellite SAR and wind farm wake models". In: *Journal of Physics: Conference Series* 625. DOI: 10.1088/1742-6596/625/1/012035.

Ivanova, L. and E. Nadyozhina (2000). "Numerical Simulation of Wind Farm Influence on Wind Flow". In: *Wind Engineering* 24. DOI: 10.1260/0309524001495620.

Jensen, N. O. (1983). *A note on wind generator interaction*. 2411. Risø National Laboratory.

Keith, D. W., J.F . Decarolis, D. C. Denkenberger, D. H. Lenschow, S. L. Malyshev, S. Pacala, and P. J. Rasch (2004). "The influence of large-scale wind power on global climate". In: *Proceedings of the National Academy of Sciences of the United States of America* 101.46, pp. 16115–16120. ISSN: 0027-8424. DOI: 10.1073/pnas.0406930101.

Kirk-Davidoff, D. and D. W. Keith (2008). "On the Climate Impact of Surface Roughness Anomalies". In: *Journal of the Atmospheric Sciences* 65. DOI: 10.1175/2007JAS2509.1.

Landberg, L. (2016). *Meteorology for Wind Energy: An Introduction*. Wiley.

Langor, E. N. (2019). "Characteristics of offshore wind farm wakes and their impact on wind power production from long-term modelling and measurements". MA thesis. Technical University of Denmark - DTU.

Larsén, X. G., S. Larsen, and M. Badger (2011). "A case-study of mesoscale spectra of wind and temperature, observed and simulated". In: *Quarterly Journal of the Royal Meteorological Society* 137. DOI: 10.1002/qj.739.

Lee, J. C. Y. and J. K. Lundquist (2017). "Evaluation of the wind farm parameterization in the Weather Research and Forecasting model (version 3.8.1) with meteorological and turbine power data". In: *Geoscientific Model Development Discussions*. DOI: 10.5194/gmd-2017-128.

Lu, H. and F. Porté-Agel (2010). "Large-eddy simulation of a very large wind farm in a stable atmospheric boundary layer". In: *Physics of Fluids - PHYS FLUIDS* 23. DOI: 10.1063/1.3589857.

Malyshev, S., S. Pacala, D. Keith, D. Denkenberger, S. Baidya Roy, and E. Shevliakova (2003). "Climate Response to Large-Scale Wind Farms". In: *AGU Fall Meeting Abstracts*.

OffshoreWake (2017). *OffshoreWake: Large Scale Offshore Wake Impact on Danish Power System*. URL: https://www.offshorewake.dk/about-the-project/overview#purpose.html.

Okulov, V., I. Naumov, R. Mikkelsen, I. Kabardin, and J. Sørensen (2014). "A regular Strouhal number for large-scale instability in the far wake of a rotor". In: *Journal of Fluid Mechanics* 747. DOI: 10.1017/jfm.2014.174.

Peña, A., S. Gryning, and C. B. Hasager (2008). "Measurements and Modelling of the Wind Speed Profile in the Marine Atmospheric Boundary Layer". In: *Boundary-Layer Meteorology* 129. DOI: 10.1007/s10546-008-9323-9.

Platis, A. et al. (2018). "First in situ evidence of wakes in the far field behind offshore wind farms". In: *Scientific Reports* 8. DOI: 10.1038/s41598-018-20389-y.

Pryor, S. C., T. J. Shepherd, P. J. H. Volker, A. N. Hahmann, and R. J. Barthelmie (2020). "'Wind theft' from onshore wind turbine arrays: Sensitivity to wind farm parameterization and resolution". In: *Journal of Applied Meteorology and Climatology* 59.1, pp. 153–174. ISSN: 1558-8424. DOI: 10.1175/jamc-d-19-0235.1.

Sawyer, S. and Q Liming (2017). *Global Wind Report - Annual Market Update 2017*. Global Wind Energy Council (GWEC).

Shepherd, T.J., R.J. Barthelmie, and S.C. Pryor (2020). "Sensitivity of wind turbine array downstream effects to the parameterization used in WRF". In: *Journal of Applied Meteorology and Climatology* 59.3, pp. 333–361. DOI: 10.1175/JAMC-D-19-0135.1.

Siedersleben, S. et al. (2018). "Evaluation of a Wind Farm Parametrization for Mesoscale Atmospheric Flow Models with Aircraft Measurements". In: *Meteorologische Zeitschrift*. DOI: 10.1127/metz/2018/0900.

Skamarock, W. C., J. Klemp, J. Dudhia, D.O. Gill, D. Barker, W. Wang, and J. G. Powers (2008). "A description of the advanced research WRF version 3". In: 27.

Tennekes, H. and J. Lumley (1972). "A First Course in Turbulence". In:

Vanderwende, B., B. Kosovic, J. K. Lundquist, and J. Mirocha (2016). "Simulating effects of a wind turbine array using LES and RANS". In: *Journal of Advances in Modeling Earth Systems*. DOI: 10.1002/2016MS000652.

Vermeer, L. J., J. N. Sørensen, and A. Crespo (2003). "Wind turbine wake aerodynamics". In: *Progress in Aerospace Sciences* 39. DOI: 10.1016/S0376-0421(03)00078-2.

Volker, P. J. H. (2014). "Wake Effects of Large Offshore Wind Farms - a study of the Mesoscale Atmosphere". PhD thesis. Technical University of Denmark - DTU.

Volker, P. J. H., J. Badger, A. N. Hahmann, and S. Ott (2015). "The Explicit Wake Parametrisation V1.0: a wind farm parametrisation in the mesoscale model WRF". In: *Geoscientific Model Development Discussions* 8. DOI: 10.5194/gmdd-8-3481-2015.

Wallace, J. M. and P. V. Hobbs (2006). *Atmospheric Science*. 2nd ed. Elsevier.

Wang, C. and R. G. Prinn (2010). "Potential climatic impacts and reliability of very large-scale offshore wind farms". In: *Atmos. Chem. Phys.* 10, pp. 2053–2061. DOI: 10.5194/acp-10-2053-2010.

– (2011). "Potential climatic impacts and reliability of large-scale offshore wind farm". In: *Environmental Research Letters - ENVIRON RES LETT* 6. DOI: 10.1088/1748-9326/6/2/025101.

WindEurope Business Intelligence (2020). *Wind Energy in Europe in 2019: Trends and statistics*. WindEurope.

Wu, Y.-T. and F. Porté-Agel (2012). "Simulation of Turbulent Flow Inside and Above Wind Farms: Model Validation and Layout Effects". In: *Boundary-Layer Meteorology* 146. DOI: 10.1007/s10546-012-9757-y.

Zhang, M. H. (2015). *Wind Resource Assessment and Micro-siting: Science and Engineering*. Wiley. DOI: 10.1002/9781118900116.